DOCTORAL DISSERTATION

Paleoceanographic reconstruction and Cordilleran Ice Sheet dynamics during the last deglaciation inferred from multiproxy geochemical records of the Gulf of Alaska sediment core

アラスカ湾堆積物コアの地球化学データによる融氷期の古海洋復元と
コルディエラ氷床の動態

By
Md. Nurunnabi Mondal

Graduate School of Science and Engineering
University of Toyama
Japan

September 2021

Paleoceanographic reconstruction and Cordilleran Ice Sheet dynamics during the last deglaciation inferred from multiproxy geochemical records of the Gulf of Alaska sediment core

by

Md. Nurunnabi Mondal

ID number: 31878301

a dissertation submitted to the Graduate School of Science and Engineering,
University of Toyama, Japan
in partial fulfillment of the requirements for the degree of

Doctor of Philosophy

Supervisor
Dr. Keiji Horikawa, Associate Professor

Graduate School of Science and Engineering
University of Toyama
Japan

September 2021

Thesis Approval Committee

This thesis entitled,

“Paleoceanographic reconstruction and Cordilleran Ice Sheet dynamics during the last deglaciation inferred from multiproxy geochemical records of the Gulf of Alaska sediment core” submitted by **Md. Nurunnabi Mondal,** is approved for the degree of the Doctor of Philosophy.

This research was conducted at the Graduate School of Science and Engineering, University of Toyama, Japan.

Thesis approval committee

1.	**Dr. Keiji Horikawa, Associate Professor**	**Supervisor**
2.	**Professor Dr. Jing Zhang**	**Chairman**
3.	**Professor Dr. Naoto Ishikawa**	**Examiner**
4.	**Dr. Yusuke Okazaki, Associate Professor**	**Examiner**

ABSTRACT

During the last glacial maximum (26–19 ka, ka = kilo annum = 1000 years before present), the Cordilleran Ice Sheet (CIS) expanded in the northwest part of North America, and the western margin of the CIS was a marine-based ice sheet, like the present-day Greenland Ice Sheet. The CIS was rapidly decayed during the last deglacial period from Heinrich Stadial 1 (HS1, ~17.5–14.8 ka) to Preboreal (~11.7–10.8 ka) due to sea-level rise and oceanic and atmospheric warming. However, the exact timing of glacial meltwater injection and its source from the CIS into the northeastern Pacific has been debated, even though a large amount of glacial meltwater might have potential perturbating effects on the global thermohaline circulation and climate. In addition, the impact of meltwater injection on marine productivity has also been debated since Alaskan glacial meltwater provides large amounts of bioavailable iron (Fe) to coastal areas. These issues address in this thesis by reconstructing the paleoceanographic conditions and dynamics of the CIS in detail using marine sediment cores collected near the former CIS, where high-resolution geochemical analyses are available. This study analyzed a sediment core (KH17-3 CL14PC/MC, 59°33.35' N, 144°09.35' W, water depth 690 m), which covers sediment records for the Holocene to the last deglaciation from HS1 (~17 kyr ago), collected at the coastal area in the Gulf of Alaska (GOA), and generated high-resolution geochemical records.

First, this thesis assessed XRF core scanner multi-element count data of Core CL14PC (Chapter 2). Typically, the downcore variations in element counts measured by an XRF core scanner cannot be regarded as variations in element concentration because such element counts are decreased by higher water and organic matter contents. Downcore changes in elemental concentrations are important for inferring paleoceanographic and sedimentological conditions with time. Thus, these count data must be evaluated against concentration data or converted to concentration-equivalent elemental count data. This study measured element concentrations (Sr, Fe, Mn, Ti, Ca, and K) of selected 33 discrete sediment samples from Core CL14PC to evaluate the XRF core scanner elemental counts and found that high water contents largely decreased some elemental count. The effect of water contents on elemental counts could be successfully corrected by normalization by coherent/incoherent X-ray scatter ratio (CIR). Consequently, the CIR-normalized element counts are highly correlated with element concentrations ($0.56 < R^2 < 0.91$). The high-water contents in the sediments increase X-ray

scatter and reduce element-specific X-ray fluorescence; CIR-corrected element count data can correct water content variability and retrieve the original intensity.

Secondly, %$C_{37:4}$ alkenones, foraminifer $\delta^{18}O$, ice-rafted debris (IRD), and Sr-Nd isotopes records were used to determine detailed timing and sources of glacial meltwater injection from CIS into the GOA. This study found higher IRD deposition and higher %$C_{37:4}$ alkenones (indicating low salinity or colder water masses) occurred at ~16.4, ~16.2, and ~15.6 ka during HS1. These data provide robust evidence for collapsing of CIS multiple times during the cold HS1, probably owing to subsurface warming in response to intensified Aleutian Low. In addition, higher %$C_{37:4}$ alkenones (24% and 28%) were also found at ~14.1 and ~13.9 ka during early Bølling-Allerød (B-A) accompanied by depleted planktonic foraminifer $\delta^{18}O$ values. It is interpreted to reflect low salinity surface conditions due to meltwater. A prominent high peak of %$C_{37:4}$ alkenone occurred again in the middle Younger Dryas (~12.2 ka, YD) and then decreased (<5%). These data suggest that most of the CIS stopped melting after the end of YD. The detrital Sr-Nd isotopic compositions demonstrate that the sources of detrital sediments are proximal areas to the core site and did not change throughout the last deglaciation (HS1–YD). This evidence indicates that the core site had been influenced by the melting of the northern part of the marine and land-based CIS. From these salinity and sediment provenance data, this thesis describes the meltwater events in the northern GOA, showing the northern CIS's melting history at least four times from ~16.4–15.2 ka during HS1 and at least three times from ~14.6–12.2 ka during B-A to YD. However, the CIS melted intermittently but gradually over a long period throughout the last deglaciation and minorly contributed to the abrupt global sea-level rise (14.6–14.3 ka).

Furthermore, this study assessed the decadal- to centennial-scale paleoproductivity changes and their relation to CIS dynamics from XRF Bromine (Br), TOC, density, C-N ratio, and foraminifer $\delta^{18}O$ records. High peaks of Br and TOC, low C-N ratio, and low-density laminated sediments during B-A (~14.8–13.0 ka) and Preboreal (~11.6–11.1 ka) intervals indicate that B-A and Preboreal were higher productivity periods. However, timings of the higher productivity were not tightly matched to the inferred meltwater periods during the B-A. Instead, a minor offset between surface-and sub-surface-dwelling foraminifer $\delta^{18}O$ records suggests that high vertical mixing might have induced higher productivity. High XRF Fe data suggest that glacier Fe fertilization and/or remobilization of bioavailable Fe due to sea-level rising inundated coastal depocenter might have also been enhanced the productivity.

ACKNOWLEDGMENTS

All praises are for Almighty Allah, who enables me to present this dissertation for the degree of Doctor of Philosophy (Ph.D.).

I would like to express my deepest gratitude and sincere appreciation to my supervisor Dr. Keiji Horikawa, Associate Professor, Graduate School of Science and Engineering, University of Toyama, Japan, for providing me the opportunity to conduct my research, teaching, guidance during research activities and preparation of this dissertation, and for his recommendation to get the MEXT scholarship.

I also want to express my sincere appreciation to Prof. Dr. Jing Zhang, Prof. Katsumi Marumo, Dr. Tamihisa Ohta, Dr. Takanori Kagoshima, and all my course instructors for their support and teaching and guidance.

I express my sincere thanks to Dr. Yusuke Okazaki, Associate Professor, Kyushu University, for his cooperation, suggestion, and necessary correction while preparing the thesis and manuscript for publication.

I also express my sincere thanks to Prof. Dr. Masafumi Murayama, Kochi University, and Prof. Dr. Hideki Minami, Tokai University, for their guidance and support while conducting the research and measurement of the sample.

I sincerely acknowledge Professor Dr. Osamu Seki and Mr. Arifur Rahman, Hokkaido University, Japan, for measuring alkenones' biomarkers.

I also thank Mr. Katsuya Nejigaki for his contribution during the instrumental measurement part of planktonic foraminifer $\delta^{18}O$, $\delta^{13}C$, and bulk sediment Nd isotope. In addition, I also thank Mr. Masahiro Noda for his cooperation during the instrumental measurement part of bulk sediment Sr isotopes.

I am grateful to Kochi University technical staff Mr. Shizu Yanagimoto (density measurement), Mr. Takuya Matsuzaki, Mr. Kazuno Arai, and Mr. Shinsuke Yagyu (ITRAX XRF multi-element measurement) for their cooperation.

I thankfully acknowledge the funding support of this work by the Japan Society for the Promotion of Science under the program grants-in-aid for scientific research (KAKENHI, #JP17H01853), and the Dr. Hajime Obata, Dr. Koji Seike, onboard scientist, captain, and crew of the R/V Hakuho-Maru KH17-3 cruise.

I also like to thank my examination committee members.

I am grateful to all my former and present lab members, especially Yuki Tezuka, Hinako Nishimura, Yukiko Kozaka, Kikuchi, and Dr. Mst. Shamsun Nahar for their suggestions during research work and during the operating of the instrument.

I wish to thank MEXT (Ministry of Education, Culture, Sports, Science, and Technology) for their support during my Ph.D. life by providing the scholarship.

I am sincerely express my thanks to my university, Bangabandhu Sheikh Mujibur Rahman Agricultural University, Gazipur-1706, Bangladesh, for allowing me to pursue higher studies in Japan.

I express my boundless gratitude and endless thanks to my parents (I lost them during this study period). I also thank my family members, relatives, and friends who inspired me during my study period in Japan. Finally, I am very grateful to Jannatun Shahin, my wife, for her continuous overall support in my life and my daughters Fabiha Anbar Aurin and Fatiha Anhar Audrin.

TABLE OF CONTENTS

LIST OF TABLES

LIST OF FIGURES

Chapter 1. General Introduction

1.1. Background

During the Late Wisconsinan, the vast mountainous terrain in Alaska generated a mass of glacier ice comparable to that of all the Western United States combined. All glaciers once covered Alaska and its adjacent continental shelf during the global Last Glacial Maximum (LGM) of about 727,800 km^2 (Kaufman & Manley, 2004), and the amalgamation of coalescent ice caps and piedmont lobes formed the north-western extension of the Cordilleran Ice Sheet (CIS) (Hamilton and Thorson, 1983). During LGM, the CIS stretched from the Alaska Range in the north to the North Cascades in the south, calved into the Pacific Ocean, and merged with the Laurentide ice sheet (LIS) in the western margin (Dawson, 1888; Taylor et al., 2014; Seguinot et al., 2016). In Alaska, the CIS was unique not only for the vastness of the glaciated terrain but also for the relative extent of the glaciers during the Late Wisconsinan (Kaufman & Manley, 2004). However, the growth of the CIS was complex. In many cases, the history is unknown, especially the history of glacial advances in most parts of southeast Alaska (Hamilton, 1994) and along the continental shelf of the Gulf of Alaska (GOA) (Kaufman & Manley, 2004).

At the end of its maximum extent, the western margin became unstable (Clague & James, 2002), the period known as the last deglaciation. The last deglaciation refers to the transitional period after the end of the last glacial maximum to the Holocene interglacial period. It encompasses the glacial to interglacial state with abrupt warming and cooling events (Clark et al., 2012). Change in insolation triggered the global change during the period, also associated with changes in ice sheets, the concentration of greenhouse gas, and other amplifying feedbacks that produced remarkable global and regional responses (Clark et al., 2012). During the early deglaciation (Heinrich Stadial 1) between ~17.5 to ~15.0 ka (kilo annum = 1000 years before present), substantial meltwater discharges from the glacial ice sheet of the Northern Hemisphere substantially weakened or eliminated the meridional overturning (Atlantic meridional overturning circulation, AMOC) circulation in the North Atlantic region (Clark et al., 2001; McManus et al., 2004). The circulation also influenced the circulation and climate change in the North Pacific Ocean (Broecker, 1994; Clark et al., 2002; Chikamoto et al., 2012). During that time, the δ^{18}O records of the North Greenland Ice Core Project (NGRIP) show the cooling period (Rasmussen et al., 2006). During the period (17–16 ka), the short-lived cooling of ocean surface temperature in the eastern Pacific and Gulf of Alaska (GOA) may have slow down the retreat of the western margin of ice (Darvill et al., 2018). Subsequently, the most abrupt climate changes were observed in the Bølling-Allerød (B-A) transition during the last deglaciation, followed by a sharp sea-surface temperature (SST) warming of 4–5°C compared to Heinrich Stadial 1 (HS1) (Praetorius et al., 2015). The climate forcing and the ice sheet response, and the synchroneity and asynchroneity between the North Atlantic and the North Pacific climate coupling during the B-A, have a debate (Praetorius and Mix, 2014). Praetorius and Mix (2014) interpreting that synchronous (between the North Atlantic and the North Pacific) climate coupling dynamics occurred in these regions between ~15.5 to 11.0 ka ago. During the early B-A transition (14.6–14.3 ka), the Tahiti record indicated 12–22 m of sea-level rise (Deschamps et al., 2012). Besides, Weaver et al. (2003) indicating that during B-A, the Antarctic Ice Sheet contributes ~20 m of sea-level rise, and the onset was concurrent with the Tahiti record. During this period, the AMOC accelerated (McManus et al., 2004), thus subsequently increase the temperature in the North Atlantic region. However, this evidence suggesting that the synchronous climate forcing between the North Atlantic and the North Pacific may lead the Northeast Pacific B-A critical transition during the last deglacial period in the region. Ice sheet response with this climate forcing and subsequent meltwater inject into the ocean (Menounos et al. 2017). Melting of ice separate two ice sheets (LIS and CIS). The result of two model studies indicated that the separation of LIS and CIS was completed by 14.5 ka (Peltier et al. 2015) or the end of 13.5 ka (Lambeck et al., 2017). Subsequently, in the Younger Dryas (YD), an abrupt 3–4°C cooling of sea-surface temperature (SST) was found in the paleotemperatures records in the northern GOA by Praetorius et al. (2015). The synchronous Northern Hemisphere abrupt cooling event during the YD in the Northeast Pacific, the increased freshwater flow briefly declined AMOC in the North Atlantic region (Clark et al., 2001; McManus et al., 2004). After YD, the temperature increases up to 5°C (Praetorius et al., 2015) during the early Holocene in the northern GOA. During this period, the abrupt sea-level rise (11.45–11.1 ka) was recorded in Barbados coral record by Abdul et al. (2016).

However, for the study of ice sheet (CIS) dynamics during the major climate transition (last deglaciation), previous studies used ^{14}C (Dalton et al., 2020) and ^{10}Be dating (Menounos et al. 2017) from land-based sources from former CIS covering regions. For the North American Ice Sheet Complex study, Dalton et al. (2020) integrated the information from regional experts. They maintained consistency with Dyke et al. (2003) and Dyke (2004) listed radiocarbon (^{14}C) data and original positions of the ice margin. For radiocarbon (^{14}C) dating, the Alaska regional experts used different materials from land-based sources. They used wood, wood fragments, roots, seeds, plant debris, Salix roots, plants in dune, plant detritus, chitin, pollen in lake sediment, organics in dune, peat, basal peat, macrofossils, shells, charcoal, Mammuthus, soil over till, etc. However, variations of materials, radiocarbon, laboratory techniques, standards reference materials, and correction of radiocarbon dates (Terasmae, 1984) make a considerable variation of ^{14}C dating. Furthermore, in the case of ^{10}Be dating (Menounos et al. 2017) from erratic boulders and bedrock, the production of ^{10}Be varies with latitude, elevation, and topographic shielding (Rinterknecht et al., 2012; Li et al., 2014; Stroeven et al., 2014), thus make exposure age calculation complex. In addition, several post-depositional difficulties like rolling, exhumation, burial, or boulder cover with vegetation interrupt the cosmogenic nuclides accumulation in the boulder. That makes exposure age younger than the actual age (Stroeven et al., 2010; Heyman et al., 2011; Li et al., 2014). Furthermore, inheritance ^{10}Be contamination makes exposure age older than the actual age (Young et al., 2009; Stroeven et al., 2014; Matthews et al., 2017; Margold et al., 2019). Although this method is used widely in the study of glacier history, it makes a considerable age uncertainty; instead, the record from marine sediment provides a detailed archive of glacier dynamics (Penkrot et al., 2018). Therefore, well constraining the timing of CIS loss inferred from meltwater injection into the ocean and their impact on the ocean required comprehending study.

1.2. Objectives of the study

This study investigates the CIS dynamics through reconstruction of meltwater injection into the ocean, and their relation to paleoproductivity through high-resolution productivity tracer and relevant proxy from the GOA sediment, focusing on the last deglaciation. During this climate transition period, the marine-based CIS margins were retreated and strongly affected due to calving and subsequently accelerated ice-mass loss due to warming and rising sea level (Praetorius et al., 2015; Lesnek et al., 2020). The resulting meltwater injected into the GOA thus makes surface water freshened. In the GOA, Praetorius et al. (2020) observed surface freshening during the early deglaciation (19–16.5 ka) and YD (12.9–11.7 ka). Their (Praetorius et al., 2020) observation based on sea-surface temperature (SST) calculated from haptophyte alkenone index using Prahl et al. (1988) equation and $\delta^{18}O$ records from planktonic foraminifer. The haptophyte and planktonic foraminifera are two different biotas, and both are not dominated at the same time and in the same season. In addition, for calculating seawater $\delta^{18}O_{sw}$ they used Bemis et al. (1998) 12-chambered shell (*Globigerina bulloides*) equation. However, Bemis et al. (1998) restricted the use of their equation only for *Globigerina bulloides*. Besides, the planktonic foraminifer $\delta^{18}O$ records sometimes fail to characterize freshwater signals by producing anomalously lighter values, especially during Heinrich Stadial (Maier et al., 2018). Because in cold water conditions, the planktonic foraminifer usually makes the heaviest $\delta^{18}O$ value. Therefore, the surface freshening or the sea-surface salinity (SSS) should be required re-evaluation using an independent proxy or independent proxies. Knowledge on the relative abundance of tetra-unsaturated C_{37} alkenone as a percentage (%$C_{37:4}$) to the total abundance of di-, tri-, and tetra-unsaturated C_{37} alkenone, sediment provenance, planktonic foraminifer isotopes, and ice-rafted debris provides a robust framework for an accurate reconstruction of meltwater injection period and should help for study of ice sheet dynamics. Furthermore, for paleoproductivity, the previous research used low-resolution biogenic silica (opal) from diatom (Addison et al., 2012). Diatom frustule also contains Bromine (Br) (Leri et al., 2010). Therefore, X-ray fluorescence (XRF) core scanning high-resolution Br can reconstruct paleoproductivity. But, XRF core scanning of multi-elements counts influence by other factors during measurement (Tjallingii et al., 2007; Boyle et al., 2015; Woodward & Gadd, 2019). Unverified use of these multi-elements count data deviates the paleoceanographic interpretation (Hennekam & de Lange, 2012). So, the initial XRF multi-element data needed proper calibration. With these in mind, in this study, the paleoceanographic reconstruction and Cordilleran Ice Sheet dynamics studying through:

- determine a definite calibration method for correction of the multi-elemental high-resolution initial count data for further application in paleoceanographic studies
- reconstruction of the glacial meltwater injection into the northeastern Gulf of Alaska coastal margin during the last deglacial period
- assessment of the paleoproductivity based on high-resolution new productivity tracer during the last deglaciation in the northeastern Gulf of Alaska

1.3. Study area

The sediment sample used in this study was collected from the coastal margin of the Gulf of Alaska (59° 33.35´N and 144° 09.35´W) in the northeast Pacific Ocean (**Figure 1**). The area locates in the vicinity of the former CIS. Thus, the strategic position of the study site is ideal for received meltwater signals from the CIS. In addition, it is well-suited to obtain a comprehensive paleoproductivity overview of the investigated area. The Gulf of Alaska's coast stretches in the Kodiak Island and the Alaska Peninsula in the west to the Alexander Archipelago in the east. The coastline is a rugged combination of mountains, forests, and several glaciers. Its surface and subsurface water hydrology are predominantly influenced by the North Pacific Gyre (Tomczak & Godfrey, 1994) and two currents (subarctic Gyre and Alaska Coastal Current). The coastal oceanography in the Gulf of Alaska describes in chapter 3 (subsection 3.2.).

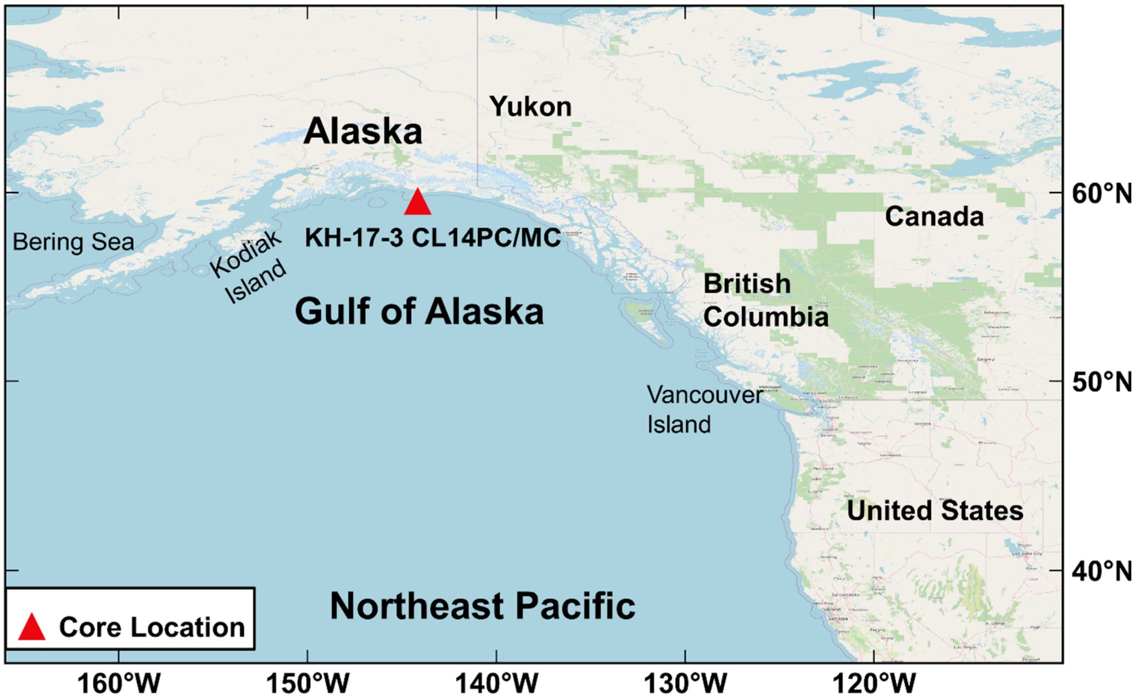

Figure 1. Map showing core location of the studied Core KH-17-3 CL14PC and CL14MC (red triangle) on the Northern Gulf of Alaska continental margin in the Northeast Pacific Ocean.

1.4. Outline of the thesis

This thesis was carried out at the Graduate School of Science and Engineering, University of Toyama, Japan. The thesis consists of five chapters (chapters 1, 2, 3, 4, and 5), with an appendix (appendix A, B, and C) and a references section. The central theme of this study deals with the investigation of a sediment core from the northeastern Gulf of Alaska for paleoceanographic reconstruction and CIS dynamics study by using the high-resolution proxy, reconstruction of deglacial meltwater injection period, and assessment of deglacial paleoproductivity. The results of this study are presented in the succeeding three chapters (Chapters 2, 3, and 4), which correspond to manuscripts published in or manuscript under preparation for submission to the international academic peer-reviewed journals. In this dissertation, references are listed in a single section to minimize duplication. Below are the three main chapters of this dissertation.

Chapter 2. Investigation of adequate calibration methods for X-ray fluorescence core scanning element count data

This chapter focused on the detailed calibration methods for the normalization of the ITRAX X-ray fluorescence core scanner-generated high-resolution multi-elemental count data used for paleoceanographic interpretation. The ITRAX XRF core scanner (CS) is a non-destructive, rapid, automated multi-function core scanner that provides high-resolution geochemical records from sediment cores (Rothwell & Croudace, 2015). The core scanner also provided total count data, incoherent and coherent X-ray scatter data, together with multi-elements intensity data. However, applying the X-ray fluorescence core scanner multi-elemental proxies to the paleoceanographic research required appropriate calibration because several factors especially core physical properties affect the elemental counts during measurement (Tjallingii et al., 2007; Boyle et al., 2015; Gregory et al., 2019; Lee et al., 2019; Woodward & Gadd, 2019; Babin et al., 2020). But, any of the existing approaches for calibration are not widely employed and require rigorous further testing based on sediment variety to find out the best method. Therefore, this study corrected the initial raw data through different approaches to determine the best calibration method. After correction of initial intensity data, a linear formula was used to correlate the calibrated intensity data with concentration measured by wavelength-dispersive XRF and elemental analyzer and compared the result. The study showed that the coherent/incoherent X-ray scatter ratio (CIR) calibration approach was better among the tested methods. And, the correlation values improved significantly from the initial values for all the tested elements. Furthermore, the study used this calibration approach (i.e., element count/CIR) to calibrate the high-resolution multi-element count data. The study also explains the cause of deviation of intensity and the way to retrieve it.

Chapter 3. Glacial meltwater injection into the northern Gulf of Alaska from Cordilleran Ice Sheet during the last deglaciation

Here, the author describes the reconstruction of the timing and sources of glacial meltwater injection into the northern Gulf of Alaska during the last deglacial climate events. For reconstructing meltwater events and their potential sources, the study used alkenone salinity proxy (%$C_{37:4}$) and sediment provenance proxies that have not been previously reported. Besides, the study also used foraminifer stable isotope records ($\delta^{18}O$, $\delta^{13}C$) and ice-rafted debris data to reconstruct environmental conditions associated with the deglacial retreat history of the CIS. This study constructed the age-depth model using radiocarbon (^{14}C) dating from *Globigerina bulloides* and *Neogloboquadrina pachyderma* (sinistral). The result showed that the Gulf of Alaska would have received meltwater multiple times during Heinrich Stadial 1 and from Bølling-Allerød to Younger Dryas during the last deglaciation. Furthermore, the Sr-Nd isotope signature constrains that the meltwater sources were proximal to the core-site. In early Bølling-Allerød from 14.6–13.8 ka (~800 years), substantial mass loss of CIS occurred. The study also interpreted that the CIS dynamics cease after the end of the Younger Dryas.

Chapter 4. Multiproxy analysis of high-resolution records revealing paleoproductivity change in the northern Gulf of Alaska

This chapter used previously calibrated (chapter 2) high-resolution XRF-element data and the inferred meltwater information (chapter 3) to evaluate the productivity during the last deglaciation in the northern Gulf of Alaska continental margin. Here, high-resolution XRF Br has been used as the marine paleoproductivity proxy. The XRF Br are highly correlated with TOC contents. The finding indicated peak productive periods at ~14.8–13 ka and ~11.6–11.1 ka, corresponding to the Bølling-Allerød and Preboreal, found during the low-density laminated sedimentation period. However, the productivity proxies were consistently lower during the Heinrich Stadial 1 and Younger Dryas meltwater period. In addition, the productivity proxies did not tightly coincide with the multiple peak meltwater period in the Bølling-Allerød.

Besides these three main chapters (chapters 2, 3, and 4), this thesis summarizes and concludes information in chapter 5. This thesis also described some chemicals and reagents used in this study, described some methodology, and input some data and a figure in the appendix (appendix A, B, and C) section.

Chapter 2. Investigation of Adequate Calibration Methods for X-ray Fluorescence Core Scanning Element Count Data

Abstract

X-ray fluorescence (XRF) core scanner elemental count data are useful for high-resolution paleoceanographic studies. However, because several factors, such as changes in physical core properties, significantly affect element count intensities, the appropriate calibration of the count data is required. Besides, the existing approaches for calibration were not widely employed and required rigorous testing based on sediment variety. In this study, the high-resolution element intensity (cps) from a wet, muddy marine sediment piston core was analyzed that was collected from the northeast Gulf of Alaska and tested several approaches with ratio and log-ratio methods. The reliability was evaluated by comparison with the concentrations that WD-XRF and an elemental analyzer measured. The results showed that the lighter elements (Ti and K) exhibited a significantly weak relationship between raw counts measured by ITRAX and concentrations measured by the WD-XRF, indicating that some factors artificially influence ITRAX intensity data. The Chlorine (Cl) intensity expressed as the water content in marine sediment increased significantly in the upper 202 cm by 42% and the top 25 cm by 73% compared to the down-core (below 202 cm), which deviates the X-ray scattering and element-counts. The calibration of initial raw data through coherent/incoherent X-ray scatter ratio (CIR) and additive- and centered-log ratio reduces the offsets. The calibration by CIR performed best for the elements Sr, Fe, Mn, Ti, Ca, K, and Br (correlation with concentration $0.56 < R^2 < 0.91$), and the correlation with concentration significantly increased for Ti and K of 100% and 56%, respectively. Therefore, the study suggests that correcting raw counts through the CIR approach is effective for wet marine sediment when core physical properties have greater variability.

2.1. Introduction

X-ray fluorescence (XRF) core scanner's non-destructive, rapid, and automated multi-function technique provides useful, high-resolution (sub-millimeter scale) geochemical records from sediment cores (Croudace et al., 2006; Rothwell & Croudace, 2015). Therefore, in paleoceanographic and paleoclimatological research, the use of the XRF core scanner (CS) has increased rapidly due to its capacity for producing ultra-high-resolution elemental proxy records from the decadal to sub-annual scale. It can also analyze the elemental composition from the unprocessed sediment core, significantly reducing the experimental cost. However, despite its rapid acquisition of high-resolution elemental datasets, it has some limitations and drawbacks. For instance, its measurements are influenced by factors, such as the variability/heterogeneity of the scanning sample, the scattering of the X-ray radiation due to water content, and the porosity of the sediment (Rothwell & Rack, 2006; Tjallingii et al., 2007; Hennekam & de Lange, 2012; Boyle et al., 2015; MacLachlan et al., 2015). Therefore, the paleo-researchers working with sediment cores still have a major debate in using X-ray fluorescence core scanner raw data in the paleoceanographic studies compared to conventional measurement. Thus, to correctly interpret the XRF core scanner data, destructive elemental data measurement by inductively coupled plasma mass spectrometry (ICP-MS), wavelength dispersive-XRF (WD-XRF) spectrometer, or energy dispersive-XRF (ED-XRF) spectrometer is also still needed. Furthermore, these conventional methods require homogenized dry powder samples that eliminate sample physical variations and heterogeneity. Although these conventional (ICP-MS, WD-/ED-XRF) techniques are well established and provide reliable datasets, they are low-resolution and discrete, time-consuming, and not cost-effective (Croudace et al., 2006). In addition, conventional methods require a complex sample preparation technique and a variety of standard and/or standard reference materials for precision and accuracy.

In fluorescence spectrometry, X-ray scattering has great importance because the scattering (coherent, incoherent) or scattering ratios (coherent/incoherent, incoherent/coherent) are used for the normalization of X-ray fluorescence intensities (Gregory et al., 2019; Lee et al., 2019; Woodward & Gadd, 2019). This X-ray scattering occurred in two different ways—coherent (Rayleigh scattering), when the X-ray beam collides with an atom and deviates with no loss of energy, and incoherent (Compton scattering), when the incident X-ray loses a small fraction of its energy for the target atom's loosely bound electron (Agarwal, 1991). Heavier (high atomic number) elements emit high X-ray fluorescence intensities with less scatter, and the lighter (low atomic number) elements emit low X-ray fluorescence intensities with high scatter. Therefore, the amount of scattering (incoherent and coherent) varies with the mean atomic number of the elements (Boyle et al., 2015). The sample's physical properties and heterogeneities affect X-ray scattering. If the sediments contain high water and/or high organic matter, this favors generating high incoherent (Compton) and low coherent (Rayleigh) scattering (Woodward & Gadd, 2019). Because water or organic matter containing low atomic numbers elements (H, O, C, and N). Besides, the high water content in sediment absorbs X-ray radiation, thus making weaker fluorescence energies (Weltje & Tjallingii, 2008; Hennekam & de Lange, 2012). For the normalization of XRF core scanner data, previous studies used coherent (Lee et al., 2019), incoherent (Hunt et al., 2015), and incoherent/coherent (inc/coh) X-ray scatter ratio (Kylander et al., 2011; Chagué-Goff et al., 2016; Oliva et al., 2018). However, very few studies used the coherent/incoherent X-ray scatter ratio (coh/inc) (Gregory et al., 2019). This study used coherent and incoherent X-ray scatter to calibrate raw ITRAX-XRF CS elements intensities, together with other calibration approaches. Although, some calibration methods have been developed to improve the accuracy of XRF CS data (Tjallingii et al., 2007; Weltje & Tjallingii, 2008; Lyle et al., 2012; Penkrot et al., 2017; Lyle et al., 2018; Gregory et al., 2019; Lee et al., 2019; Babin et al., 2020; Dunlea et al., 2020). The accuracy of these methods requires comprehensive evaluation based on sample types and/or sample location or instrument types (Avaatech, ITRAX, Geotek). In addition, the variability of the presented methods makes the proper selection of calibration methods complex and unclear. Therefore, these methods and their wide-ranging adaptations still need to be rigorously tested using various samples.

In this study, to develop the reliability of the ITRAX-XRF core scanning proxy used for regional to global consequences and for substrate-specific purposes, we measured the high-resolution elements' intensities (counts) by utilizing a wet, muddy marine sediment piston core KH17-3 CL14PC. The core containing millimeter-scale lamination and ice-rafted debris was collected from the Northeastern Gulf of Alaska in the northeast Pacific Ocean. The measured scanning raw intensities (count per second) were normalized through ratio and log-ratio calibration methods with several approaches under each group. Furthermore, to test the accuracy of the raw and calibrated data, they were correlated with the destructive and homogenized sediment sample concentration that was measured by conventional WD-XRF and elemental analyzer and then evaluated the methods.

2.2. Materials and Methods

2.2.1. Sample Collection

The sampling area is located at the continental margin of the Gulf of Alaska (**Figure 1**) in the northeast Pacific Ocean. The sediment sample (piston core CL14PC and multiple core CL14MC) was collected from the site at 690 m water depth.

2.2.2. Core Description and Measurement

The interface between the water and sediment (upper 16.5 cm) was recovered by the multicore (CL14MC) sediment due to the lack of seafloor sediments in the piston core (CL14PC). The total length of the core was 869 cm. The whole core (piston) was divided into nine sections (**Figure 2**). The computed tomography scan (CT-scan) (**Figure 3**) and X-ray photography measurements were conducted by an X-ray CT scanner (Aquilion PRIME Focus Edition, Canon Medical System Corporation). The bulk density (gm/cc) of the core CL14PC was measured by using Multi-Sensor Core Logger (MSCL-S, GEOTEK) gamma-ray attenuation technique at the Kochi Core Center (KCC), Nankoku, Kochi, Japan (Boyd et al., 2008; Smith et al., 2020). The MSCL-S is a non-destructive geochemical and petrophysical core logging platform that measures the bulk density, magnetic susceptibility, resistivity, and fractional porosity (Boyd et al., 2008; Smith et al., 2020).

Afterward, the core sections were split into the archive and working halves for laboratory analysis. The archive half was again subdivided at 1 cm consecutive intervals. The working half was subdivided at intervals of 2–2.5 cm and then preserved at 4 °C in a refrigerator in the laboratory of the University of Toyama, Gofuku, Toyama, Japan, for further study. Here the core depth defines by the centimeters below the seafloor scale (hereafter cmbsf).

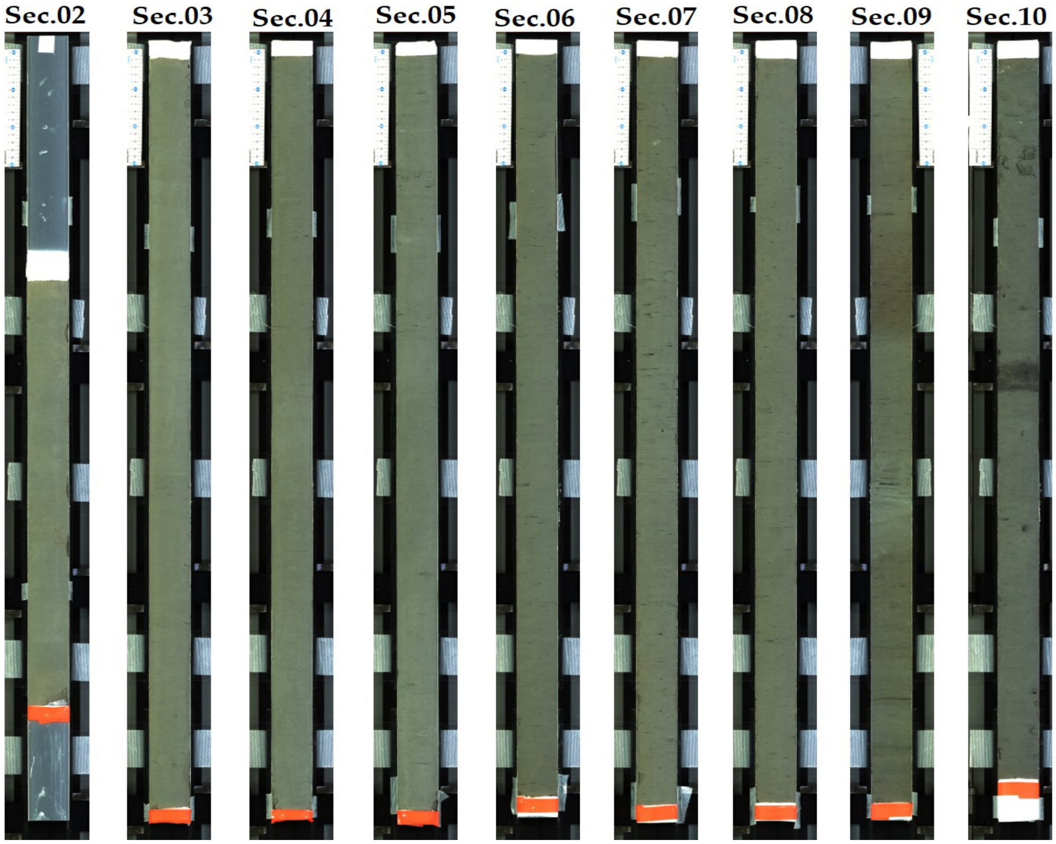

Figure 2. Section (Section 02 (Sec.02)–Section 10 (Sec.10)) pictures of the whole piston core (KH17-3 CL14PC). The number above is the section number of each section.

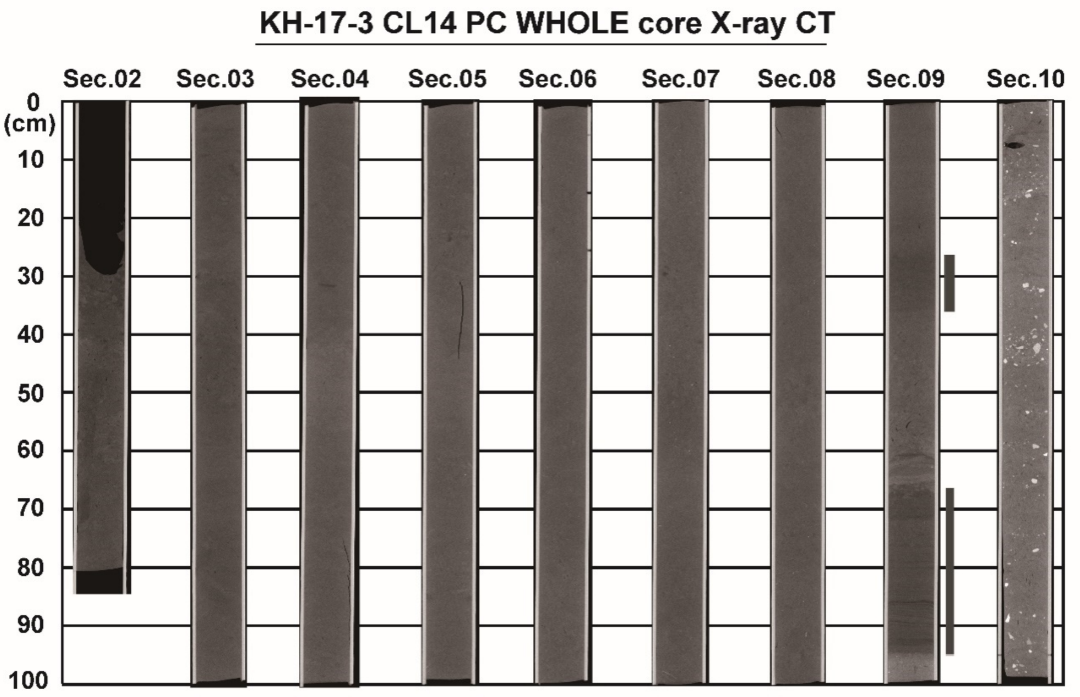

Figure 3. The computed tomographic (CT) scan photography of a total of nine sections (Sec.02–10) of the whole core KH-17-3 CL14PC. The densely (CT-dark) area in Sec.09 represents the lamina and sub-lamina intervals (right side lighter black vertical line indicating the upper and lower limit of the lamina and sub-lamina intervals). Sec.10 is marked by intercalation of ice-rafted debris (white color consists of rocks, foraminifer tests, shells, and fine grain). The black color indicated an empty and disturbed area.

2.2.3. Sediment Analysis

2.2.3.1. Optimization of Scanning Parameters for ITRAX Core Scanner

To obtain the elemental profile, an ITRAX-XRF (COX analytical systems) core scanner was used at the Center for Advanced Marine Core Research (CMCR), Kochi University, Nankoku, Kochi, Japan. A homogenized sediment test pellet ~3 cm wide made from the sediment sample of the core CL14MC at the same site (**Figure 1**) to optimize the exposure time and analytical precision. By using the test sample, triplicate measurement analysis was conducted along one line with an exposure time of 10, 20, 40, and 80 seconds. For scanning, a Molybdenum (Mo) anode X-ray tube was used for X-ray source setting in different voltage and current. We found that increasing the exposure time decreases the relative standard deviation (RSD%). Some elements that are usually used in paleoceanographic studies, such as Fe, Ca, K, Ti, Sr, Mn, and Br, have higher counts (count per second (cps)) (**Figure 4**) setting at 30 kV (kilo Volt) and 55 mA (milli Ampere) of voltage and current, respectively, at 20 s exposure times. The concentration measured through the WD-XRF spectrometer (Subsection 2.2.3.5.) indicates that these elements are marked by the higher concentration of % order in the sample compared to other elements. The RSD% of these elements was <10% (**Figure 4**), specifically 0.52%, 1.57%, 1.24%, 1.76%, 1.97%, 1.82%, and 5.70% for Fe, Ca, K, Ti, Sr, Mn, and Br, respectively. The RSD% was calculated by using the mean value and standard deviation obtained from the test sample reproduced analysis (triplicate measurement) at 20 s exposure time through the following formula (Miller et al., 2018):

$$\mathrm{RSD\%} = ((\sigma/\mu) \times 100) \tag{1}$$

where σ means the standard deviation and μ represents the mean values of the reproduced measurements.

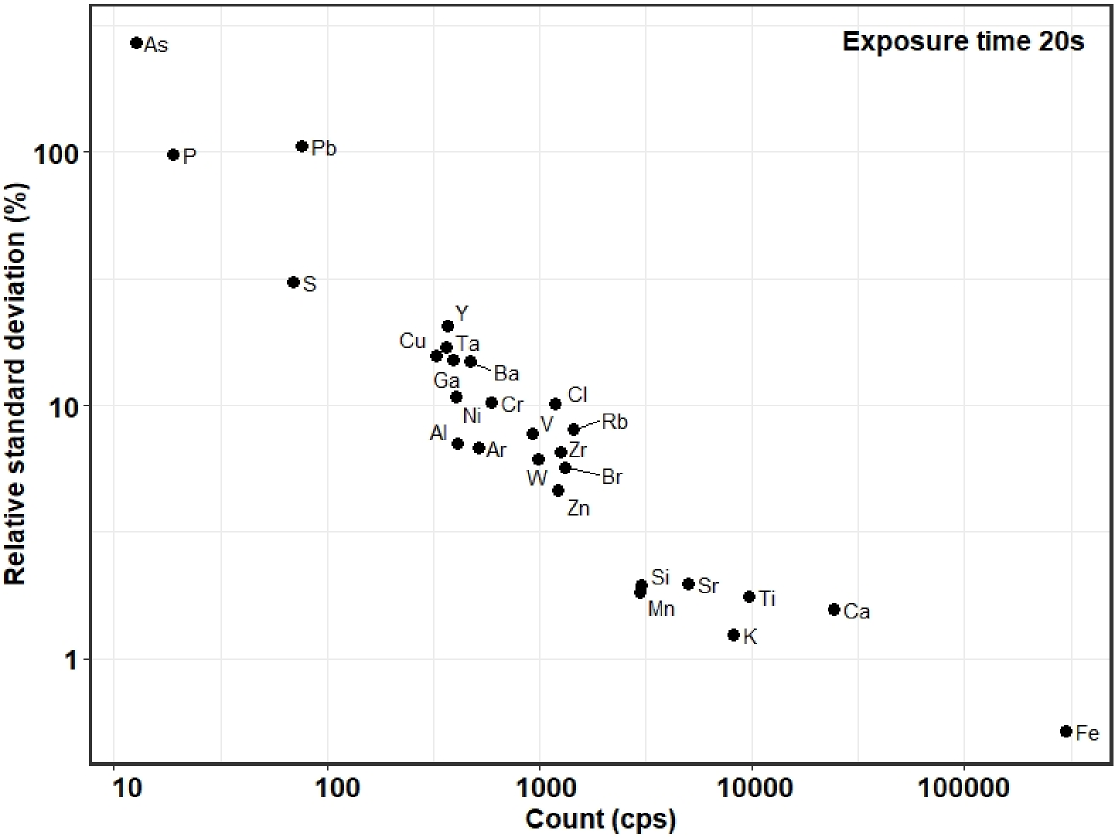

Figure 4. The relationships between count (cps) and the relative standard deviation (RSD%) for all measured elements at 30 kV voltage and 55 mA current of Mo X-ray anode tube. The exposure time (20 seconds) indicating at the top right corner of the plot.

However, given a low enough RSD(%) for the target elements and the required high throughput measurement, the exposure time of 20 s chose for this study, following a previous study (Plaza-Morlote et al., 2017). At this exposure time (20 seconds), with a 30 kV voltage and 55 mA current per 1 cm step, a total of 40–50 minutes is required to measure the 1 m long sediment core. Although with this exposure time (20 seconds), some elements represent lower counts (cps) and higher RSD% (**Figure 4**), such elements require careful attention that is related to instrument settings, including measurement time, applied current and voltage supply, and the type of X-ray source tube used. In particular, the lower- to moderate-atomic number elements Al (Z = 13) and Si (Z = 14) exhibit very low counts, and for Mg (Z = 12), no signal (counts) was found, indicating that the selected scanning parameters and molybdenum X-ray tube cannot perfectly detect these elements. Therefore, enhancement of X-ray excitation is required to detect lower-atomic number elements. However, by changing the X-ray tube (Cr tube) in the second generation ITRAX model, we can obtain good detection (counts) for lower-atomic number elements (Croudace et al., 2006; Rothwell & Croudace, 2015). In **Figure 4**, although Si (Z = 14) shows less RSD% value in the test sample (homogenized pellet) measurement; however, in the case of the measurements of the down-core sediment samples, we found less Si intensity (counts). The detection of lighter elements (like Al or Si) through the Mo-tube is less efficient than using Cr-tube (Rodríguez-Germade et al., 2015). Furthermore, by using a 30 kV voltage and a 55 mA current at a 20 s exposure time, the ITRAX did not provide suitable intensities for the elements Ni, Rb, Y, and Zr (Z = 28, 37, 39, and 40, respectively). Therefore, by increasing the exposure time from 20 to 60 s or by changing the voltage and current to 45 kV and 55 mA, respectively, at 20 s, ITRAX provides higher counts for these high-atomic number elements.

2.2.3.2. Measurement of Multi-Element Count through ITRAX-XRF Core Scanner

For the measurement of the high-resolution non-destructive multi-element count, a sediment sample slab from the working half of the core CL14PC was used. To run the ITRAX core scanner, a sample slab 5 cm wide, 100 cm long, and 1 cm thick was used at 1 cm, 0.4 mm, and 0.2 mm resolution, with a Molybdenum X-ray tube set at 30 kV and 55 mA at 20 s exposure time. By using these scanning parameters, the core scanner detected a total of 27 elements (Al, Si, P, S, Cl, Ar, K, Ca, Ti, V, Cr, Mn, Fe, Ni, Cu, Zn, Ga, As, Br, Rb, Sr, Y, Zr, Ba, Ta, W, and Pb). The coherent and incoherent X-ray scattering of the atoms $13 \leq Z \leq 82$ of the Mo X-ray tube system was used with element intensities. Of the detected elements, eight high-abundance and moderately to highly detectable (higher counts and lower RSD%, **Figure 4**) elements, such as Sr, Br, Fe, Mn, Ti, Ca, K, and Cl, were detected at 1 cm resolution, and the total counts (cps) and coherent (coh) and incoherent (inc) X-ray scatter selected for further data processing and interpretation. The elemental composition of the measured sediment sample was expressed as the intensity count per second (cps).

2.2.3.3. Preparation of Calibration Curve for WD-XRF Concentration Measurement

For the preparation of the calibration curve for WD-XRF concentration measurement, pressed pellet samples from different certified reference materials (CRMs) were used. After being oven-dried (50 °C at 1 h), 4 g of the ground samples were mixed with 0.4 g (10:1) of

Spectro Blend binder. A set of dies was imposed at 120 kN pressure with high-pressure equipment (Riken equipment Co., Ltd., Tokyo, Japan) that was equipped with a pressure gauge on a 40 mm diameter sample cup filled with a powder sample to make the pressed pellet (Takahashi, 2015). In every step of sample preparation, high care was taken to avoid contamination.

Twelve (12) different CRMs (JA-1, JB-1a, JB-2, JB-3, JF-1, JG-3, JGb-1, JP-1, JR-1, JLK-1, and JSd-2 from Geological Survey of Japan (GSJ), Tsukuba, Japan, and MESS-4 from National Research Council Canada (NRCC), Ottawa, ON, Canada) were used to construct a calibration curve. The published certified values of the target elements of these CRMs samples were 0.00033–0.0442, 0.06–10.53, 0.001–0.1817, 0.0021–0.960, 0.39–8.50, and 0.002–8.290 (wt%) for Sr, Fe, Mn, Ti, Ca, and K, respectively. The calibration curve was used for the quantitative analysis of each element prepared through the Empirical Calibration (EC) method. The EC method is the method for calculating the concentration in samples based on the external calibration regression. The external calibration regression can be made by the relationship between the measured intensities of the fluorescence X-ray and the concentration obtained from standard samples similar to the unknown samples and intensities of the fluorescence X-ray of the unknown sample to perform the quantitative measurement. The operational flow (steps) for the quantitative measurement through the EC method are creating application files, setting of application information, standard samples, analysis information and measuring condition, measurement of standard samples, calculation of regression, and setting of the control information.

Through different setup conditions (**Table 1**) and the setting of regression formulae, the background subtraction, drift correction, and matrix/overleap correction methods for smoothing the calibration curve were implemented.

Table 1. Measuring conditions for the selective elements of interest measured by Wavelength-Dispersive X-ray Fluorescence (WD-XRF) Supermini 200 spectrometer.

Element	Analyte line	Peak measurement angle (2θ)	Time (s)	Detector	PHA	Crystal	Voltage (kV)	Current (mA)
Sr	Kα	25.130	20	SC[1]	100–300	LiF (200)	50	4.00
Fe	Kα	57.470	20	SC	100–350	LiF (200)	50	4.00
Mn	Kα	62.952	20	SC	100–350	LiF (200)	50	4.00
Ti	Kα	86.110	20	SC	50–300	LiF (200)	50	4.00
Ca	Kα	45.176	40	PC[2]	100–300	PET	50	4.00
K	Kα	50.150	40	PC	100–300	PET	50	4.00

[1] SC-Scintillation Counter; [2] PC-Proportional Counter.

2.2.3.4. Validation of Calibration Curve

A sample with known concentration was analyzed to check the validation of the calibration curve that was prepared through the Empirical Calibration method. This study used JA-3 certified reference material sample from the geological survey of Japan. For the preparation of the pressed pellet, an oven-dried sample (JA-3) was used. The sample preparation was the same as described in the above section (Subsection 2.2.3.3.). The analytical uncertainty (percent relative standard deviation (RSD%)) of the reproduced ($n = 7$) measurements was less than 1% for all elements (K, Ca, Ti, Mn, Fe, and Sr). The percent relative standard deviation is expressed as RSD% = $((\sigma/\mu) \times 100)$, being the same as Equation (1) (Miller et al., 2018).

According to the guidelines of the international union of pure and applied chemistry (IUPAC), the detection limit (L_D) and the quantification limit (L_Q) were calculated based on the following Equations, respectively (Currie, 1995; Gazulla et al., 2010):

$$L_D = 3.29 * s \qquad (2)$$

$$L_Q = 10 * s \qquad (3)$$

where s is the standard deviation of the reproduced measurements. In the case of quantification, limit the values ten times the standard deviation. **Table 2** presents the calculated values of the L_D and L_Q based on Equations (2) and (3).

Table 2. The detection limit (L_D) and quantification limit (L_Q) of the elements measured by WD-XRF spectrometer from the replicate measurements (*n* = 7) of the sample JA-3 according to Equations (2) and (3).

Element	**L_D (wt%)**	**L_Q (wt%)**
K	0.01	0.02
Ca	0.03	0.10
Ti	0.01	0.02
Mn	0.003	0.01
Fe	0.03	0.10
Sr	0.0	0.0

Replicate measurements (*n* = 7) of the standard sample (JA-3) confirmed that there was no significant difference ($\Delta_m \leq U_\Delta$) between the measured and reference value of the target elements (**Table 3**). The values of Δ_m and U_Δ are obtained from the following expression (Gazulla et al., 2010; Linsinger, 2010):

$$\Delta_m = |C_m - C_{known}| \tag{4}$$

where Δ_m indicates the absolute difference between the mean measured and certified (known) value, C_m indicates the measured mean value, and C_{known} indicates the certified (known) value. However, both of the measurements have uncertainty. Therefore, the combined uncertainty of Δ_m is expressed as u_Δ by the following formula:

$$u_\Delta = \sqrt{(u^2_m + u^2_{known})} \tag{5}$$

where u_Δ is the combined uncertainty of the measured and certified value (known), that is the uncertainty of Δ_m, and u_m and u_{known} is the uncertainty of the measured value and the certified (known) value, respectively. Finally, the expanded uncertainty (U_Δ) is calculated by multiplying the combined uncertainty (u_Δ) by a coverage factor (k). The value of k is usually equal to 2, which corresponds to a confidence level of approximately 95%. Thus, expressed as:

$$U_\Delta = 2.u_\Delta \tag{6}$$

Finally, the method performance was evaluated by the comparison of Δ_m with U_Δ, which is, if $\Delta_m \leq U_\Delta$, then there is no significant difference between the measurement value and the certified (known) value of the analyzed sample.

Table 3. Comparison of the results obtained from the WD-XRF measurements with the certified reference value for the standard sample (JA-3) to determine the validity of the prepared calibration method.

Element (wt%)	**Certified Value [a] (mean ± SD)**	**Value Measured by WD-XRF (mean ± SD)**	**Δ_m**	**U_Δ**
K_2O	1.41 ± 0.06	1.32 ± 0.003	−0.090	0.120
CaO	6.24 ± 0.16	6.56 ± 0.014	0.318	0.321
TiO_2	0.70 ± 0.06	0.69 ± 0.004	−0.015	0.120
MnO	0.104 ± 0.01	0.105 ± 0.001	0.001	0.02
T-Fe_2O_3	6.60 ± 0.18	6.41 ± 0.012	−0.194	0.361
Sr [b]	0.0287 ± 0.0018	0.029 ± 0.0	0.0003	0.004

[a] Terashima et al., 1994 and Guevara et al., 2005. [b] Imai et al., 1995.

The excellent agreement between the measured and certified value, low detection limit, and low uncertainty from reproduced measurement confirm that the calibration method of WD-XRF for measurement worked well. However, in every step, like during oven-dried of the sample, sample mixing with the binder, making pressed pellets, and during measurement, we were cautious to avoid contamination.

2.2.3.5. Measurement of Element Concentration through WD-XRF Spectrometer

In addition to the ITRAX-XRF core scanning results, the quantitative concentrations of the selected elements (high abundance and being suitable for conventional XRF measurement), namely Sr, Fe, Mn, Ti, Ca, and K (**Figure 5**), were measured using a Wavelength Dispersive X-ray Fluorescence (Rigaku Supermini 200) spectrometer, at the University of Toyama, Japan. To confirm the reliability of ITRAX-XRF CS element count data, I prepared thirty-three discrete bulk sediment samples from the working half. These discrete bulk sediment samples were selected from the basis of significant minima, maxima, and changeover intervals indicated by the ITRAX-XRF CS records. The selection of discrete samples also covered all the sections and climate events, such as Heinrich Stadial 1 (HS1), Bølling-Allerød (B-A), Younger Dryas (YD), Preboreal (PB), and Holocene intervals, being demarked after the determination of age through the construction of the age-depth model (Subsection 3.3.1.). For the concentration measurement, the freeze-dried discrete samples were ground to a particle size < 63 μm. For the measurement of element concentration, the sample was prepared as described in the above section (Subsection 2.2.3.3.). Afterward, the pressed pellets sample concentration was measured using the prepared calibration curve (discuss in Subsection 2.2.3.3. and 2.2.3.4).

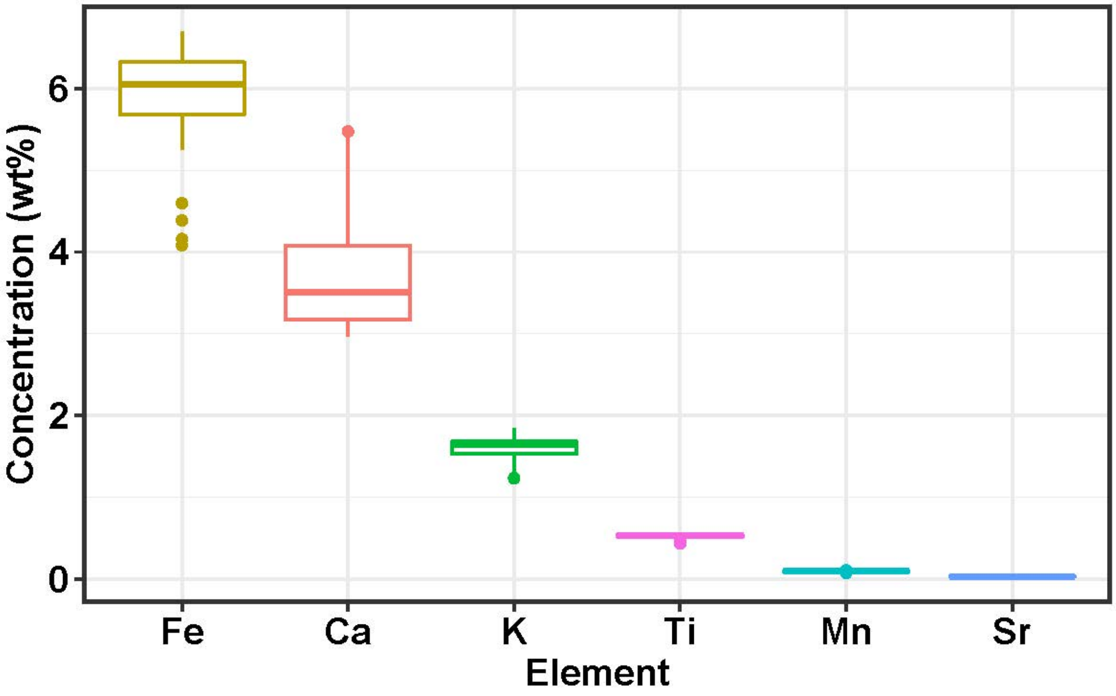

Figure 5. Boxplots of high abundance element determined by the conventional wavelength-dispersive X-ray fluorescence (WD-XRF, Rigaku Supermini 200) spectroscope from the discrete bulk sediment samples of the core CL14PC plotted concentration (wt%) versus elements (Sr, Fe, Mn, Ti, Ca, and K) in y- and x-axis, respectively. The pointed shape indicates the outlier of each of the elements.

2.2.3.6. Total Organic Carbon Analysis

The total organic carbon (TOC) was measured in the decarbonated bulk sediment sample of the core CL14PC. For this purpose, a total of 100 homogenized dried bulk ground sediments samples of ~200 mg each were decarbonated by adding 10 mL of 1 M HCl for each sample. Until the complete removal of the CO_2 bubbles, the samples were kept at room temperature and then centrifuged at 3000 rotations per minute (rpm) for 10 minutes, and the supernatant was discarded. After being rinsed three times with ultrapure water (18.2 MΩ·cm), the samples were utterly oven-dried at 50 °C (overnight). The TOC measurement was accomplished at the University of Toyama, Japan, using an elemental analyzer (Vario EL cube CHNOS). The total carbon (TC) and total nitrogen (TN) were measured from the dried bulk sediment using the same facility. For calibration, sulfanilamide ($C_6H_8N_2O_2S$) was used as a standard. The replicate measurements ($n = 4$) of the TOC samples had an RSD of 1.6%.

2.2.3.7. XRF Core Scanner Data Calibration

The variation of down-core physical properties and matrix effects affect XRF core scanner measurement and reduce scanning integrity (Tjallingii et al., 2007). Therefore, XRF CS data's calibration (normalization) is required to minimize the influence due to the matrix, specimen, or closed-sum effects. This study applied several techniques/approaches for the calibration of raw counts (cps) data, such as calibration by X-ray scattering, element ratio, total count (cps), and log-ratio transformation (Rothwell & Croudace, 2015; Gregory et al., 2019; Lee et al., 2019). All these approaches are categorized into two broad groups (methods), such as calibration by ratios (Subsection 2.2.3.8.) and log-ratio transformation (Subsection 2.2.3.9.). According to these methods, the XRF CS raw count (cps) data was normalized, after that, making a comparison based on their correlation with conventionally measured concentration.

A linear formula (Equation) was used to compare the conventional WD-XRF (wt%) measurement concentration with ITRAX-XRF CS values (cps), as:

$$\mathrm{W}_{ij} = a_i + \mathrm{I}_{ij} b_i \tag{7}$$

where W_{ij} is the concentration (weight) that is measured by WD-XRF (wt%) of element i at depth j, I_{ij} is the intensity (cps) measured by the ITRAX-XRF CS of element i at depth j, a_i is the y-intercept of element i, and b_i represents the slope of the regression line for element i.

2.2.3.8. Calibration by Ratios

One of the approaches for minimizing the potential complication/influence caused by the variation of the core physical properties or heterogeneities is the calibration of raw data using different variables ratios. Thus, calibrated data may increase the correlation with their actual concentration when compared to raw data. Therefore, we normalize the raw data by applying different approaches under this category, then compare the calibrated data with concentration (**Table 4**). The variables that were used to normalize the raw (initial) cps data were expressed as:

$$\text{Calibrated intensity } (I_{ij}) = \text{raw intensity } (I_{ij})/XS_j \tag{8}$$

$$\text{Calibrated intensity } (I_{ij}) = \text{raw intensity } (I_{ij})/TC_j \tag{9}$$

$$\text{Calibrated intensity } (I_{ij}) = \text{raw intensity } (I_{ij})/EI_j \tag{10}$$

where I_{ij} is the intensity (cps) measured by the ITRAX-XRF CS of element *i* at depth *j*, and XS_j in Equation (8) is the X-ray scatter at depth *j*. For X-ray scatter, we used the coherent/incoherent (coh/inc) X-ray scatter ratio (CIR), incoherent/coherent (inc/coh) X-ray scatter ratio (ICR), coherent X-ray scatter (coh), and the incoherent plus coherent (inc + coh) X-ray scatter (I + C). The TC_j shown in Equation (9) means the total count (TC) per second (total cps) at depth $_j$, and the EI_j in Equation (10) means the specific element intensity at depth $_j$. To normalize raw intensities in this study, we used two elements' intensities (Ti and Ca) as denominators in Equation (10).

2.2.3.9. Log-Ratio Transformation

The log-ratio transformation reduces the closed-sum effects and facilitates multivariate analysis (Weltje & Tjallingii, 2008). Two types of log-ratio transformation of data were employed in this study, namely, the additive log-ratio (alr) and centered log-ratio (clr) transformation. These log-ratio data transformations were calculated based on the following two equations (Lee et al., 2019):

$$\mathrm{alr}(I_{ij}) = \ln((I_{ij})/X_j) \tag{11}$$

$$\mathrm{clr}(I_{ij}) = \ln((I_{ij})/\mathrm{gm}_j) \tag{12}$$

where I_{ij} is the ITRAX-XRF CS intensities of element *i* at depth *j* and X_j is the variables applied for calculation at depth *j*. In this study, the CIR (coherent/incoherent) was used as the variable for initial raw intensities, and coh (coherent) as the variable for raw and CIR normalized intensities in Equation (11). In Equation (12), gm_j indicates the geometric mean at depth $_j$—for the calculation of centered log-ratio (clr), the geometric mean of the raw XRF data was used (mention as clr of raw data in **Table 4**). Besides, the clr was also calculated using the geometric mean of the coherent/incoherent X-ray scatter ratio (CIR) calibrated XRF data (mentioned as clr of CIR calibrated data in **Table 4**). For this, three groups of elements were made: (i) Sr, Fe, Mn, K, Ca, and Ti that was transformed in clr for comparison with WD-XRF concentration, (ii) Br and Cl for comparison with TOC, and (iii) Br/Cl ratio and Cl for comparison with TOC. The log-ratio (clr and alr) data transformations were executed using a compositional data package, CoDaPack 2.03.01 (Comas Cufí & Thió-Henestrosa, 2011), and/or R base ggplot2 package robCompositions.

2.3. Results

2.3.1. Raw X-Ray Fluorescence Core Scanner Data

In this study, the relationship between the ITRAX-XRF CS intensities (cps) was compared with WD-XRF measured concentration (wt%) using two different methods—linear regression through Pearson's method and Kendall's tau (τ) (**Table 4**) method. Kendall's tau (τ) method was used to confirm (cross-check) the correlation's accuracy that Pearson's method measured to avoid miscalculation. Therefore, hereafter, linear regression means that Pearson's method calculated linear correlation. Because Br and Cl are not elements analyzed using WD-XRF, the Br and Cl intensities are, thus, excluded for comparison with WD-XRF measured concentration. On the other hand, because Br and TOC are both productivity proxies and are related to organic matter content (Ziegler et al., 2008; Cartapanis et al., 2012; Seki et al., 2019), the ITRAX-XRF CS Br intensities were compared with TOC (wt%) through linear (R^2) regression and Kendall's τ (**Figure 6, Table 4**). In this study, the ITRAX-XRF CS raw cps data from the sediment core CL14PC were used as a baseline for comparison with different calibration methods.

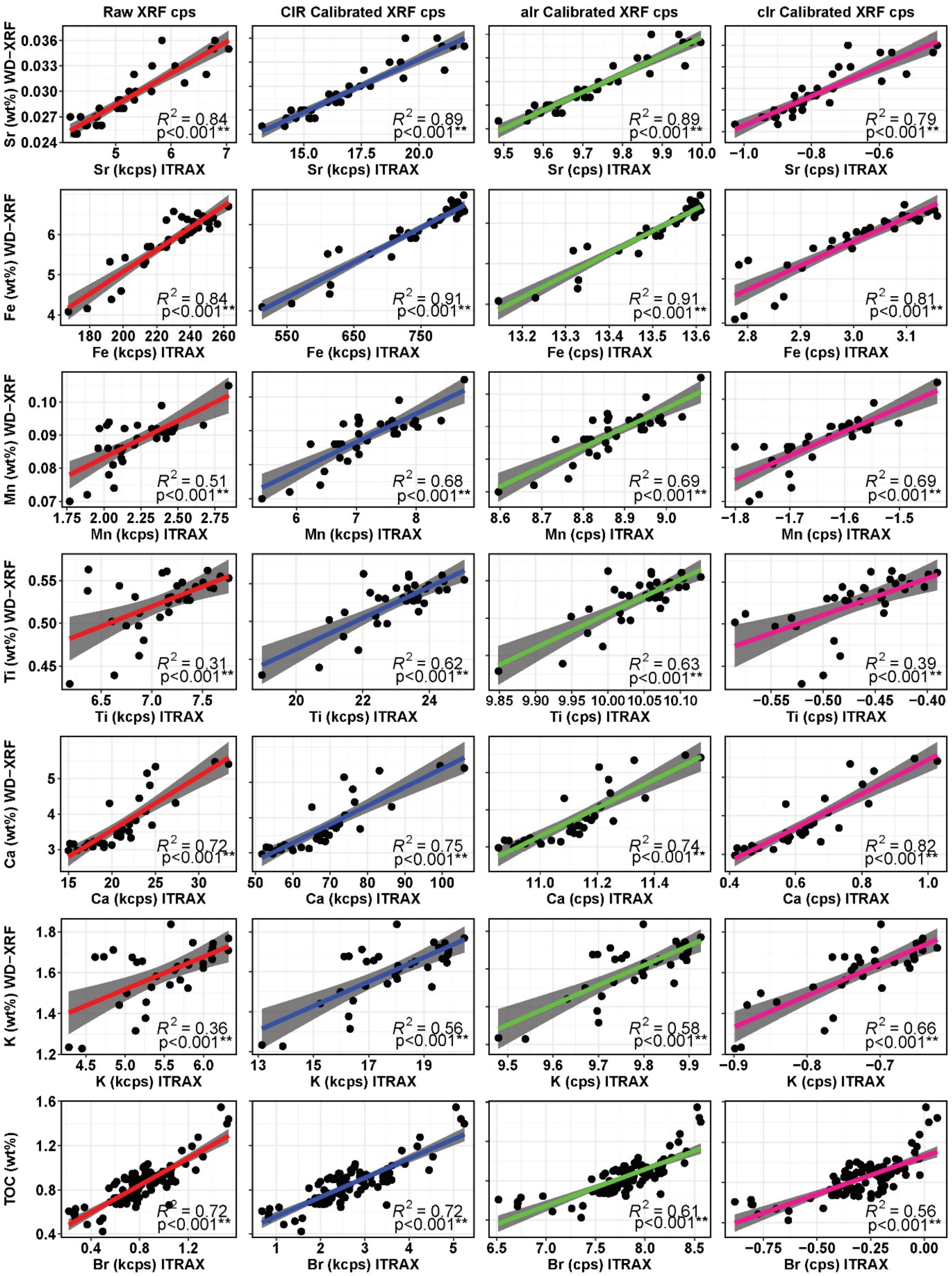

Figure 6. The comparison of correlation through linear regressions of ITRAX-XRF CS raw data (left side first column) and calibrated data by selected calibration approaches (from left to the right side) such as coherent/incoherent (coh/inc) X-ray scattering ratio (CIR), additive log-ratio transformation (alr) by Equation (11), and centered log-ratio transformation (clr) by Equation (12) with conventional WD XRF elemental concentrations (wt%) for element Sr, Fe, Mn, Ti, Ca, and K, and the Br with TOC(%). The y-axis is common for each element for all the approaches. In the x-axis, cps means count per second, and kcps means cps × 1000. The regression lines of raw and the CIR, alr, and clr calibrated data are presented by red, blue, green, and deep pink color, respectively, with a surrounded black shaded area representing a 95% confidence interval the regression lines.

The concentration (w%) of the bulk sediment samples was measured using a WD-XRF spectrometer. Among the six elements (Sr, Fe, Mn, Ti, Ca, and K), Fe and Ca showed high concentrations—5.83 (wt%) and 3.74 (wt%), respectively (**Figure 5**). A comparison of the correlation of raw counts (cps) with the WD-XRF measured concentration (wt%) showed $0.31 < R^2 < 0.84$ for linear regression (R^2) and $0.38 < \tau < 0.79$ for Kendall's method. The coefficients of determination (R^2) of the measured elements, i.e., Sr, Fe, Mn, Ti, Ca, and K, were 0.84, 0.84, 0.51, 0.31, 0.72, and 0.36, respectively (**Figure 6**). In the raw data, showing less (weak) correlation for Ti and K. In the case of Br and the Br/Cl ratio, the correlations (R^2) between the raw intensities and TOC (%) were 0.72 and 0.64, respectively, and, in Kendall's τ, the values were 0.60 and 0.53, respectively. In both cases (R^2 and τ), the relationship showed greater values in integral Br than the Br/Cl ratio (**Figure 6, Table 4**).

2.3.2. Calibrated X-Ray Fluorescence Core Scanner Data

In this study, the raw count (cps) data was calibrated into different procedures of two broad categories (group/method). The correlation (R^2) of calibrated cps through different X-ray scatter ratios with WD-XRF concentrations and TOC (%) were 0.56–0.91 for coherent/incoherent X-ray scatter ratio (CIR) calibrated data, 0.07–0.77 for incoherent/coherent X-ray scatter ratio (ICR) calibrated data, 0.05–0.74 for coherent (coh) calibrated data, and 0.0–0.69 for incoherent + coherent calibrated data (I + C) (**Table 4**). The raw intensity (cps) that was normalized by total counts, Ti, and Ca showed a correlation (R^2) with conventional concentration (WD-XRF) of 0.0–0.81, 0.27–0.86, and 0.0–0.64, respectively

(**Table 4**), under category ratio calibration. The log-ratio transformation of data (category log-ratio calibration) is an important procedure of XRF data calibration. It reduces closed-sum effects and is suitable for multivariate statistics (Aitchison & Egozcue, 2005; Weltje & Tjallingii, 2008; Lee et al., 2019).

The centered log-ratio transformation using raw and coherent/incoherent X-ray scatter ratio (CIR) calibrated data showed the exact correlation with concentration, and the range was 0.29–0.82 (**Table 4**). The additive log-ratio transformation by using CIR and coh as the denominator in the case of raw data in Equation (11) showed R^2 values of 0.58–0.91, and 0.05–0.76, respectively, when correlating with WD-XRF concentration and TOC (here, Br and Br/Cl compare with TOC) (**Table 4**). In the case of the coherent/incoherent X-ray scatter ratio, calibrated data transform in the additive log-ratio by using coherent (coh) X-ray scatter, as the denominator in Equation (11) showed R^2 values of 0.30–0.82 when compared with concentration and TOC% (**Table 4**).

Table 4. The Pearson's (R^2, through equation (7)) and the Kendall's Tau (τ) correlations results between ITRAX-XRF CS raw, ratio and log-ratio corrected element intensity (cps) data and WD-XRF concentration (wt%) results. For Br and Br/Cl, the correlation was calculated between ITRAX-XRF CS Br intensities (cps) and Br/Cl ratio with TOC (wt%).

Category		Correlation method	Correlation between ITRAX-XRF CS intensities (cps) with WD-XRF concentration ((wt%), *n* = 33), and TOC ((wt%), *n* = 100)							
			Element							
			Sr	Fe	Mn	Ti	Ca	K	Br v TOC	Br/Cl v TOC
Raw XRF CS		Pearson (R^2)	0.84	0.84	0.51	0.31	0.72	0.36	0.72	0.64
		Kendall's τ	0.79	0.66	0.47	0.38	0.71	0.41	0.60	0.53
Calibration by ratio	CIR[a]	Pearson (R^2)	0.89	0.91	0.68	0.62	0.75	0.56	0.72	0.64
		Kendall's τ	0.83	0.78	0.55	0.45	0.73	0.48	0.61	0.53
	ICR[b]	Pearson (R^2)	0.77	0.62	0.32	0.07	0.69	0.17	0.70	0.64
		Kendall's τ	0.73	0.55	0.38	0.29	0.68	0.30	0.59	0.53
	coh[c]	Pearson (R^2)	0.74	0.64	0.33	0.05	0.72	0.18	0.70	0.64
		Kendall's τ	0.75	0.61	0.37	0.30	0.70	0.32	0.60	0.52
	I + C[d]	Pearson (R^2)	0.69	0.45	0.22	0.00	0.68	0.07	0.68	0.64
		Kendall's τ	0.67	0.53	0.29	0.18	0.66	0.24	0.59	0.53
	Total count (cps)	Pearson (R^2)	0.81	0.69	0.25	0.00	0.75	0.15	0.72	0.64
		Kendall's τ	0.77	0.57	0.27	0.09	0.71	0.30	0.61	0.52
	Ti intensity (cps)	Pearson (R^2)	0.85	0.86	0.56	-	0.82	0.27	0.65	0.64
		Kendall's τ	0.84	0.80	0.56	-	0.75	0.32	0.57	0.52
	Ca intensity (cps)	Pearson (R^2)	0.00	0.64	0.51	0.46	-	0.63	0.52	0.64
		Kendall's τ	-0.09	0.74	0.67	0.57	-	0.62	0.49	0.52
Calibration by log-ratio	clr[e] of CIR calibrated data	Pearson (R^2)	0.79	0.81	0.69	0.39	0.82	0.66	0.56	0.29
		Kendall's τ	0.78	0.81	0.70	0.56	0.76	0.62	0.52	0.33
	clr of raw data	Pearson (R^2)	0.79	0.81	0.69	0.39	0.82	0.66	0.56	0.34
		Kendall's τ	0.78	0.81	0.70	0.56	0.76	0.62	0.52	0.36
	alr[f] by CIR	Pearson (R^2)	0.89	0.91	0.69	0.63	0.74	0.58	0.61	0.60
		Kendall's τ	0.82	0.79	0.58	0.45	0.74	0.48	0.61	0.55
	alr by coh after CIR calibration	Pearson (R^2)	0.82	0.82	0.52	0.30	0.74	0.40	0.58	0.52
		Kendall's τ	0.79	0.75	0.52	0.49	0.72	0.42	0.61	0.50
	alr by coh	Pearson (R^2)	0.76	0.66	0.32	0.05	0.67	0.17	0.59	0.52
		Kendall's τ	0.75	0.61	0.37	0.30	0.70	0.32	0.60	0.50

[a] CIR = coherent/incoherent (coh/inc) X-ray scatter ratio, [b] ICR = incoherent/coherent (inc/coh) X-ray scatter ratio, [c] coh = coherent (coh) X-ray scatter, [d] I + C = incoherent + coherent (ich + coh) X-ray scatter, [e] clr = centred log-ratio, [f] alr = additive log-ratio.

2.4. Discussion

2.4.1. Sediment Physical Properties Affect Scanning Intensities

In the sediment core, the top sediments are generally characterized by higher porewater contents expressed by high Chlorine (Cl) content, especially in marine sediments, because Cl is a major dissolved element of seawater. The scenario is different in lacustrine and other freshwater sediments. Because lacustrine and freshwater sediments contain extremely low Cl content. The XRF intensity of Cl is used as a water content proxy for marine sediment (Tjallingii et al., 2007). The Cl intensity in the core CL14PC significantly increases in the topmost part, especially in the upper 202 cmbsf depth (**Figure 7**), suggesting high interstitial/porewater content. At depth 201 cmbsf, the Cl intensity (cps) increases 29% from depth 202 cmbsf Cl cps, and in the top 202 cmbsf, the average Cl content (cps) increases 42% compared to the down-core average Cl (cps) content. In the core top, the high Cl intensity (cps), indicating high water content, influences X-ray scatter and element intensity measurement. The Cl intensity also exhibits elevation in the down-core at 793–766 cmbsf depth.

The wet bulk density (gm/cc) at the top of the core from depths 202 to 25 cmbsf did not show extreme variation (**Figure 7**). However, at the top-most 25 cmbsf, the density sharply decreases from 1.82 to 1.03 gm/cc, and the average Cl content increases 73% compared to the down-core average Cl content below 202 cmbsf depth. At a depth of 766 to 737 and 716 to 676 cmbsf, the wet bulk density (gm/cc) was more prominently low (**Figure 7**). At that depth, the Br (cps) content was significantly high. Br has been used as a good proxy for marine organic matter and related productivity tracer in the ocean basins (Ziegler et al., 2008; Cartapanis et al., 2012; Seki et al., 2019). These high Br intensity intervals are characterized by organic-rich marine sediments (high TOC and low TOC/TN molar ratio) that are derived from marine algal sources with a dark area (seen in CT-scan photography in **Figure 3**) and low density. In that depth, the bulk density variation (gm/cc) inversely reflects the X-ray scattering. Although a lower sedimentary density at 766–737 and 716–676 cmbsf depth increases the X-ray scattering, with Compton (incoherent) scatter (Thomson et al., 2006) being remarkably high, after correction, the pattern of variation of the element intensity (cps), especially Br and Ca (related to organic matter), did not significantly change (Subsection 2.4.3.). Thus, strengthening the water content was responsible for the deviation of the scanning intensity. Therefore, in this study, the coherent/incoherent X-ray scatter ratio calibration of raw intensity showed a high correlation with WD-XRF measured concentration. The coherent/incoherent scatter (inc/coh) ratio (CIR) is used for the calibration of raw intensity (cps), where water content has a more significant influence (Boyle et al., 2015; Gregory et al., 2019). Meanwhile, some researchers have used X-ray scattering (incoherent/coherent ratio) to correct raw XRF counts when the organic matter has a more significant influence (Chagué-Goff et al., 2016; Oliva et al., 2018).

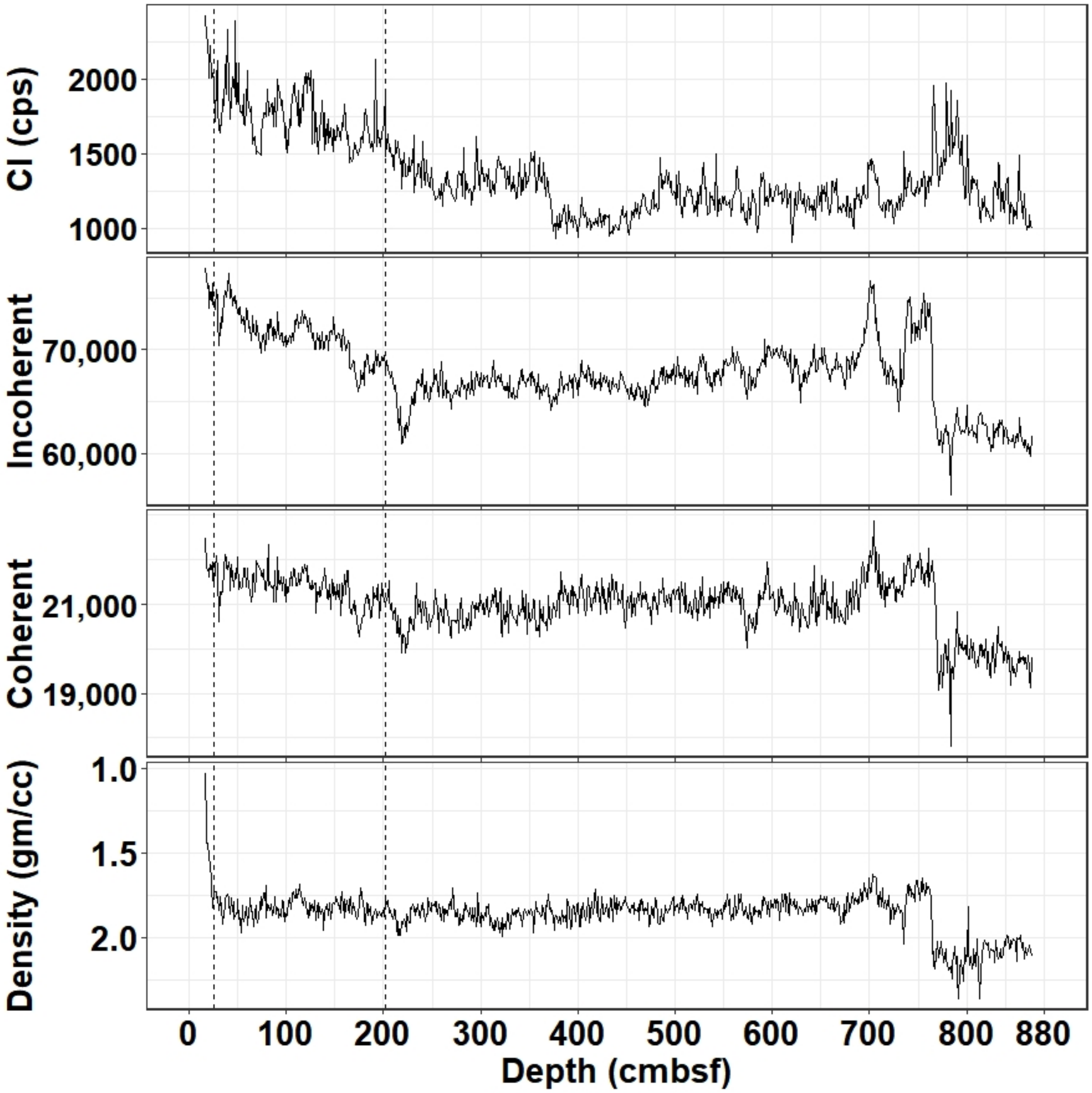

Figure 7. The Cl counts (cps), X-ray scattering of incoherent and coherent, and the wet bulk density (gm/cc) are plotted versus depth (cmbsf) in y- and x-axis, respectively, of the core CL14PC. The vertical black dash line at 202 and 25 cmbsf indicates the porewater Cl content increasing abruptly toward the core top.

2.4.2. Element Intensities Calibration by Ratios

The correlation (R^2) that was calculated between the raw counts and WD-XRF concentrations (wt%) of lighter elements, especially Ti and K, showed a weak relationship (**Figures 6 and 8**), and the scattering distance from the regression line increased (**Figure 6**).

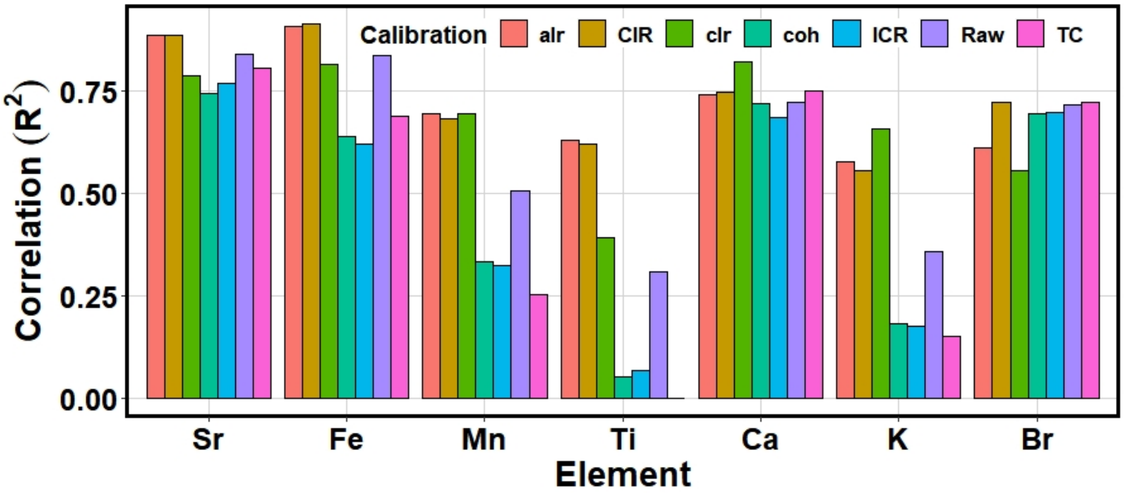

Figure 8. The coefficients of determination (R^2) calculated from ITRAX-XRF CS raw and calibrated (alr, CIR, clr, coh, ICR, and TC (total count)) data with conventional WD-XRF concentration are plotted in the y-axis, and the elements in the x-axis for comparison. Here, only presented the correlation (R^2) results of six calibration approaches and raw data; for detail, see the text and **Table 4**.

The ITRAX-XRF CS Cl counts exhibited increasing values toward the core-top, and, inversely, the K and Ti intensities decreased at the horizon. That might be a primary factor in artificially influencing element counts through inaccurate or imprecise detection throughout the core. In addition, a previous study (Croudace et al., 2006) reported that the higher porewater content influences K through the absorption of the Kα fluorescence of K by seawater Cl atoms. Ti might also be influenced by higher porewater content (Hennekam & de Lange, 2012) because porewater increases the looseness and decreases the compaction in sediments. Under ratio calibration methods, the initial raw intensity data were calibrated using coherent/incoherent X-ray scatter ratio (CIR), incoherent/coherent X-ray scatter ratio (ICR), coherent X-ray scatter (coh), incoherent + coherent X-ray scatter (I + C), total count (cps), Ti, and Ca element intensity. Among these approaches, the calibration of raw K intensity (cps) through Ca intensity and CIR yields the highest correlation, with WD-XRF concentrations of 0.63 and 0.56, respectively, in linear regression and 0.62 and 0.48, respectively, for Kendall's τ (**Table 4**). We found the correlation (R^2) values for K and Ca to be slightly increased when being normalized by Ca and Ti intensities (element ratio), respectively, as compared to CIR normalization. The geochemically antipathetic behavior of Ca with respect to K or Ti (Hennekam & de Lange, 2012) as the atomic numbers of K (19), Ca (20), and Ti (22) are nearly identical, enhanced the correlation with concentration. However, the element ratio calibration does not entirely avoid artifacts due to porewater or matrix effects for other elements (Sr, Fe, Mn, Ti, and Br) because the X-ray attenuation due to matrix effects fluctuates with photon energy (Boyle et al., 2015). Therefore, the calibration of raw data through element ratios (here using Ca and Ti intensities as the denominator) did not provide a good result for all elements and diverged from correlation values that were found in the CIR calibration methods in this study. In the case of Ti, the CIR calibrated intensities showed a more significant correlation ($R^2 = 0.62$) with WD-XRF concentration than raw data. For both elements (K and Ti), the correlation with WD-XRF concentration significantly increased in CIR calibrated data, for which Ti increased 100%, and K increased 56% from raw correlation. Similarly, the calibration of raw intensity (cps) through CIR for the elements Sr, Fe, Mn, and Ca showed a more significant correlation with WD-XRF concentration when compared to other ratio calibration processes (approaches).

The relationship between the Br count and TOC (wt%) presented a slight deviation in the uppermost part of the core CL14PC marked by an interval of high Cl (porewater) content. Because seawater Br sometimes overprints on algal Br, the XRF Br count intensities are sometimes normalized by Cl counts. Although the Br/Cl ratio seems to work as a good tracer with TOC in the upper part of the core, it does not have good agreement with TOC variation in the downcore trends of the core, and it has a lower correlation with TOC ($R^2 = 0.64$, $n = 100$) when compared to integral Br (**Table 4**). However, the correlation of CIR-calibrated Br intensities ($R^2 = 0.7215$) showed a minor increase or almost similar values compared to raw correlation ($R^2 = 0.7156$) (**Figure 6**). This heavier ($Z = 35$), high-atomic weight (80), and high-excitation ($K\alpha = 11.9$ keV) energy element (Ziegler et al., 2008; Addison et al., 2013) is relatively unaffected, and, in most cases, the magnitude of Br cps in CIR calibration increases or decreases proportionately with the relation of raw cps variation.

2.4.3. Element Intensities Calibration by Log-Ratios

When transformed through centered log-ratio (clr) for the raw and CIR calibrated cps, the geometric mean varies in a similar proportion and after transformation, thus making similar values in both cases. Therefore, we found similar correlation values when compared with concentration (WD-XRF) (**Table 4**). However, exceptions occur when Br/Cl raw data and the Br/Cl CIR ratio were separately transformed with Cl through clr—they make different geometric means and calibrated intensities (cps). Therefore, the CIR-calibrated clr Br/Cl ratio data (R^2 = 0.29) and raw clr Br/Cl ratio data (R^2 = 0.34) have different correlations with concentration (TOC) (**Table 4**). In the centered log-ratio approach, the correlation (R^2) values for Ti, K, and Mn were 0.39, 0.66, and 0.69, respectively (Table 4). The R^2 value in the case of K slightly increases in the clr log-ratio transformation method, but, in Ti, the value significantly decreases compared to the CIR ratio calibration discussed in the above section (Subsection 2.4.2). The correlation between clr calibrated intensity with concentration (WD-XRF and TOC) for Sr, Fe, Ca, and Br were 0.79, 0.81, 0.82, and 0.56, respectively. Although, Lee et al. (2019) suggested that the calibration of data through clr transformation was better than alr transformation and ratio calibration in lacustrine (lake) sediment. However, in this study, the CIR approaches showed a better performance than clr approach, suggesting that the calibration of XRF data is not method-specific—it may vary according to sediment samples, sample condition, region, and/or depend on the scanning instrument.

In the additive log-ratio calibration approach (Weltje & Tjallingii, 2008; Lee et al., 2019), when the raw cps was transformed using the CIR (coh/inc) ratio as the denominator, the values showed a good correlation with concentration (WD-XRF and TOC) (**Table 4**). The correlation (R^2) with concentration (WD-XRF and TOC) for the elements Sr, Fe, Mn, Ti, Ca, K, and Br were 0.89, 0.91, 0.69, 0.63, 0.74, 0.58, and 0.61, respectively. Although the relationship between ITRAX-XRF CS intensities and WD-XRF concentration through the alr and CIR calibration approach showed almost similar values for the elements Sr, Fe, Mn, Ti, Ca, and K, different results were found for the Br intensities when compared with TOC. The relationship between Br intensities and TOC increased by 0.11 in the CIR calibrated data compared to the alr log-ratio calibrated data. However, the goodness of fit for additive log-ratio depends on which parameters or elements are used as the denominator for data transformation. The wrong selection significantly influences the actual agreement.

However, the relationship (correlation) between ITRAX-XRF CS data and the concentration that conventional WD-XRF measured in the CIR ratio calibration method shows good agreement (Gregory et al., 2019). The correlation values in the CIR approach were increased from the values of the raw relationship in all of the selected elements (Sr, Fe, Mn, Ti, Ca, K, and Br) in this study (**Figure 6 and Table 4**). The coefficient of determination of all the elements was above 0.50 ($R^2 > 0.50$) in the CIR calibrated data using the ratio method. Of which the values of lighter elements (Mn, Ti, K) improved significantly from raw values (**Figure 9**), although Tjallingii et al. (2007) mentioned that K and Ti were relatively unaffected by the variation of core physical properties (water content). The relationship that was measured by Kendall's tau (τ) method also showed a positive correlation (τ correlation) of all the elements that were higher than the raw data τ correlation (**Table 4**).

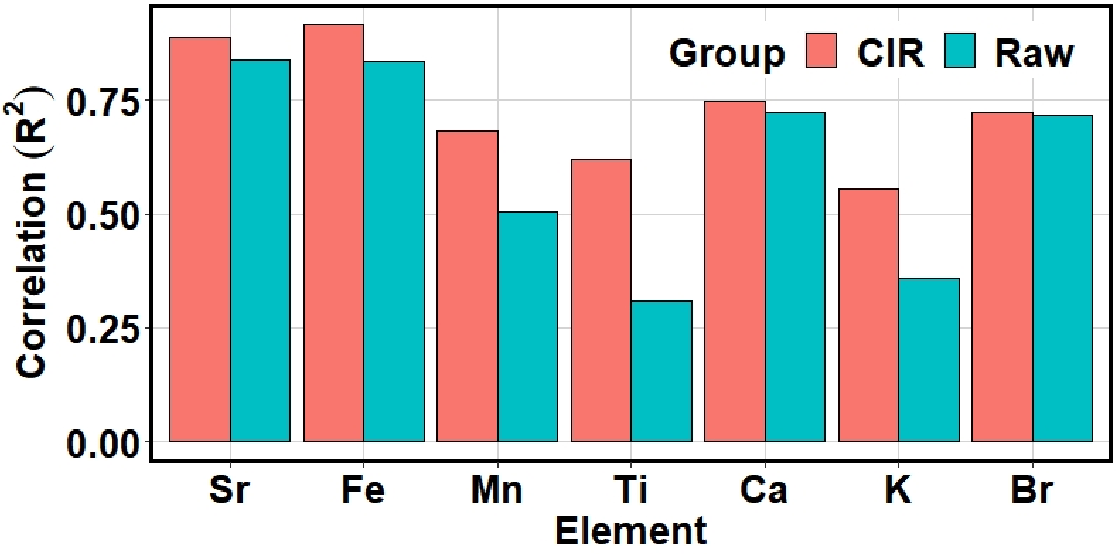

Figure 9. The comparison of correlation (R^2) was determined from ITRAX-XRF CS raw data and the CIR calibrated data versus WD-XRF concentration by a linear regression method. In the case of Br, the correlation was determined between Br versus TOC (wt%). The measured coefficient of determinations (R^2) plotted versus different elements (Sr, Fe, Mn, Ti, Ca, K, and Br) in the x-axis.

From the above evaluation, it can conclude that the raw cps that were calibrated by coherent/incoherent X-ray scatter ratio (CIR) (i.e., element intensity/CIR) is the best fit for the calibration or normalization of X-ray fluorescence scanning data. Therefore, based on this result, we applied the coh/inc X-ray scatter ratio (CIR) to calibrate the entire raw cps data (**Figure 10**, violet color) of the core CL14PC. In the calibrated data, the element intensity (cps) was rescaled compared to raw cps, and the relative magnitude of the minima and maxima was changed. In the upper part, the calibrated cps showed a substantially higher magnitude of increase relative to raw cps, particularly for Sr, Fe, Mn, Ti, and K (**Figure 10**), where the Cl XRF intensity (cps) was higher. The down-core profile for almost all of the elements studied in this experiment showed a high or low scale of magnitude compared to the raw intensity (cps) variation.

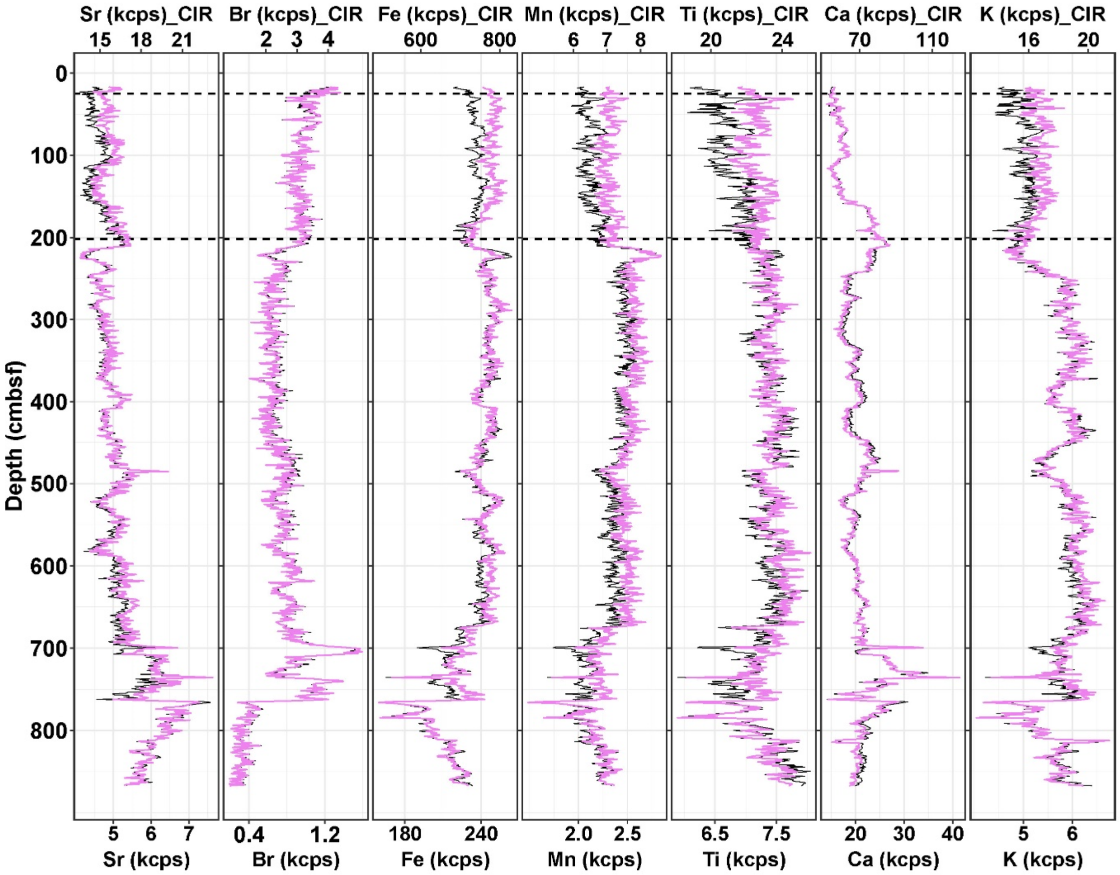

Figure 10. The corrected intensity (kcps, violet color) through the CIR calibration and the raw intensity (kcps, black color) from ITRAX-XRF CS count for the element Sr, Br, Fe, Mn, Ti, Ca, and K is plotted versus core depth in centimeter below seafloor scale (cmbsf). The black dash line at 202 and 25 cmbsf indicates the boundary of the high porewater influence in the core top. Here, kcps = cps * 1000.

2.5. Conclusions

In this study, the ITRAX X-ray fluorescence core scanner was run by using a Molybdenum (Mo) X-ray anode tube at a 30 kV voltage and 55 mA current with a 20-s exposure time for the scanning of a wet marine sediment piston core that was collected from the Northeastern Gulf of Alaska continental margin. The ITRAX provides high counts (cps) for the elements Sr, Fe, Mn, Ti, Ca, K, Br, and Cl, with relatively low RSD (%). The Cl intensity increases toward the top of the core, with an average increase of 42% compared to the down-core average cps (the dividing point at depth 202 cm below seafloor scale). In the down-core, at the depth 793–766 cm below the seafloor, the Cl content also exhibited elevated values. The high Cl content indicated high seawater content because, in marine sediments, the XRF Cl intensity is expressed as the seawater content. Thus, this significantly affects the correlation between raw counts and concentration measured by WD-XRF spectrometer, especially the lighter elements (K and Ti), which are affected greatly. In this study, we compile several normalization processes under two calibration methods—ratio and log-ratio—sporadically applied in different research works. Therefore, in the future, relevant researchers can utilize these multiple approaches to test their multi-sensor datasets and find the best correction method for their datasets. However, these various techniques were tested in the sediment core CL14PC to determine the best way to normalize the raw intensity data that eliminates the effects and provides the highest accuracy from raw counts. Among the calibration approaches, the correction of the raw cps by coherent/incoherent X-ray scatter ratio (CIR) (i.e., element intensity/CIR) showed the best performance when correlating with concentration. The correlation measured through linear regression with Pearson’s method and Kendall’s tau (τ) method substantially increased in the CIR normalization using the ratio calibration method compared to raw correlation. Compared to the initial correlation, the correlation increased in lighter elements by 100%, 56%, and 33% in Ti, K, and Mn, respectively. Therefore, based on the above evaluation, it can conclude that the normalization of ITRAX-XRF core scanner initial data by coherent/incoherent X-ray scatter ratio (CIR) can be applied for marine-based sediments to obtain good multi-elemental records through minimizing the effects due to the core physical properties. Thus, it may further increase the reliability of using XRF core scanning data.

Chapter 3. Glacial meltwater injection into the northern Gulf of Alaska from Cordilleran Ice Sheet during the last deglaciation

Abstract

The timing and sources of meltwater injection due to the decay of the Cordilleran Ice Sheet (CIS) during the last deglaciation have not yet been well constrained, even though they might have potential perturbating effects on the thermohaline circulation. To constrain the timing of meltwater discharge associated with the CIS retreat during the last deglaciation and their potential source areas, we measured $\%C_{37:4}$ alkenones, planktonic foraminifer $\delta^{18}O$, ice-rafted debris (IRD), and detrital Sr-Nd isotopic compositions from core CL14PC in the northern Gulf of Alaska (GOA). The multiple concomitant higher values of IRD deposition and $\%C_{37:4}$ alkenones were found at ~16.4, ~16.2, and ~15.6 ka during Heinrich Stadial 1 (HS1), suggesting collapsing of the CIS at multiple times. Unusually low salinity conditions inferred from higher $\%C_{37:4}$ alkenones values (24% and 28%) were also found at ~14.1 and ~13.9 ka, respectively, during the early Bølling-Allerød (B-A), which was accompanied by depleted planktonic foraminifer $\delta^{18}O$ values. This evidence confirms that multiple meltwater injections also occurred in the early B-A as expected by ice sheet model studies but not deduced from planktonic foraminifer $\delta^{18}O$ alone. Furthermore, a prominently higher and long-lived peak of $\%C_{37:4}$ alkenone was found during the middle Younger Dryas, which would partly reflect lower salinity conditions related to the decay of the northern part of the CIS. The integrated analyses of this study demonstrate that all these sources of the deglacial meltwater are likely proximal to the core site (i.e., the northern part of the marine-and land-based CIS). This study observed that the northern GOA would have received multiple meltwater injections during HS1 and at least three times during 14.6–12.2 ka from B-A to YD, indicating temporally disaggregated meltwater events. These longer contributions of CIS meltwater in view of global sea-level rise were minor. However, their impact on the freshwater budget in the northeastern Pacific during the abrupt global sea-level rise (14.6–14.3 ka) was relatively small.

3.1. Introduction

During the last glacial maximum (LGM, 19–26 ka), northern North America was covered by the North America Ice Sheet complex consisting of the smaller Cordilleran Ice Sheet (CIS) in the west and a larger Laurentide Ice Sheet (LIS) in the center and east (Seguinot et al., 2016) (**Figure 11**).

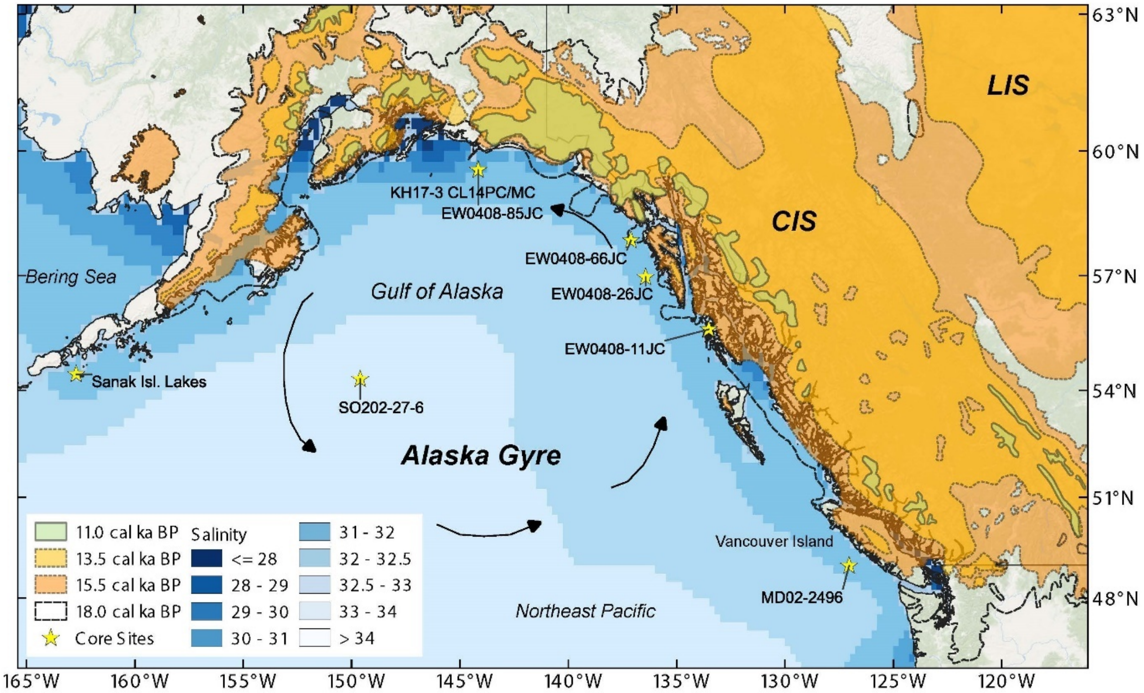

Figure 11. Core's locations and hydrography in the map in the northern Gulf of Alaska. The site of the core KH17-3 CL14PC/MC (this study), EW0408-85JC (Davies et al. 2011), EW0408-66JC, EW0408-26JC, and EW0408-11JC (Barron et al. 2009; Praetorius and Mix 2014), MD02-2496 (Taylor et al., 2014), SO202-27-6 (Maier et al., 2018), and Sanak Isl. Lakes (Misarti et al., 2012) in the Northeast Pacific indicated a yellow star. The baseline map was generated by QGIS (https://www.qgis.org/en/site). The mean seasonal (summer) sea-surface salinity profile in the background map taken from the World Ocean Atlas 2013 data set (https://data.nodc.noaa.gov/thredds/catalog/nodc/archive/data/0114815/public/salinity/netcdf/decav/0.25/catalog.html). The North American CIS and the LIS extent at 18.0, 15.5, 13.5, and 11.0 (^{14}C) cal ka BP are also shown (Dalton et al., 2020). The generalized surface circulation pattern and the current system of the subarctic Northeast Pacific are indicated by black arrows.

The maximum ice volume of the CIS-LIS was 64–82 m sea-level equivalent, and the CIS had an ice mass comparable to that of the present-day Greenland Ice Sheet (Clark and Mix 2002; Seguinot et al. 2016). During the last deglaciation, the retreat of the CIS-LIS provided a large amount of meltwater into the adjacent Pacific, Arctic, and Atlantic Oceans, which is thought to have influenced the thermohaline circulation and, therefore, global climate (Clark et al. 2001, 2002; Tarasov and Peltier 2005). Furthermore, the retreat of the CIS-LIS should have also created a viable route that allowed the first humans to migrate into the Americas from Beringia (~16 ka), influencing human dispersion (Mann and Peteet 1994; Llamas et al. 2016; Lesnek et al. 2018).

Previous studies using ^{14}C and ^{10}Be dating of erratic boulders and bedrock surfaces in the former CIS-covered regions have shown a detailed history of the CIS decay: (1) marine-based CIS margins were in retreat by ~17 ka due to sea-level rise and subsurface warming at the grounding line (Cosma and Hendy 2008; Misarti et al. 2012; Praetorius and Mix 2014; Taylor et al. 2014; Lesnek et al. 2018, 2020); (2) the CIS-LIS became physically separated between 15.7 ka and 14 ka (13.5 to 12 ^{14}C ka BP) (Dyke 2004; Munyikwa et al. 2011; Gregoire et al. 2012) although modeling studies indicate that the CIS-LIS remained joined until 13.5 ka (Lambeck et al., 2017) or that the separation was completed by 14.5 ka (Peltier et al., 2015). Another recent study indicated that the CIS-LIS separated between ~15.5 and 14.9 ka (Dalton et al., 2020); and (3) substantial areas covered by the CIS were ice-free by the end of the Younger Dryas (YD) (Menounos et al., 2017) (**Figure 11**).

These ^{10}Be moraine-erratic boulder chronologies and glacio-isostatic adjustment (GIA) ice-sheet models show that the CIS had lost almost one-half of its LGM mass in just 500 years during the early Bølling–Allerød (B-A) warm period (14.5–14.0 ka), causing 2.5–3.0 m of sea-level rise (Lambeck et al. 2014; Peltier et al. 2015; Menounos et al. 2017). However, assumptions for ^{10}Be exposure-age calculations, such as elevation correction, snow shielding or erosion, and inherited muogenic (muon-generated) ^{10}Be contamination, make constraining the timing of volumetrically substantial meltwater injection into the northeastern North Pacific challenging.

Typically, continental margin sediments in the Gulf of Alaska (GOA), the vicinity of the former CIS, register a high time-resolution CIS decay history (Taylor et al., 2014). Thus, sedimentary archives can also be useful for reconstructing the detailed timing of glacial meltwater injection. Previous studies which were documented from the vicinity of the former

CIS conducted a paired analyses of $U^{k'}_{37}$–derived sea-surface temperature (SST) and planktonic foraminifer $\delta^{18}O$ (*Globigerina bulloides*), and argued that the GOA experienced less saline surface conditions during the early deglaciation and YD due to a large amount of meltwater injection from the land-based CIS, rather than the B-A warm period of 14.5–14.0 ka (Praetorius et al. 2015, 2020). However, the less saline surface conditions derived from the debatable assumption that both alkenone-producing haptophytes and *G. bulloides* reflect a water mass in the same season and at the same depth.

To test their argument on massive meltwater injection at YD and to fully understand meltwater injection history (i.e., the timing and sources) throughout the last deglaciation from the CIS into the GOA, this study reconstructed a new salinity proxy record based on $\%C_{37:4}$ alkenones as well as other paleoceanographic records, such as ice-rafted debris abundance, detrital Sr-Nd isotopes, and high-resolution planktonic foraminifer $\delta^{13}C$ and $\delta^{18}O$ records.

3.2. Coastal oceanography in the Gulf of Alaska

The Subarctic North Pacific consists of the Alaska Gyre (AG) in the east and the western subarctic gyre in the west (**Figure 11**). The Alaska Coastal Current (ACC) originates from the AG flowing counterclockwise along the continental shelf in the GOA, which is driven by strong along-shore winds (Stabeno et al. 2004, 2016). The ACC is also marked by freshwater inputs from precipitation and discharge from glacial rivers and streams with higher particulate and dissolved iron (Royer 2005; Lippiatt et al. 2010). That results in relatively low-salinity (25–31, (Mundy 2005; Hallmann et al. 2011)) and high-productivity water masses (Stabeno et al. 2004; Lippiatt et al. 2010). The low-salinity ACC intrudes into the Bering Sea and then flows into the Arctic Ocean (Kipphut, 1990; Weingartner et al., 2005; Hallmann et al., 2011), modulating a freshwater budget in the Arctic Ocean.

The seasonal variations of temperature and salinity in the top 100-m water depth in the continental shelf of the GOA are shown in **Figure 12**, where ACC influences and the core sites are located. On the continental shelf of the GOA, intensified onshore winds create the strongest coastal downwelling during winter (Childers et al. 2005; Royer 2005), and much of the precipitation is accumulated on land as snow and, consequently, river runoff decreases. In addition to the decline in river runoff rates, a deeper mixed layer and lower light conditions are attributed to lower primary productivity (Strom et al., 2006; 2010; Costa et al., 2018).

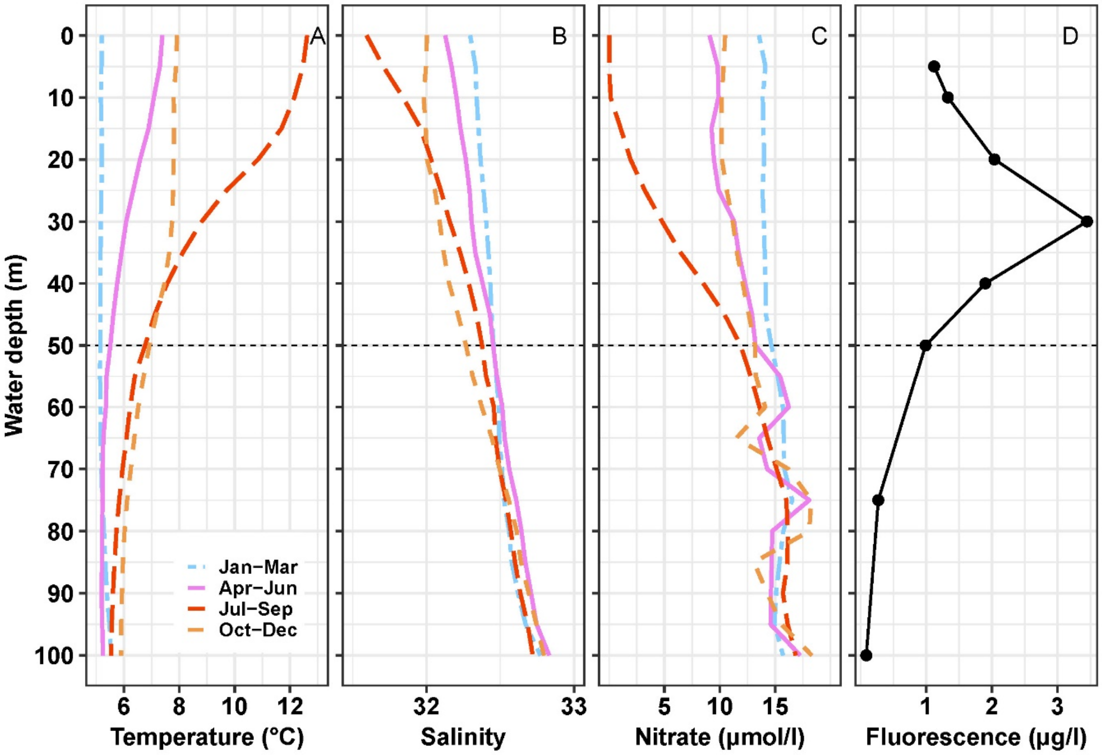

Figure 12. Seasonal variation of the oceanographic parameters in the core-site. The modern (1955–2012) seasonal in situ: A. temperature (°C), B. salinity, and C. nitrate (µmol/l) profiles (0–100 m water depth) showing during the Jan-Mar (January-March, Sky Blue color thick two-dash vertical line), Apr-Jun (April-June, Violet thick solid vertical line), Jul-Sep (July-September, Orange Red color thick long-dash vertical line), and Oct-Dec (October-December, Tan color thick dash vertical line) of the hydrological stations 34 631-B (World Ocean Atlas 2013, https://odv.awi.de/data/ocean/world-ocean-atlas-2013/), located nearby of this studied core. The top 50-m of the water column, where planktonic foraminifera (*Neogloboquadrina pachyderma* (s)) dwelled predominantly during summer, is marked by the horizontal dash line. (D) The Chlorophyll fluorescence (µg/l) data (0–100 m water depth) was collected at the core site via CTD on July 21, 2017.

In contrast, the relaxed onshore winds in early spring to early summer allow the creation of coastal upwelling, which promotes large algal blooms at relatively shallower depths over the shelf (Stabeno et al., 2004). During summer, low-salinity and warm surface waters result in maximum stratification, forming a shallow mixed layer (Whitney and Freeland 1999; Stabeno et al. 2004) (**Figure 12**) as the subsurface chlorophyll maximum was observed at a depth of 30 m at the CL14PC core site during the KH17-3 Cruise (July 21, 2017), which is associated with the top of the nitracline and pycnocline (~30–40 m) (**Figure 12**).

Globigerina bulloides and *Neogloboquadrina pachyderma* (sinistral) are found abundantly in the GOA sediments and have been used to reconstruct oceanographic conditions based on the chemical characteristics of their shells (Davies et al. 2011; Taylor et al. 2018). *G. bulloides* is found from spring to late autumn in the subarctic North Pacific (Sautter and Thunell 1989; Asahi and Takahashi 2007; Taylor et al. 2018). The main habitat depth of *G. bulloides* is thought to be just below the mixed-layer depth, associated with the chlorophyll maximum (Schiebel et al. 2001; Kuroyanagi and Kawahata 2004; Iwasaki et al. 2017). *N. pachyderma* (s) is a (sub)polar species and prefers ocean temperatures cooler than 8 °C (Reynolds and Thunell 1985; Kuroyanagi and Kawahata 2004). Studies employing sediment traps in the North Pacific show that *N. pachyderma* (s) flux varies regionally; however, it often exhibits peaks in abundance during spring and late summer/autumn (Sautter and Thunell 1989; Asahi and Takahashi 2007; Iwasaki et al. 2017; Taylor et al. 2018). The calcification depth estimated from the δ^{18}O values of *N. pachyderma* (s) is just below the base of the mixed layer in the subpolar North Atlantic (Jonkers et al., 2010), and *N. pachyderma* (s) in the western North Pacific could occur near the pycnocline at depths of 25–45 m in summer and 45–65 m in winter (Kuroyanagi et al., 2011). According to plankton tow data during summer in the subarctic North Pacific, *N. pachyderma* (s) occurs predominantly in the top 50-m of the water column, and its abundance was also tied to food availability, such as *G. bulloides* (Taylor et al., 2018). However, in a recent study by analysis of the CTD and multinet data, Taylor et al. (2018) recommended that the *G. bulloides* and *N. pachyderma* (s) predominantly found within 0 to 50 m water depth in the North Pacific during spring of March to June. Given that the habitat depths of *G. bulloides* and *N. pachyderma* (s), their seasonal abundance and ecological drivers, and oceanographic conditions in the coastal GOA, their δ^{18}O and δ^{13}C values should record subsurface conditions from spring to late summer/autumn. This inference leads us to expect that the chemical characteristics of both planktonic foraminifer shells would be ideal for detecting changes in sea surface conditions ($\delta^{18}O_{sw}$ and temperature) related to meltwater injections and/or seawater warming.

3.3. Materials and methods

3.3.1. Sediment core CL14PC and age-depth model

The piston core CL14PC was collected from the Gulf of Alaska continental margin (59° 33.35´N, 144° 09.35´W, 690 m water depth) (**Figure 1**). The piston core was split into the archive and working halves. The archive samples were used for foraminifer ^{14}C dating and planktonic foraminifer carbon– and Oxygen–isotope (δ^{13}C and δ^{18}O) analyses, and the working half samples were used for all other measurements. The core depth was defined by a composite core-depth below the seafloor (bsf), which was determined using correlations between Fe, Mn, and Ti downcore variabilities of cores CL14PC and CL14MC obtained in an ITRAX X-ray fluorescence (XRF) core scanner (Mondal et al. 2021) **(Figure C1)**. The total core length after integrating CL14PC and CL14MC was ~869 cm (bsf, centimeters below the seafloor scale).

To construct the ^{14}C-based age-depth model for core CL14PC/MC, *G. bulloides,* and *N. pachyderma* (s) tests from the > 125-µm size fraction in 1–4-cm-thick subsamples **(Table 5)** was used. Fourteen ^{14}C samples from fourteen sedimentary horizons from core CL14PC/MC (one sample was from core CL14MC) were prepared. As the upper part of the core did not contain sufficient foraminifer tests, additional tests were collected at the corresponding depths from the working half, pooled for the ^{14}C measurement **(Table 5)**. Among the fourteen samples, one was from a molluscan shell at a core depth of 451.9 cm, well-preserved and unfragmented. The foraminifer and shell samples were cleaned using the same protocol for δ^{18}O and δ^{13}C (Subsection 3.3.2). The ^{14}C measurements were performed using an accelerator mass spectrometer (AMS) at the Woods Hole Oceanography Institution (NOSAMS) **(Table 5).** Although one ^{14}C age from the lowest part of the core (868.5 cm) exhibited a slight age reversal (**Table 5** and **Figure 13**), all ^{14}C dates were used to construct an age-depth model. In addition to fourteen ^{14}C dates, an additional date of –67 (cal yr BP) at a 0-cm depth was also included to represent modern sedimentation. A Bayesian statistical age model using the {*rbacon*} R script package (Bacon) (version 2.3.9.1) (Blaauw & Christen, 2011) was constructed for age-depth model. Radiocarbon dates were calibrated using Marine13 (Reimer et al., 2013) with a constant regional reservoir correction (ΔR) of 470 ± 80 years (McNeely et al., 2006), similar to that of core EW0408-85JC in the GOA (Davies et al. 2011; Davies-Walczak et al. 2014). The Bacon model divides a core into many thin vertical sections using a Bayesian approach. Then, through millions of Markov Chain

Monte Carlo (MCMC) iterations, builds an age-depth model based on the accumulation rate for each of these sections (Blaauw & Christen, 2011).

Table 5. The accelerator mass spectrometry (AMS) ^{14}C dates from the core CL14PC/MC (KH17-3-CL14PC/MC).

Core	**Type**	**Core depth (cm, bsf)**	**Planktonic foraminifer ^{14}C age (years BP)**	**Planktonic foraminifer ^{14}C age error (± years BP)**	**Lab code**
CL14MC	Multiple	13.5	260[a]	60	OS-144767
CL14PC	Piston	88.0	1560	40	OS-144765
CL14PC	Piston	292.4	4240	65	OS-144766
CL14PC	Piston	451.9	6690[b]	25	OS-144531
CL14PC	Piston	521.7	8360	30	OS-139041
CL14PC	Piston	632.7	9570	40	OS-139042
CL14PC	Piston	705.1	10700	40	OS-139149
CL14PC	Piston	726.4	11050	45	OS-144532
CL14PC	Piston	741.2	12600	35	OS-139106
CL14PC	Piston	765.4	13500	50	OS-144533
CL14PC	Piston	783.7	14000	55	OS-144590
CL14PC	Piston	809.5	14650	55	OS-144591
CL14PC	Piston	845.7	15000	40	OS-139107
CL14PC	Piston	868.5	14750	60	OS-144592

[a] The data was not used to calibrated calendar age due to being out of range of calibration.

[b] Mollusca shells.

An ensemble of age-depth iterations calculated the mean, median, minimum, and maximum (2σ uncertainty). In this study, the mean age was used for the age-depth model (**Figure 13**). The age model for core EW0408-85JC has also been revised by the Bayesian statistic age model {*BChron*} (Haslett and Parnell 2008; Parnell et al. 2008) with the Marine13 calibration curve. The foraminifer $\delta^{18}O$ and $\delta^{13}C$ stable isotope records from core EW0408-85JC (85JC), which were used for comparison with data of this study, are based on this age model.

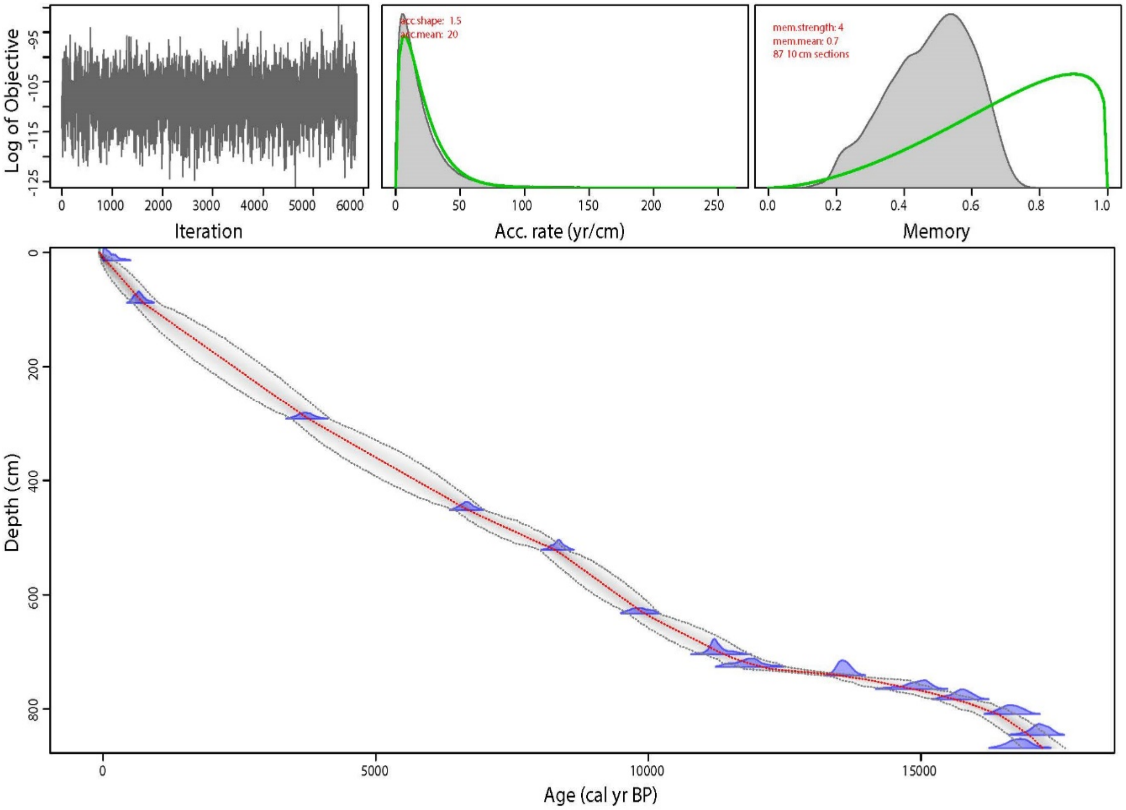

Figure 13. Radiocarbon (^{14}C) based age-depth model. The age (cal yr BP) versus depth (cm) model was constructed based on the radiocarbon (^{14}C) dates by the "rbacon" version 2.3.9.1 (Blaauw & Christen, 2011). The upper three small panels are depicted as "iteration," "accumulation rate (yr/cm)," and "memory." The prior (green line) and posterior (grey shade) accumulation rate consist of gamma distribution with two parameters and its "shape" and "means" set by acc.shape (here accumulation shape is 1.5) and acc.mean (here accumulation mean is 20), respectively. The green line in the memory means prior, and the grey shaded area represents the posterior distribution of the memory, and it is a beta

distribution. We used mem.strength (memory strength) 4 and memory mean (mem.mean) 0.7, and the thickness of each section is 10-cm, and the entire sections are 87. In the bottom panel, the transparent blue shape is the calibrated ^{14}C dates, and the grey shaded area shows the more likely calendar age; the grey stippled dot line is the 95% confidence intervals of the calendar ages. The red stippled dot line is the mean age for each of the depths.

Recently, radiocarbon calibration curves have been revised, and the IntCal20 and Marine20 calibration curves have been developed (Heaton et al. 2020; Reimer et al. 2020). Thus, we also reconstructed a Marine20-based age-depth model using the Bacon {*rbacon*} package (version 2.4.3) (Blaauw & Christen, 2011), handled similarly like Marine13 described above, and recalculated the regional reservoir correction (ΔR) of 301 ± 60 years (n = 10, (McNeely et al., 2006) near core site CL14PC. There are minimal age differences between the Marine13 and Marine20 calibrated ages at any given depth (**Table B1** in Appendix B **and Figure 14**), with a maximum of ~200 years at approximately 17.0 ka. Therefore, such age differences are considered minor, and our interpretation is insensitive; and in addition, other core data used in the study were based on the Marine13 calibration curve. Therefore, in this study, the Marine13-based age-depth model was used for core CL14PC/MC, and the alternative Marine20-based ages are included in the supplementary file (**Table B1** in Appendix B).

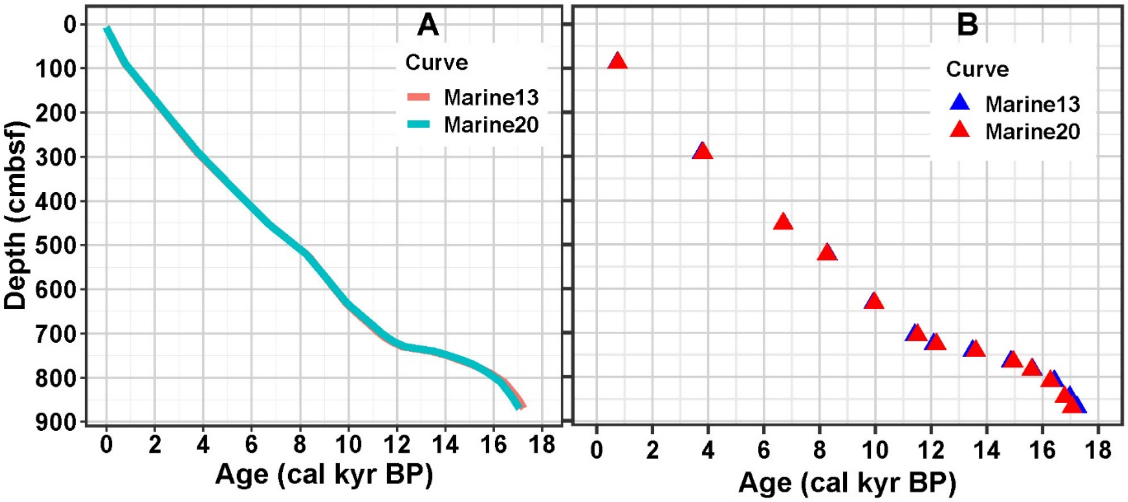

Figure 14. Comparison of age (cal kyr BP) from two calibration curves (Marine13 and Marine20). The age (cal kyr BP) from two calibration curves, Marine13 (Reimer et al., 2013) and Marine20 (Heaton et al. 2020; Reimer et al. 2020) (A, left side figure), and the age (cal kyr BP) calibrated from both Marine13

and Marine20 only for the 13 radiocarbons (^{14}C) dates (B, right side figure) are plotted versus depth (cmbsf (cm below sea-floor scale)). The packages used to reconstruct age-depth models are Bacon-2.3.9.1 and Bacon-2.4.3 (Blaauw & Christen, 2011) for Marine13 and Marine20, respectively, with R (rbacon). Comparison of age (cal kyr BP) between two calibration curves shows a similar pattern against depth (cmbsf), only a slide difference in ~17.0 kyr (ka) (maximum 192 years).

The age-depth model for core CL14PC/MC represents continuous sedimentation over the past ~17.2 ka. The sedimentation rates ranged from 8.3 to 100 cm/kyr, and relatively lower sedimentation rates were observed between 14.1 and 12.3 ka. The lowermost part of the core (764.1–869 cm) consisted of silt and clay with a high abundance of pebble-sized ice-rafted debris (IRD) overlain with a distinct lamina to the sub-lamina interval (736.3–764.1 cm) with sharp boundaries (**Figure 15**). The onset of the lamination was dated to be 14.8 ka (14.3–15.2 ka with a 95% confidence range), which is consistent with the well-dated nearby core EW0408-85JC (Davies et al., 2011). The onset of the lamination should correspond to the transition (14.642 ± 0.186 cal. kyr BP) from Heinrich Stadial 1 (HS1) to the B-A as assigned by the North Greenland Ice Core Project (NGRIP, Rasmussen et al. 2006). Another weakly sub-laminated interval was observed at 690.1–711.2 cm depth (**Figure 15**) with a bottom boundary dated at 11.57 ka (11.21–12.0 ka with a 95% confidence range). The timing of this seems to correspond to the YD–Preboreal transition (11.653 ± 0.099 cal. kyr BP) as assigned by the NGRIP (Rasmussen et al., 2006) and the onset of meltwater pulse 1B (MWP-1B, 11.45–11.1 cal ka BP) as assigned by Barbados coral record (Abdul et al., 2016), and nearby core EW0408-85JC (11.160 ± 0.13 ka) (Davies et al., 2011). The close similarity between the GOA and the NGRIP δ^{18}O records and the timing consistency between lamina formation in the GOA and rapid climate changes in the northern hemisphere confirm the validity of the age model for core CL14PC/MC. This study mainly focuses on the last deglaciation and only discusses the period from 9.0–17.2 ka.

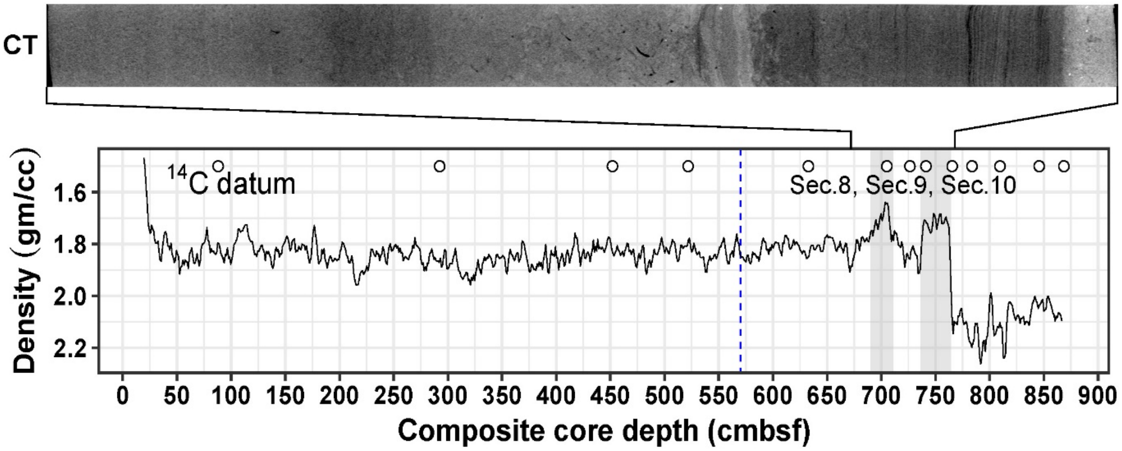

Figure 15. Computerized Tomographic scan (CT-scan) image and density (gm/cc) plot. The upper image shows the CT scan, and the lower figure shows the density (gm/cc, 3-point running mean values in reverse order, black-line) plotted versus composite core depth (cmbsf). The CT-scan image is only for section 9. The ^{14}C datum (white fill black circle) is depicted in the upper part of the density (gm/cc) plot. The vertical gray shaded areas indicating two laminations at 736.3–764.1 cmbsf, and 690.1–711.2 cmbsf. The vertical dashed line (blue dash line) at 570 cmbsf indicating the starting of the downcore deglacial section (Sec.8, 9, and 10) that is considered for focusing (570–869 cmbsf) on this study.

3.3.2. Foraminifer stable isotope measurements

For planktonic foraminifer δ^{13}C and δ^{18}O measurements, bulk sediments (1-cm thick sections) were passed through a 63-µm sieve, and the > 63-µm size fraction was then dried in an oven at 50 °C for 24 h. *G. bulloides* (~20 specimens) and *N. pachyderma* (s) (~20 specimens) were then collected from the 180–250-µm size fraction to minimize size-dependent effects on isotopic compositions (Hillaire-Marcel et al., 2004). The broken foraminifer tests nor those with yellowish or blackish discoloration were not used in this study. The foraminifer samples were crushed, ultrasonically cleaned with ultrapure water (18.2 MΩ·cm), and methanol (super special grade, Wako Pure Chemical Industries, Ltd., Osaka, Japan) three times, and rinsed with ultrapure water three times to remove any adhering clays on the tests. Using ~50–100 µg cleaned foraminifer tests, we measured carbon and oxygen stable isotopes using a Thermo-Finnigan MAT-253 isotope ratio mass spectrometer (IR-MS) with a carbonate preparation device at the CMCR, Kochi University, Japan. Data were reported in δ notation (‰ VPDB) corrected using the NBS-19 standard measured each day. Here, a total of 104 δ^{13}C and 104

δ^{18}O data for both species from 9.0 to 17.1 ka were reported (**Table B2** in Appendix B). The planktonic foraminifer stable isotopes (δ^{13}C and δ^{18}O) noted here (total 104) were all measured from a 1-cm thick subsample; therefore, the data will be high-resolution records.

3.3.3. ITRAX multi-element count

The ITRAX XRF core scanner measurement was conducted at the CMCR, Kochi University, the detailed procedure described in chapter 2. Here, use only the Fe, Mn, and Ti element count (cps) to determine the composite core-depth below the seafloor (bsf)-scale (**Figure C1** in Appendix C).

3.3.4. Analysis of the abundance of ice-rafted debris (IRD)

Core Section 10 (769–869 cm, ~15–17.2 ka), which corresponds to HS1, is marked by a higher abundance of IRD, and at least three concentrated IRD layers could be visually identified in the upper part of this section **(Figure 16)**.

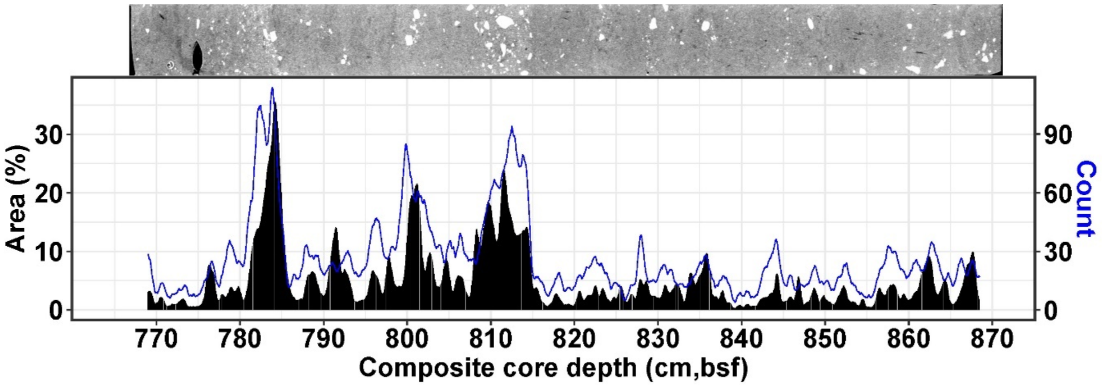

Figure 16. The abundance of ice-rafted debris (IRD) in the core CL14PC. The upper image is the CT-scan image of section 10 in the core CL14PC showing the IRD in white color. In the lower part, the IRD (Area (%, black fill shade of 11-point running mean) and count blue line of the 11-point running mean) are plotted versus composite core depth (cm, bsf) of the core CL14PC.

To quantitatively reconstruct temporal changes in the abundance of IRD, we used high-resolution whole-core CT images taken at 0.5-mm intervals. First, we converted the CT images to 8-bit images, and then black and white images were made with threshold values of 200 and 255. Next, both the number and the area occupied by grains larger than 2 mm (i.e., higher density area) in a selected area (i.e., 5.6 cm × 5.6 cm) within the core (diameter = 80 mm) were calculated using the ‘analyze particles’ tool in ImageJ software. This process was automated for a total of 1,974 CT images.

3.3.5. Measurement of alkenone biomarkers

Total lipids were extracted three times from 1 to 3.5 g of dried sediments with dichloromethane/methanol (95:5) using a SpeedExtractor (E-916, BUCHI) at 100 °C and 1,450 p.s.i. for 5 min. The pooled extracts were separated into three fractions using silica gel column chromatography; aliphatic and aromatic hydrocarbons, aliphatic ketones (alkenones), and alcohol plus fatty acid fractions were isolated. The C_{37} alkenones were analyzed with an HP6890 gas chromatograph (GC) equipped with an on-column injector-fused silica capillary column (CPSIL-5 CB, 60 m length × 0.25 mm inner diameter, and a film thickness of 0.12 mm) and a flame ionization detector. The GC oven temperature was programmed to increase from 50 to 290 °C at a rate of 20 °C min^{-1}, and then from 290 to 310 °C at 0.5 °C min^{-1}. The alkenone measurements were conducted at the Institute of Low-Temperature Science, Hokkaido University, Japan (Seki et al., 2004; Horikawa et al., 2015). The relative abundance of the tetra-unsaturated C_{37} alkenones to total C_{37} alkenones (% $C_{37:4}$) was defined as $\% \, C_{37:4} = [C_{37:4}]/([C_{37:2}] + [C_{37:3}] + [C_{37:4}]) \times 100$.

3.3.6. Sr-Nd isotope measurements

For Sr and Nd isotope determinations of the bulk sediments, a sample from sequential leaching (Horikawa et al., 2011; Kozaka et al., 2018) and acid digestion (Appendix A.2.3.) was used. Sr isotopic compositions were analyzed on a high-resolution multi-collector inductively coupled plasma mass spectrometer (MC-ICP-MS) NEPTUNE (Thermo Fisher Scientific) at the Research Institute for Humanity and Nature (RIHN), Kyoto, Japan. Sr isotope ratios ($^{87}Sr/^{86}Sr$) were normalized to 0.710250 for the NBS 987 standard, which averaged 0.710277 ± 0.00004 (2σ, $n = 17$) at the time of analysis. A total of 42 Sr isotope ratios ($^{87}Sr/^{86}Sr$) data were reported in this study from 9.0 to 17.2 ka (**Table B3** in Appendix B). The Nd isotopes were measured with a thermal ionization mass spectrometer (TIMS) TRITON at Kochi Institute for Core Sample Research, JAMSTEC, Japan. An international standard JNdi-1

(Tanaka et al., 2000) was also analyzed, and the average value (0.512095, *n* = 3) was compared with the recommended value of JNdi-1 (0.512115; Tanaka et al., 2000) to determine a correction factor for each of the samples analyzed each day. The Nd isotopes were reported as ε_{Nd} (**Table B4** in Appendix B), which is $[(^{143}Nd/^{144}Nd)_{sample}/(^{143}Nd/^{144}Nd)_{CHUR} - 1] \times 10^4$, where the Chondritic Uniform Reservoir (CHUR) is 0.512638 (Jacobsen & Wasserburg, 1980).

3.4. Results

3.4.1. Planktonic foraminifer stable isotope records

The $\delta^{18}O$ values of *N. pachyderma* (s) and *G. bulloides* showed very similar evolution, ranging from 3.70‰ to 1.27‰ and from 3.75‰ to 1.50‰ between 9.0 and 17.1 ka, respectively, and their values simultaneously decrease from ~16.0 ka (**Table B2** in Appendix B**, Figure 17**). At the formation of the laminae of the B-A, the $\delta^{18}O$ values for *N. pachyderma* (s) sharply decreased in 0.56‰. At the same time, *G. bulloides* represented more gradual decreases in $\delta^{18}O$ values from the late HS1 to laminated B-A periods (**Figure 17**). The $\delta^{18}O$ values for both species simultaneously decreased during the late YD from 12 ka to 10.5 ka (**Figure 17**).

The deglacial $\delta^{18}O$ records from two subsurface-dwelling planktonic foraminifera species clearly showed that the early B-A (13.8–14.8 ka) is marked by distinctly lighter mean $\delta^{18}O$ values compared to those of the late B-A (13.0–13.8 ka); 2.18 ± 0.26‰ (early B-A, *N. pachyderma* (s)), 2.12 ± 0.28‰ (early B-A, *G. bulloides*), 2.49 ± 0.14‰ (late B-A, *N. pachyderma* (s)), and 2.35 ± 0.11‰ (late B-A, *G. bulloides*). During such an early B-A period, high-resolution planktonic foraminifer $\delta^{18}O$ records revealed three $\delta^{18}O$-depletion peaks at 14.6–14.3 ka, 14.2–14.1 ka, and 13.9–13.8 ka, which are more distinct in *N. pachyderma* (s) $\delta^{18}O$ records. Similar multiple $\delta^{18}O$-depletion peaks at the early B-A are already documented in core EW0408-85JC (Davies et al., 2011). Thus, our data confirm that lowering planktonic foraminifer $\delta^{18}O$ is not due to analytical artifact (**Figure 17**). Furthermore, as another feature found in both $\delta^{18}O$ records, *N. pachyderma* (s) tended to have relatively lighter $\delta^{18}O$ values than *G. bulloides* during the early B-A and at ~11.3 ka (**Figure 17**).

The $\delta^{13}C$ values of *N. pachyderma* (s) and *G. bulloides* also showed very similar overall trends with a consistent offset, with a relatively higher value of 0.5‰ for *N. pachyderma* (s) during the period 9.0–17.0 ka (**Figure 17**). Both species showed remarkably lighter $\delta^{13}C$ values during the early B-A and heavier $\delta^{13}C$ values throughout the late YD.

The foraminifer isotope data in this study matched well with previously published foraminifer isotope records from core EW0404-85JC (Davies et al., 2011) for $\delta^{18}O$ but showed slight differences for $\delta^{13}C$. For example, at ~12 ka, core EW0404-85JC exhibited distinct lighter $\delta^{13}C$ values for both species, which were not found in this study (**Figure 17**). Importantly, Davies et al. (2011) is based on their measurements for the > 150-µm size fraction, whereas we measured a 180–250-µm size fraction. As foraminifer $\delta^{13}C$ and $\delta^{18}O$ values have a size-dependent effect (i.e., smaller foraminifer tests yield lighter isotopes) (Hillaire-Marcel et al., 2004), this might explain the slight discrepancy in $\delta^{13}C$ values between two nearby sites. In addition, factors that influence foraminifer $\delta^{13}C$, such as 'vital effects,' seasonal shifts of environmental conditions, and dissolution of shell walls thickness, are prominent in small-sized shells (Ravelo & Hillaire-Marcel, 2007).

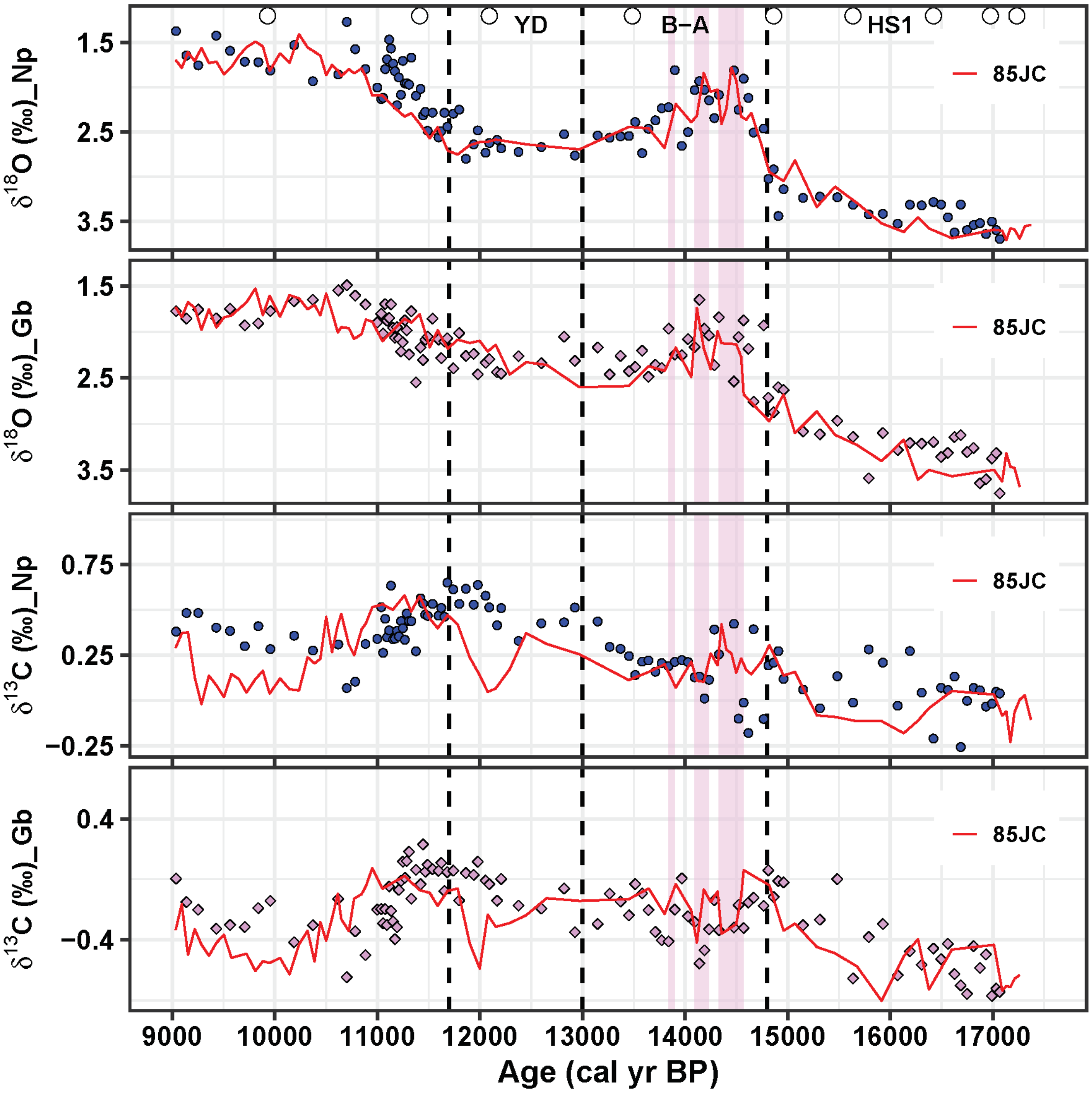

Figure 17. Planktonic foraminifer oxygen and carbon stable isotope records during the last deglacial period. The foraminifer $\delta^{18}O$ (‰) and $\delta^{13}C$ (‰) of Gb (*G. bulloides*) and Np (*N. pachyderma* (s)) are plotted versus calibrated age (cal yr BP) mainly focus between 9 to 17.2 ka (cal kyr BP). The blue fill black circle indicated Np, and the plum color fill diamond shape indicated Gp (this study). In contrast, the planktonic foraminifer (Np & Gb) records ($\delta^{18}O$ (‰) & $\delta^{13}C$ (‰)) in the core EW0408-85JC (85JC, Davies et al., 2011) mentioned by a red line. The ^{14}C datum (white fill black circle) is mentioned in the upper part of the plot. The three vertical areas (peak $\delta^{18}O$-depletion) at 14.6–14.3 ka, 14.2–14.1 ka, and 13.8–13.9 ka are shaded by plum color. At the top of the plot, the timing of major climate intervals during the last deglaciation was demarked by HS1, B-A, and YD.

3.4.2. IRD abundance during HS1

In this study, higher density areas larger than 2 mm are defined as IRD. The temporal changes in the number and area occupied by IRD grains (> 2 mm) revealed three prominent IRD-concentrated layers from 16.5 ka to 15.5 ka of the late HS1 (**Figures 18**). The number and area data were consistent (**Figure 16**, $R^2 = 0.71$, $p < 0.001$). It was also consistent with the IRD abundance observed in the CT images, indicating that the image-analyzed data can be used as the representative of the abundance of IRD deposition. From these high-resolution IRD data, we found that the oldest massive IRD layer for the past ~17 ka reaches a maximum at ~16.5–16.4, and then largely diminished after ~16.4 ka (**Figures 16, 18**). The following massive IRD deposition was found at ~16.2 ka. The third and most enormous period of IRD deposition begins at ~15.7 ka. It reaches a maximum at ~15.6 ka, followed by a notable reduction of massive IRD deposition from 15.5 ka and the formation of the laminated sediments at B-A (**Figures 16, 18**).

3.4.3. Relative abundance of tetraunsaturated C_{37} alkenones (%$C_{37:4}$)

The relative abundance of %$C_{37:4}$ ranged from 2 to 44% during the period 9.6–16.6 ka, and we detected seven distinctly higher values (> ~18%) (**Figure 18**). Four of the peaks are single-peak, and the rest three peaks seem to be long-lasted. The earliest three peaks at ~16.4 (18%), ~16.2 (39%), and ~15.6 (42%) ka during HS1 are concomitant with the layers of massive IRD deposition (**Figure 18**). The fourth %$C_{37:4}$ alkenones peak at the end of HS1 does not accompany distinct IRD deposition, and %$C_{37:4}$ alkenones gradually decreased with time. During the early B-A, anomalously high values (24% and 29%) were again found at ~14.1 and

~13.9 ka, respectively, which are concomitant with δ^{18}O-depletion of both planktonic foraminifera at 14.2–14.1 and 13.8–13.9 ka (**Figures 17, 18**). Furthermore, we also found the higher and most prolonged %$C_{37:4}$ alkenones peak (37%) at ~12.2 ka (11.7–12.8 ka with a 95% confidence range) during the middle YD. Following the YD, the %$C_{37:4}$ alkenones decreased by less than 10% to be close to the average value during the Holocene (~8%, *n* = 12).

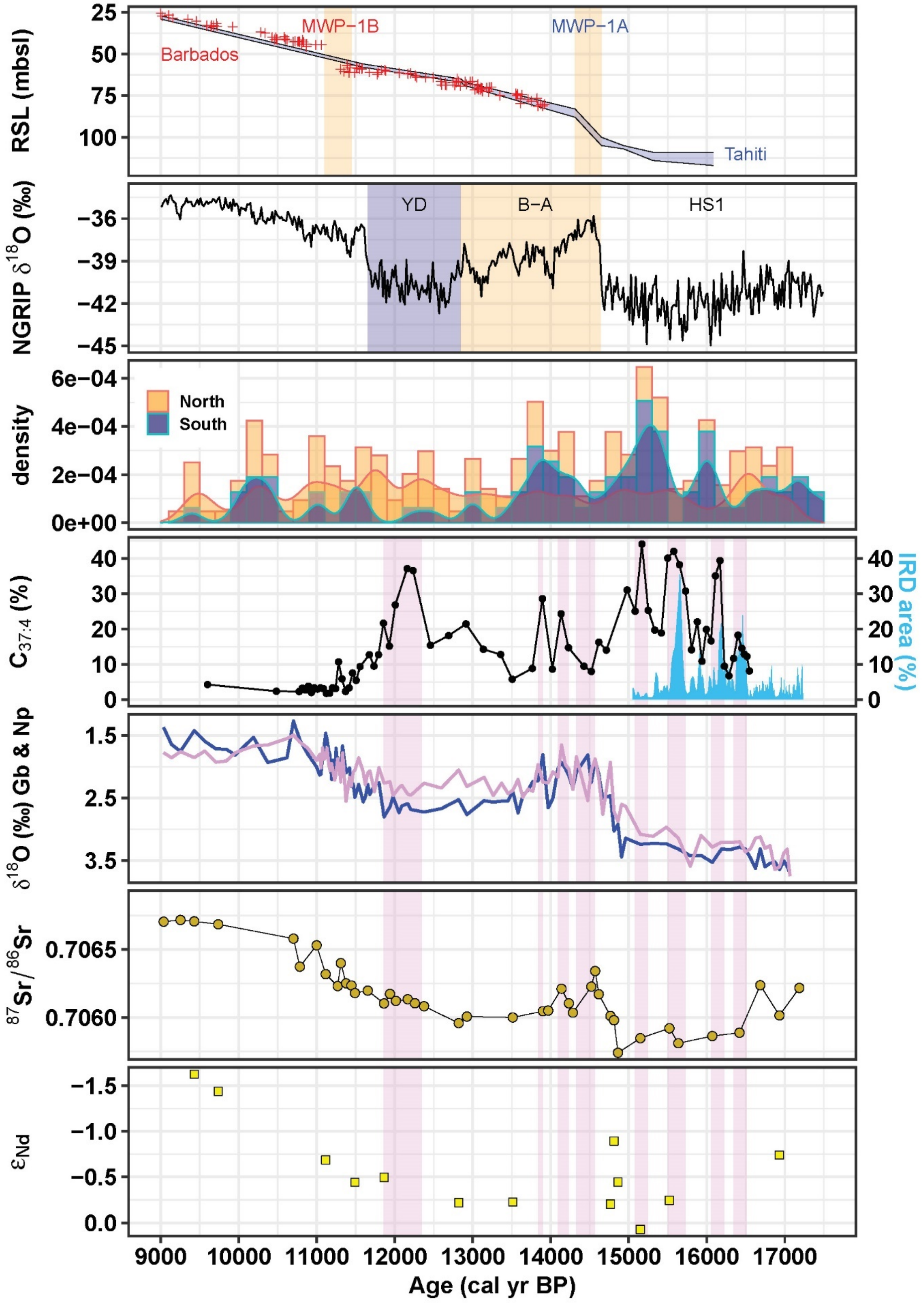

Figure 18. Alkenone proxy-based meltwater variability with related multi-proxy records during the last deglacial periods. The RSL (relative sea level, mbsl-meter below sea level) of Tahiti (black-line bound

with blue fill, (Deschamps et al., 2012)) and Barbados (red plus shape, (Abdul et al., 2016)), the NGRIP (Rasmussen et al., 2006) $\delta^{18}O$ (‰, black line), the density of cosmogenic ^{10}Be exposure dating histogram with density plot in the y-axis (bar graphs with a curve) of Northern part (Young et al. 2009; Stroeven et al. 2010, 2014; Menounos et al. 2017; Lesnek et al. 2018) of CIS (orange color) and Southern part (Margold et al. 2014; Balbas et al. 2017; Menounos et al. 2017; Darvill et al. 2018) of CIS (dark blue color), IRD area (%, deep sky blue fill shade) and alkenones $C_{37:4}$ (%) (black-line with black fill markers), $\delta^{18}O$ (‰) of planktonic foraminifer (Gb- plum color thick line and Np- blue color thick line), and the $^{87}Sr/^{86}Sr$ ratios (gold3 color fill black circle) and ε_{Nd} (yellow fill black square) are plotted versus age (cal yr BP) in the y- and x-axis, respectively. The MWP-1B (Abdul et al., 2016) and MWP-1A (Deschamps et al., 2012) at 11.10–11.45 ka and 14.31–14.65 ka, respectively is marked by orange color at the top of the plot. The B-A, YD, and HS1 in the NGRIP plot marked by orange, blue, and without color, respectively. The timing of multiple melting intervals mentions at 16.3–16.5, 16.1–16.2, 15.5–15.7, 15.1–15.3, 14.3–14.6, 14.1–14.2, 13.8–13.9, and 11.9–12.4 ka by a vertical plum color shading.

3.4.4. Sr-Nd isotopes of the detrital fraction

The $^{87}Sr/^{86}Sr$ isotopic composition ranged from 0.705740 to 0.706718 during 9.0–17.2 ka, while ε_{Nd} data ranged from –1.62 to 0.1 ε_{Nd}. The overall ranges of the variations in $^{87}Sr/^{86}Sr$ isotopic compositions and ε_{Nd} values were minimal, but the temporal changes in the detrital Sr-Nd isotopes showed a similar trend to the foraminifer $\delta^{18}O$ records. In the late HS1, the $^{87}Sr/^{86}Sr$ isotopic ratio slightly decreases, and after 15.6 ka, the value first increases then decreases up to the onset of B-A (~14.8 ka). Similarly, after 15.5 ka, the ε_{Nd} composition first increases, then a sharp decrease up to the beginning of B-A (~14.8 ka). At the onset of the B-A, both Sr-Nd isotopic composition increase toward radiogenic (**Figure 18**). Although the sampling resolution was not sufficiently high, both detrital Sr and Nd isotopes were characterized by intermediate values in the early HS1 and the B-A–YD (**Figure 18**).

3.5. Discussion

3.5.1. Meltwater Events in the Northern Gulf of Alaska

3.5.1.1. Heinrich Stadial 1

The $\%C_{37:4}$ alkenones are recognized as salinity and/or temperature (Sicre et al. 2002) proxies, with higher percentages reflecting cool and/or freshwater masses (Rosell-Melé 1998; Rosell-Melé et al. 2002; Sicre et al. 2002; Harada et al. 2003; Bendle et al. 2005; Seki et al.

2005; Sachs et al. 2013). In the modern Bering Sea, Harada et al. (2003) found a significant negative correlation between $\%C_{37:4}$ alkenones (18.3–41.4%) and salinity (32.4–30.4) ($\%C_{37:4} = 397.6–11.7 \times salinity$, $r = 0.76$, $n = 8$). They interpreted that temperature does not have a primary influence on the $\%C_{37:4}$ alkenones production mechanism. Further, the $\%C_{37:4}$ alkenones data, obtained from Pliocene–Pleistocene Bering Sea sediments, are also used as a salinity proxy, and from temporal variations in $\%C_{37:4}$ alkenones, glacial meltwater inputs related to the formation of the Alaskan mountain glaciers have been established (Horikawa et al., 2015).

In the North Atlantic, Rosell-Melé (1998) proposed that $\%C_{37:4}$ alkenones (> 5%) in sediment are not correlated with temperature. Further, Rosell-Melé et al. (2002) mentioned that higher values of $\%C_{37:4}$ alkenones indicate low sea-surface salinity due to melting of icebergs and/or sea-ice melted freshwater in the North Atlantic, and interpreted that Heinrich events marked by high $\%C_{37:4}$ alkenones with IRD accumulation as reflecting low salinity due to iceberg flotillas. In the GOA, we found, for the first time, anomalously high peaks in $\%C_{37:4}$ alkenones at ~16.4 (18 %), ~16.2 (39 %), and ~15.6 (42 %) ka (**Figure 18**). Notably, these high peaks in $\%C_{37:4}$ alkenones coincide with prominent IRD deposition, which occurred at ~16.5 ka, followed by ~16.2 ka and ~15.6 ka (**Figure 18**). Because IRD deposition results from the melting of icebergs, the coincident high peaks in $\%C_{37:4}$ alkenones can be interpreted as a result of low salinity related to the melting of icebergs.

Interestingly, diatom-derived $\delta^{18}O$ records from the offshore site in the GOA (core SO202-27-6, 54.3°N, 149.6°W; 2,919 m water depth) also represented distinct surface freshening signal at HS1 (~16.9–15.6 ka and mean salinity 29.9) (Maier et al., 2018). However, such multiple pulses of surface freshening that were detected in the HS1 have not been documented in the planktonic foraminifer $\delta^{18}O$ records in our core (CL14PC) nor other cores (Davies et al. 2011) in the northern GOA (**Figures 17, 18**). There are several potential reasons for this inconsistency. First, lower SSS and lower SST during HS1 might have canceled out their opposite influences on foraminifer $\delta^{18}O$. Second, the environmental preferences of planktonic foraminifera make it unlikely that they would have inhabited a meltwater plume. That is, *G. bulloides* and *N. pachyderma* (s) might have dwelled in the subsurface layer, avoiding surface freshening. Third, if the meltwaters originated from the coastal glaciers close to a maritime moisture source, relatively heavier $\delta^{18}O_{ice}$ causes a meltwater signal that is difficult to detect.

For meltwater injection during HS1, general circulation models (GCMs) demonstrate that a collapse of the Atlantic Meridional Overturning Circulation (AMOC) as Heinrich Stadial 1 induces reduced precipitation and warming in the eastern equatorial Pacific (EEP), followed by intensification of the Aleutian Low (Okumura et al., 2009). Intensified Aleutian Low leads to stronger Westerlies, accelerating advection of warm, salty surface waters from the subtropical Pacific into the northeast Pacific (Maier et al., 2018). It is likely that advection of warm subtropical waters, as well as deglacial sea-level rise, would have destabilized the marine-based western margin of the CIS and then promoted retreat of the grounding line of them during HS1 (Cosma and Hendy 2008; Misarti et al. 2012; Praetorius and Mix 2014; Taylor et al. 2014; Lesnek et al. 2018). Thus, meltwater injection during HS1 would have resulted from collapses of the marine-based western margin of the CIS, and a suite of substantial iceberg discharges from CIS would have created distinct low salinity conditions over the coastal and central GOA (**Figure 11, 18**).

3.5.1.2. Bølling-Allerød

During the early B-A, one can expect that northern GOA might have received a sufficient volume of meltwater from the CIS because the rapidly increasing temperature of 3–5 °C (Taylor et al. 2014; Praetorius et al. 2015) from HS1 to the early B-A would have risen glacial equilibrium-line altitudes and melted the CIS. However, the previously published $\delta^{18}O_{sw}$ records calculated from a paired analysis of alkenone ($U^{k'}_{37}$) SST and *G. bulloides* $\delta^{18}O$ from the GOA cores (EW0408-85JC, -26JC, -87JC) do not show distinctly lower salinity signals during early B-A; conversely, $\delta^{18}O_{sw}$ indicates saline conditions (Praetorius et al., 2020) (**Figure 11**). Saline conditions are also documented during the early B-A at ~13.8 ka from core MD02-2496 off Vancouver (Taylor et al., 2014). The $\delta^{18}O_{sw}$ estimation assumes that both alkenone-producing haptophytes and *G. bulloides* reflect a water mass in the same season and at the same depth. However, such an assumption cannot be confirmed from sedimentary records. Thus, their salinity reconstruction is debatable and requires other salinity reconstructions not based on their assumption (i.e., different salinity proxies).

In this study, we found, for the first time, anomalously high values of %$C_{37:4}$ alkenones (24% and 29%) at ~14.1 and ~13.9 ka during the early B-A. SST cannot explain these unusually high %$C_{37:4}$ alkenones values because SST was high during the B-A period. Therefore, high values of %$C_{37:4}$ alkenones can be interpreted to reflect low salinity surface conditions (**Figure**

18). Notably, these peaks of %$C_{37:4}$ alkenones are also concomitant with prominent δ^{18}O-depletion in the planktonic foraminifer records at 14.2–14.1 ka and 13.9–13.8 ka. Generally, relative to the LIS, a CIS meltwater signal is difficult to detect from planktonic foraminifer δ^{18}O because LIS $\delta^{18}O_{ice}$ was probably in the order of –25 to –35 ‰ (Flower et al., 2004) while meteoric water in south-central Alaska has δ^{18}O values of –15.3 ± 2.8 ‰ (1σ), which are closer to the seawater value (~0 ‰) (Gonyo et al., 2012). In these circumstances, the observed co-occurrence of higher %$C_{37:4}$ alkenones and δ^{18}O-depletion has very important implications for volumetrically significant meltwater injection at multiple times during the early B-A (**Figure 18**), unlike previous interpretation (Praetorius et al., 2020) (**Figure 18**). The inferred meltwater greatly influences density and increases the offshore pressure and density gradients, thus poleward transport the warmer water and further increasing glacial melting (Royer & Finney, 2020).

We believe co-occurrence of higher %$C_{37:4}$ alkenones and δ^{18}O-depletion during the early B-A indicate robust evidence for low-salinity surface conditions related to glacial meltwater, but we should also emphasize that the δ^{18}O-depletion of both *G. bulloides* and *N. pachyderma* (s) did not accompany a corresponding increase in %$C_{37:4}$ alkenones at 14.6–14.3 ka (**Figure 18**). At 14.6–14.3 ka, the δ^{13}C record of *G. bulloides* shows distinctly lower values as same as meltwater events inferred from higher %$C_{37:4}$ alkenones at ~14.1 and ~13.9 ka (**Figure 17**). The $\delta^{13}C_{DIC}$ (DIC, dissolved inorganic carbon) record from Kepler Lake in southern Alaska shows depleted values of –9.5 to –9‰ (Gonyo et al., 2012). If collapses of the CIS supplied glacial meltwater, which has depleted $\delta^{13}C_{DIC}$, into the coast in the GOA, the $\delta^{13}C_{DIC}$ in the sea surface water were decreased, and the planktonic foraminifer δ^{13}C were also lowered. Therefore, although the planktonic foraminifer (*G. bulloides* and *N. pachyderma* (s)) δ^{18}O-depletion at 14.6–14.3 ka lacks a corresponding increase in %$C_{37:4}$ alkenones, the depleted δ^{13}C and δ^{18}O signals strongly suggest that meltwater was also injected in the northern GOA at 14.6–14.3 ka. The lack of relationship between δ^{18}O-depletion of planktonic foraminifer and decreases in %$C_{37:4}$ alkenones at 14.6–14.3 ka might be related to differences in the seasons and depths of alkenone-producing haptophytes and *G. bulloides*: If meltwater inputs, that peaks from October to November at present-day (Stabeno et al. 2004), were not be high enough to sustain lower salinity condition throughout the year, especially in summer when alkenone-producing haptophyte algae bloom, lack of increase in %$C_{37:4}$ alkenones will happen. In Winter (February), the GOA received minimum runoff (Stabeno et al. 2004); during the period, the minimum meltwater did not reach the haptophyte's growth depth. In the early spring

(March/April), the meltwater runoff started increasing (Stabeno et al. 2004) and reached the planktonic foraminifer growth depth (0–50 m, Taylor et al., 2018). So, in early spring, the heavy growth of planktonic foraminifer received meltwater. In Summer (July), Prahl et al. (2005) found maximum alkenone export originate above Chlorophyll maximum layer in the North Pacific subtropical gyre. In this study (CL14PC) in summer (July), we found the maximum Chlorophyll concentration in 30 m (**Figure 12**). During the period (summer) when haptophyte was heavily produced, the meltwater in the shallower growth depth was quickly mixed with seawater. The mixing of seawater with meltwater was increased the surface water salinity, also induced by abrupt sea-level rise (Deschamps et al., 2012) and summer temperature (Praetorius et al., 2015). So, the haptophyte did not received prolong low saline meltwater and thus suppressed $C_{37:4}$ alkenone production (Harada et al., 2003). Therefore, in this study, we did not find the elevated %$C_{37:4}$ at the early B-A (14.6–14.3 ka).

In this study, the consistent records of %$C_{37:4}$ alkenones and δ^{18}O-depletion of planktonic foraminifer in the northern GOA support that the warmer B-A climate conditions during 14.6–13.8 ka (800 years) caused one minor and subsequent two volumetrically significant meltwater injection into the northern GOA. The ice sheet model studies imply that the deglacial warming halved the maximum volume of the CIS less than 500 years during the early B-A warm period (14.5–14.0 ka), causing a sea-level rise of 2.5–3.0 m (Peltier et al. 2015; Lambeck et al. 2017; Menounos et al. 2017) in the GOA. Our proxy data suggestive of meltwater injection into the GOA in the early B-A of 800 years (14.6–13.8 ka) were longer than the meltwater period in the ice sheet model studies. Furthermore, this 800-year-long meltwater injection period is more extended than MWP-1A that (MWP-1A) caused rapid sea-level rise (12–22 m) during 14.31–14.65 cal ka BP (Deschamps et al., 2012). Multiple CIS meltwater injections were temporally disaggregated during 14.6–13.8 ka, suggesting that the contribution of CIS melt to global sea-level rise during MWP-1A was minor. The glacio-isostatic adjustment (Peltier et al. 2015; Lambeck et al. 2017) and ice sheet model (Menounos et al. 2017) studies indicating that the CIS meltwater contribution to abrupt global sea-level rise (MWP-1A) was 17.5–21%. Other studies (Lambeck et al. 2014; Royer & Finney, 2020) mentioned that the contribution was ~10%. However, CIS's contribution to the freshwater budget on the northeastern Pacific during the abrupt global sea-level rise (14.6–14.3) was relatively small.

3.5.1.3. Younger Dryas

The %$C_{37:4}$ alkenones gradually increased from the end of B-A. Further, it reached a more prominent and persistent peak (37%) at ~12.2 ka (**Figure 18**), which represents a similar $\delta^{18}O_{sw}$ variation suggestive of low salinity conditions at the middle YD (Praetorius et al., 2020). Because the SST in the GOA described a 3–4 °C cooling into the YD (Praetorius et al. 2015, 2020), the significant SST cooling would have attributed to the production of $C_{37:4}$ alkenones. Although it is difficult to quantitatively define lower salinity to the high %$C_{37:4}$ alkenones, the fact that %$C_{37:4}$ alkenones peak at the middle YD is consistent with the lower $\delta^{18}O_{sw}$ values in the GOA (Praetorius et al., 2020) implies that low salinity surface conditions also favored the production of $C_{37:4}$ alkenones at YD. We argue that the melting of proximal ice induced the high %$C_{37:4}$ alkenones in the core CL14PC during summer, when alkenone-producing haptophyte algae bloom, as claimed in the off southeastern Norway core HM79-6/4 (Rosell-Melé (1998).

Indeed, in the YD at ~12.8 ka in the nearby core U1419, Walczak et al. (2020) mentioned high fluxes of meltwater associated with the retreat of the terrestrial ice (Briner and Kaufman 2008; Walczak et al. 2020). Moreover, freshwater, sea-ice, and sea-ice-related diatoms were abundantly observed at coastal GOA sites (55°N–58°N, EW0408-66JC, -11JC) during the YD (Barron et al., 2009) (**Figure 11**). In contrast, there is no clear evidence of a surface freshening signal at the offshore site in the GOA (core SO202-27-6) (Maier et al., 2018) (**Figure 11**). These lines of evidence suggest that the stadial YD period exhibited boundary conditions that supplied a considerable amount of meltwater into the GOA. But, unlike HS1 meltwater injection, the influence of meltwater injection at YD was restricted in coastal GOA. The restriction of low-saline influence in the northeast coastal Pacific might be related to the change in the paths of the Aleutian Stream; the low-saline Alaskan Stream re-inflowed into the Bering Sea during YD due to the re-opening of Aleutian passes.

3.5.1.4. Preboreal–Younger Dryas transition

After the YD, a less bioturbated and weakly sub-laminated interval occurs at 11.6 ka (**Figures 17, 18**). This event was coeval with deglacial MWP-1B as defined from Barbados records (Abdul et al., 2016) and the records from the core EW0408-85JC (Davies et al., 2011) within the uncertainty of our age model. Although sea-level rise (MWP-1B) following the termination of the YD is interpreted to be attributed to the melting of Northern Hemisphere Ice

Sheets (Abdul et al., 2016), our %$C_{37:4}$ alkenone data do not indicate lowered SSS, nor do the foraminifer isotope data. Together, this evidence suggests that meltwater injection into the northern GOA was less significant/ceased after the YD.

3.5.2. Sediment Provenance during the last deglacial transition

To associate meltwater injection found in our sediment records with the potential melting areas of CIS, we analyzed the Sr and Nd isotopes of bulk sediments. In general, marine sediments are mixtures derived from multiple sources, with each source having unique isotopic properties. Thus, the Sr-Nd isotopic compositions of the bulk sediments reflect mixing among all contributing sources. Furthermore, Sr and Nd isotopic compositions in CL14PC tightly co-varied throughout the core (**Figure 18**), suggesting that grain-size changes and/or incongruent weathering that affects only Sr isotopic compositions should be less important (Snoeckx et al. 1999; Clinger et al. 2016). Therefore, in our case, the Sr-Nd isotopic compositions can be simply interpreted as reflecting changes in sediment provenance.

In the late HS1 between ~16.5 ka–14.8 ka, both the $^{87}Sr/^{86}Sr$ isotopic composition and ε_{Nd} values of bulk sediments showed relatively lower values, an average of 0.70586 and −0.38, respectively (**Figure 18**). During the B-A, bulk sediments $^{87}Sr/^{86}Sr$ isotopic composition slightly shifted toward radiogenic values in the inferred meltwater-injection periods. However, the variation did not exceed Holocene $^{87}Sr/^{86}Sr$ ratios (**Figure 18**). The less significant changes in $^{87}Sr/^{86}Sr$ ratios mean that even if a large amount of meltwater was injected into the GOA, detrital sources did not significantly change, as in HS1. Davies et al. (2011) found an abrupt 1‰ decrease in benthic foraminifer $\delta^{18}O$ at ~14.2 ka. They interpreted this as evidence of meltwater's hyperpycnal flow in the northern GOA at intermediate water depths (~680 m). This evidence is indicative of the melt of the remnant of CIS near the core site. Similarly, ε_{Nd} values also shift toward radiogenic values to the B-A period. During the YD, the insignificant changes in $^{87}Sr/^{86}Sr$ ratios of the bulk sediments indicate insignificant changes in detrital sources throughout HS1 to the middle YD (**Figure 18**). The ε_{Nd} values also exhibited minor changes from B-A to YD. According to this geochemical evidence, we suggest that the YD freshening event was restricted to the coastal margins in the northern part of the GOA. And, the meltwater sources during the middle YD were the northern GOA proximal to the core-site. It has been argued that lower salinity during the YD in the coastal GOA was attributed to mega-floods from the Columbia River (Praetorius et al., 2020). However, the Ce record, which is indicative of Paleozoic–Proterozoic sediments supplied from the interior of North America, does not show any significant increase off Vancouver Island during the YD (MD02-2496, **Figure 11**) (Gombiner et al., 2016), suggesting an absence of mega-floods from the Columbia River during the YD. The compilation of cosmogenic ^{10}Be exposure dates in the northern part (> 55°N) of the CIS exhibits a broad concentration around the middle YD (Young et al. 2009; Stroeven et al. 2010, 2014; Menounos et al. 2017; Lesnek et al. 2018) (**Figure 18**). That suggests that the northern parts of the CIS were the main source of meltwater during the middle YD. The Sr isotopic composition in the core CL14PC was characterized by radiogenic values in the Holocene period after 11 ka, whereas Nd isotopic composition exhibited less radiogenic and decreasing values after 11 ka in this study, suggesting that the Holocene sediment might be a mixed sediment source. During this period (~11 ka), the opening of the Bering strait transports the Pacific warm water and Bering sediment to the Arctic Ocean via the Chukchi sea (Jakobsson et al., 2017; Sun et al., 2021).

In the core CL14PC, the ^{87}Sr/^{86}Sr isotopic composition was 0.705740 to 0.706718, and the ε_{Nd} isotopic composition was –1.62 to 0.1 during 9.0–17.2 ka. Thus, represent close similarity with the values of the Orca group's deep-sea fan sediments (early Paleogene) (Farmer et al., 1993), plutonic rocks from the Cordova area (Barker et al., 1992) as demonstrated by geologic and isotopic mapping of bedrock (**Figure 19**).

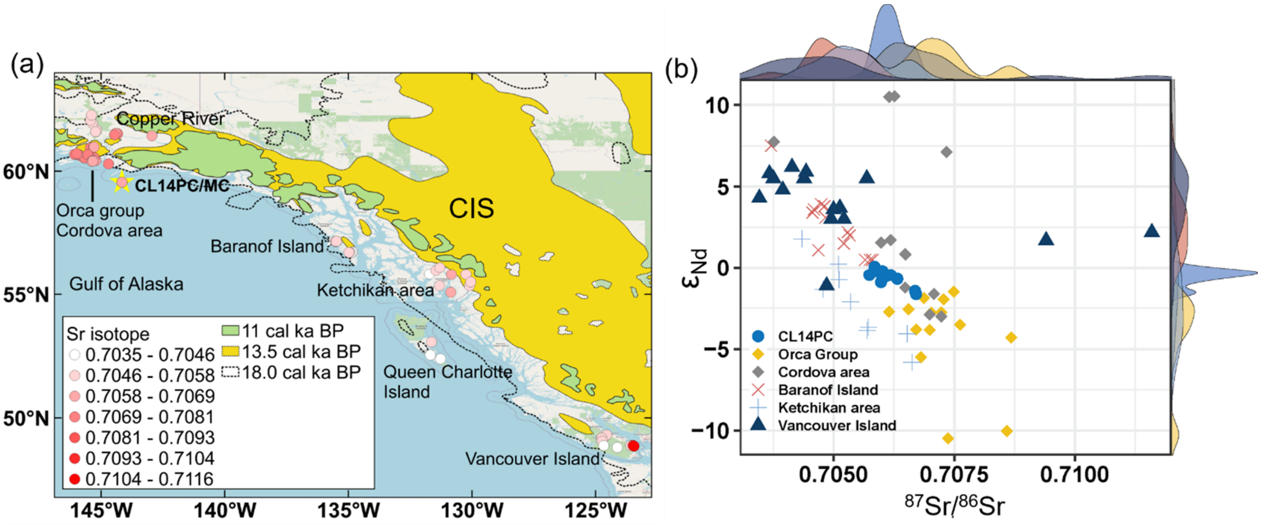

Figure 19. The Sr-Nd isotopic composition in the Gulf of Alaska core. (a) The QGIS (https://www.qgis.org/en/site) software-generated updated North American CIS extent

indicated at 18.0, 13.5, and 11.0 (^{14}C) cal ka BP (Dalton et al., 2020) in the Northeast Pacific. The (a) Sr isotopic compositions values and (b) ^{87}Sr/^{86}Sr isotopic compositions versus ε_{Nd} plot with their density plot in the top and right side are demonstrated for the bulk sediments of the core CL14PC (this study), and Orca Group's deep-sea fan sediments (early Paleogene) (Farmer et al., 1993), Cordova area's plutonic rocks (Barker et al., 1992), rock in the Eastern Chugach Mountains (Sisson et al., 2003), plutonic rocks in Baranof Island (Wackett, 2014), and batholith in the Ketchikan area (Arth et al., 1988) in the Northeastern Pacific.

The ^{87}Sr/^{86}Sr isotopic ratio of the Orca group's deep-sea fan sediments (Farmer et al., 1993) ranging from 0.70615–0.70868, which are very similar to the ^{87}Sr/^{86}Sr isotopic ratio in this study. This study's ^{87}Sr/^{86}Sr isotopic composition was also very similar to the Cordova area, such as Rude River Pluton, McKinley Peak Pluton, and Sheep Bay Pluton ^{87}Sr/^{86}Sr isotopic composition (0.70598–0.70734) (Barker et al., 1992). Similarly, the ε_{Nd} isotopic composition also showed close similarity of Cordova area (Barker et al., 1992) plutonic rocks ε_{Nd} isotopic composition, and the intermediate values for Orca group's (Farmer et al., 1993) deep-sea fan sediments ε_{Nd} isotopic composition (**Figure 19**). The Sr isotopes of bulk sediments from CL14PC are identical to Sr isotopes in the upstream Copper River (0.70606 ± 0.0006, $n = 11$), the proximal river to the core site (Brennan et al., 2014). The ^{87}Sr/^{86}Sr isotopic composition of the plutonic rocks in Baranof Island (Wackett, 2014) showed lower values (0.70500 ± 0.00059, $n = 13$), and the ε_{Nd} also showed a very high range (0.5–7.5) compared to this study. The core site (Baranof Island) was southeast of the core site of this study (**Figure 19**). The ^{87}Sr/^{86}Sr isotopic composition of Vancouver Island and Queen Charlotte Islands (Samson et al., 1990) had a wide range from 0.703458–0.711596 and most of the values lower than this study, and the values of ε_{Nd} isotopic composition are also far (very high) from this study. The Sr-Nd isotopic composition of the glacial-interglacial cycle of the Arctic marine sediments (Tütken et al., 2002) in the far north side of this study area showed a very high range of ^{87}Sr/^{86}Sr (0.712860–0.733329) and very low range (−3.6 to –14.0) of ε_{Nd} isotopic composition compare to this study. These all sediment provenance data confirm that the study area at Site CL14PC was dominated by offshore sediment transport through proximal large ice streams (Dunn et al., 2017). Moreover, detrital zircon represents that the proximal Bagley-Bering Glacier system transports the sediments on the continental shelf (nearby core site CL14PC).

3.6. Conclusion

High-resolution multiproxy records relating to oceanographic evolution from core CL14PC provide an opportunity to trace meltwater signals and constrain the timing of meltwater injection from the CIS into the northern GOA. Based on the integrated analysis of the generated datasets, we draw the following main conclusions: (1) The relative abundance of the tetraunsaturated C_{37} alkenones to total C_{37} alkenones denoted as $\%C_{37:4}$ alkenones ranged from 2 to 44% during the period 9.6–16.6 ka. During the late HS1 at ~16.4, ~16.2, and ~15.6 ka, three high peaks of $\%C_{37:4}$ alkenones were observed in the core CL14PC (this study) in the northern GOA. These peaks are concomitant with evidence of prominent IRD deposition, suggesting that surface freshening was associated with the melting of icebergs. However, planktonic foraminifer $\delta^{18}O$ records of CL14PC and other cores fail to document surface freshening during HS1. The IRD deposition results from the melting of icebergs, and coincident high peaks in $\%C_{37:4}$ alkenones, can be interpreted that sea surface conditions were low salinity during the period. (2) We found anomalously high values of $\%C_{37:4}$ alkenones during the early B-A at ~14.1 and ~13.9 ka. These high values of $\%C_{37:4}$ alkenones can be interpreted to reflect low salinity surface condition, also concomitant with prominent $\delta^{18}O$-depletion in the planktonic foraminifer record at 14.2–14.1 ka and 13.9–13.8 ka. In this study, the observed co-occurrence of higher $\%C_{37:4}$ alkenones and $\delta^{18}O$-depletion has very important implications; volumetrically significant meltwater was injected in the GOA during the early B-A. Furthermore, at 14.6–14.3 ka, the depleted planktonic foraminifer $\delta^{18}O$ and $\delta^{13}C$ signals suggest that meltwater was also injected in the northern GOA at 14.6–14.3 ka. The period might be related to differences in the seasons and depths of alkenone-producing haptophytes and planktonic foraminifer, and the meltwater inputs were not high enough to sustain lower salinity conditions throughout the year, especially in summer when alkenone-producing haptophyte algae bloom. These consistent records of $\%C_{37:4}$ alkenones and $\delta^{18}O$-depletion of planktonic foraminifer evidence robustly constrains that the warmer climate conditions during 14.6–13.8 ka caused multiple volumetrically significant meltwater injections into the northern GOA. This 800-years-long meltwater injection period is more extended than MWP-1A and the ice sheet model studies. (3) In the middle YD at ~12.2 ka, the extremely high $\%C_{37:4}$ alkenones (37 %) in core CL14PC can be explained by the influence of meltwater injection during the period. The interpretation supported by the benthic–planktonic foraminifer ^{14}C high age difference, freshwater, sea-ice, and sea-ice related diatom records from previous studies suggested meltwater signature during YD. The influence of YD meltwater injection seems to be restricted in the northern parts of the coastal GOA, unlike HS1 meltwater injection that is widespread over the coastal to the offshore GOA. (4) The %$C_{37:4}$ alkenone records did not indicate lower SSS after younger dryas a period of less bioturbated and weakly sub-laminated interval called Preboreal. The planktonic foraminifer isotopic composition also did not exhibit any distinct depleted value during the period. Therefore, this evidence indicates that after YD, the meltwater injection into the northern GoA was less significant. (5) The Sr-Nd isotope signatures of the core CL14PC constrain that the sediments' provenance was proximal to the core-site. The insignificant changes of $^{87}Sr/^{86}Sr$ and ε_{Nd} isotopic composition of the bulk sediments throughout HS1 to the middle YD indicate very similar sources of sediments and meltwater, being proximal to the core-site. Although, during the early B-A, the isotopic composition of bulk sediments exhibited a slight shift toward radiogenic values, however, the less significant changes in isotopic composition mean that even if a large amount of meltwater was injected into the GOA, detrital sources did not significantly change.

However, the integrated evidence from %$C_{37:4}$ alkenones, ice-rafted debris, planktonic foraminifera- and bulk sediment-stable isotopic records suggested that melt of the northern parts of the CIS injected a large amount of freshwater into the northern GOA following a substantial mass loss of the CIS during HS1 and in the early B-A to the middle YD. From the early B-A to the middle YD, the period was ~2,500-years (14.6–12.2 ka). These longer contributions of CIS melt to the global sea-level rise during the MWP-1A event were minor. Furthermore, these proximal multiple meltwater injections into the northern GOA are temporally disaggregated. However, their impact on the freshwater budget in the northeastern Pacific during the abrupt global sea-level rise (14.6–14.3 ka) was relatively small.

Chapter 4: Multiproxy analysis of high-resolution records revealing paleoproductivity change in the northern Gulf of Alaska

Abstract

The northern Gulf of Alaska paleoproductivity records required a high-resolution proxy investigation for firm constraints following the northern climatic intervals. Besides, the impact of meltwater injection on the paleoproductivity during the last deglaciation in the northern Gulf of Alaska has not been well constrained. In this study, by using a suite of new high-resolution geochemical records, stable isotopic records, carbon and nitrogen content, and multivariate analysis of high-resolution proxy reconstructed the detailed productivity during the last deglacial period from Heinrich Stadial 1 (HS1) to early Holocene (Preboreal) intervals in the Gulf of Alaska continental margin. The observed elevated productivity periods at 14.8–13.0 ka and 11.6–11.1 ka in this study marked by elevated Br and TOC-rich laminated sediments correspond to the regional expressions of Bølling-Allerød (B-A) and Preboreal, respectively. These findings indicate that high-resolution XRF Br robustly reflects the paleoproductivity changes in the northeastern GOA continental margin, which might yet be rarely considered in the region. The productivity proxies were consistently lower during the inferred meltwater period in the HS1 and Younger Dryas (YD). Probably, lower temperature, increased water turbidity, and deeper mixed layer with low light should be key variables for suppressing primary productivity during HS1 and YD. The productivity proxies did not tightly coincide with multiple peak meltwater periods in the B-A. The offset between *G. bulloides* and *N. pachyderma* (s) planktonic foraminifer δ^{18}O (‰) records decreases during elevated productivity periods, suggesting high vertical mixing. Thus, high vertical mixing, rapid warming, decreased mixed layer, and increased light creates a favorable condition in the euphotic zone for elevated productivity. The iron (Fe) from deglacial meltwater and inundated coastal depocenter enhanced productivity during the high productivity period (B-A and Preboreal). However, based on the new proxy from the core CL14PC, this study established a clear framework for regional paleoproductivity in the continental margin of the high latitudes, the northeastern Gulf of Alaska, during the last deglacial climate intervals.

4.1. Introduction

In chapter 2, this study discusses different methods for calibrating the X-ray fluorescence core scanner-generated high-resolution datasets. However, after transforming a large variety of raw datasets to a definitive calibration method, latent factors and information extraction, and identification of similar groups for further interpretation from such a vast dataset are complicated. Therefore, we can effectively disclose the inside implicit information to assess the dataset in a combination of cluster and principal components of multivariate analysis (Martin-Puertas et al., 2017; Schwestermann et al., 2020). This study analyzed the calibrated high-resolution XRF dataset from the Gulf of Alaska continental sediments by applying multivariate cluster and principal component analysis methods. The purpose of discovering their latent fact for further investigation and interpretation of the marine-based sediment core.

Biogenic silica (opal) was used in paleoceanographic studies as a productivity tracer (Addison et al., 2013). In the marine environment, diatom produces opal. Diatom frustules also contain a high concentration of Bromine (Leri et al., 2010). This study used the high-resolution Bromine (Br) with other productivity proxies to investigate paleoproductivity. Because Br makes a good discriminant of marine and terrestrial conditions (Malcolm & Price, 1984), terrestrial organic matter is comparatively poor in Br practically absent in terrestrial plants and animals (Dembitsky, 2002). On the contrary, Br and bromide salts are significantly more abundant in the oceans (Goodwin et al., 1997; Gribble, 2000; Dembitsky, 2002; Mayer et al., 2007; Rothwell & Croudace, 2015). Furthermore, marine phytoplankton and macroalgae produce abundant bromoalkaloids (Carpenter and Liss, 2000; Dembitsky, 2002) as the algal membranes provide suitable substrates (Bromoperoxidase) for bromination in the marine environment (Leri et al., 2014). Bromine is also uniquely well-suited to XRF core scanning analysis as it has high excitation energy ($K_{\alpha 1}$ = 11.9 keV) (Kido et al., 2006; Addison et al., 2013). Thus, the record of this productivity tracer is an excellent marine-based proxy that may reflect the changes of paleoproductivity in the northeast Pacific. Therefore, based on the multiple high-resolution datasets with the application of multivariate analysis approach, stable isotope ratios, carbon, and nitrogen content, and with relevant supportive data, this study reconstructed detailed paleoproductivity from Heinrich Stadial 1 (HS1) to early Holocene (Preboreal) during the last deglaciation in the GOA continental margin of the northeastern Pacific.

4.2. Materials and Methods

4.2.1 Core-site and sample collection

The details of the core site are described in the general introduction section (Subsection 1.3.) in chapter 1. From the site, a total of 869 cm long core was collected. The coring region is a highly productive ecosystem (Stabeno et al., 2016) characterized by winter strongest coastal downwelling (Childers et al., 2005), and early spring to summer coastal upwelling (Stabeno et al., 2004; Davies et al., 2011) dominated by the Alaska Coastal Current (ACC) (**Figure 20**). The ACC from the Alaska Gyre (AG) transports along with Alaskan Stream (AS) (Gorbarenko et al., 2019) toward the Samalga Pass of the Aleutian Islands this ~1700 km extending current system may drive by the along-shore winds (Stabeno et al., 2016).

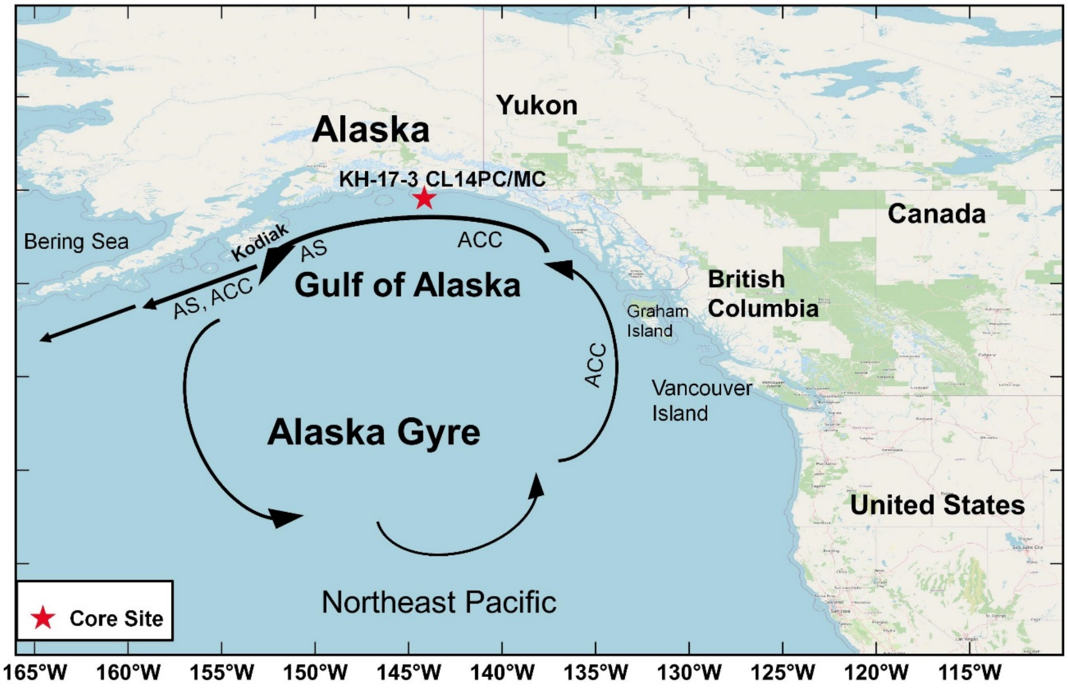

Figure 20. Map showing the surface circulation and current system in the subarctic northeast Pacific showing by black arrows. The current system mentions Alaska Coastal Current (ACC) and Alaska Stream (AS). The red star indicating the core (KH-17-3 CL14PC/CL14MC) location on the northeastern Gulf of Alaska continental margin.

4.2.2 Age model

Globigerina bulloides and *Neogloboquadrina pachyderma* (sinistral) planktonic foraminifer mixed ^{14}C, and molluscan shell ^{14}C dates were used to construct the radiocarbon (^{14}C) based age model. The age was calibrated by the Marine 13 (Reimer et al., 2013) calibration curve with reservoir correction of $\Delta R = 470 \pm 80$ years (McNeely et al., 2006) was used in this study. The details of the age-depth model construction are described in chapter 3 (Subsection 3.3.1.).

4.2.3. Multivariate analysis

The coherent/incoherent X-ray scatter ratio (CIR) calibrated ITRAX-XRF core scanner data were used to analyzed multivariate principal component analysis (PCA) and clustering analysis (CA). PCA is a popular multivariate analysis technique/method that reduces dimensions of the data, summarizing and visualizing important information contained in an observed variable by extracting the latent factors (principal components) (Loska & Wiechuła, 2003; Lee et al., 2019). These latent factors correspond to a linear combination of the original variables. Here, the main goal of analyzing our data under PCA is to identify the direction of maximal/important variation present/hidden in the data set and visualize graphically with minimal loss of existing information. Cluster analysis is another important multivariate analysis technique that identifies patterns or groups of similar objects within a data set of interest. A ggplot2-based R package named-

factoextra (http://www.sthda.com/english/rpkgs/factoextra), and

FactoMineR (http://factominer.free.fr/index.html) were used in this study for multivariate PCA and CA analysis. To avoid large differences in the mean and/or the standard deviation of the variables used for clustering analysis and for making the variables comparable, we standardized the data using the function *scale* (). The function transformed the data by using the following formula:

$$(x_i - \text{center}(x)) / \text{scale}(x) \tag{13}$$

Here, *center (x)* is the mean or median of the x values, and *scale (x)* is the standard deviation. In PCA analysis, the default function *PCA* () of the package *FactoMineR* automatically standardized the data using the *scale* () function, so there is no need for manual standardization. However, the following simple calculation is used for determining the major contribution of the applied variables in the variance of the first two principal components (PCs):

$$[(C1*E1) + (C2*E2)]/ (E1 + E2) \tag{14}$$

Here, C1 and C2 are the contributions of the variable in the variance of the first two dimensions, PC1, and PC2, respectively, and E1 and E2 are the eigenvalues of the first two dimensions (PC1 and PC2), respectively. Eigenvalues are the measurement of the amount of variation retained by each dimension (PCs). The first PCs have a larger eigenvalue. Then, a decrease in other PCs indicated that the first PCs contained/hold the direction of the maximum amount of variation in the contributing data set.

4.2.4. $CaCO_3$ content estimation and elemental analysis

The $CaCO_3$ (wt%) content was calculated from the following Equation (15) (Walinsky et al., 2009; Brunelle et al., 2010), assuming that total inorganic carbon presents as $CaCO_3$.

$$CaCO_3\ (\%) = (TC\ (\%) - TOC\ (\%)) \times 8.33 \tag{15}$$

For estimation of $CaCO_3$, the bulk sediments sample (*n* = 100) of archive halves first oven-dried at 50 °C for 24–48 h and make a homogenized powder sample with an agate mortar and pestle. Then the total carbon (TC) from the dried bulk sediments and total organic carbon (TOC) from the decarbonated sediments samples were analyzed by an elemental analyzer (Vario EL cube CHNOS). The preparation of decarbonated sediment samples is described in chapter 2 (Subsection 2.2.3.6.). Sulfanilamide ($C_6H_8N_2O_2S$) was used as a standard for calibration. The analysis was performed in the instrumental analysis division at the University of Toyama, Japan. A subsample from the same dried bulk sediment was used for total nitrogen (TN, *n* =100) content measurement. The relative standard deviations (RSD%) of the replicate measurements (*n* = 6) of the standard carbon and nitrogen were 0.3% and 1.3%, respectively. The estimate of $CaCO_3$ wt% should have an uncertainty of ~1.6% (RSD).

Values for the molar ratio of total organic carbon to total nitrogen (C/N) were calculated using the assessed TOC and TN content, according to the following equation (16) (Hedges & Stern, 1984; Walinsky et al., 2009).

$$C/N = (TOC\ (\%)/12)/\ (TN\ (\%)/14) = (TOC\ (\%)\ /\ TN\ (\%)) \times 1.167 \qquad (16)$$

4.2.5. Lead (Pb) isotopes measurement

After complete drying of a sample taken from the stock solution prepared through sequential leaching and acid digestion (Appendix A.2.3.) were re-dissolved with 8 M HNO_3 (KANTO Ultrapure-100) to separate the Pb fraction. After conditioning and sample loading (500 µL) in the cation exchange column, the Pb fraction was collected from the sample solution with 6 M HCl (KANTO Ultrapure-100) eluent. The separation of Pb has carried out as- (1) major elements were removed from samples solution by using a cation exchange resin column with 8 M HNO_3, (2) The Sr fraction was removed by adding 0.05 M HNO_3 to the column, and (3) after rinsing with ultrapure water and 2.5 M HCl the Pb fraction was collected in a Perfluoroalkoxy (PFA) Teflon (Savillex®) vial by 6 M HCl. All procedures were done in a clean laboratory at the University of Toyama, Japan. Pb aliquots from column chemistry were dried and re-dissolved with 3% HNO_3 before aspiration. Pb isotopic ($^{208}Pb/^{204}Pb$, $^{207}Pb/^{204}Pb$, $^{206}Pb/^{204}Pb$) compositions were analyzed on a high-resolution multi-collector inductively coupled plasma mass spectrometer (MC-ICP-MS) NEPTUNE (Thermo Fisher Scientific) at the Research Institute for Humanity and Nature (RIHN), Kyoto, Japan. Lead isotopes $^{208}Pb/^{204}Pb$, $^{207}Pb/^{204}Pb$, and $^{206}Pb/^{204}Pb$ ratios (mol/mol) are normalized to a value of 38.0626, 15.6278, and 18.0900 for NMJI CRM 3681-a Pb standard from national metrology institute of Japan (NMJI), which averaged 37.9535 ± 0.0168, 15.5891 ± 0.0062, and 18.0534 ± 0.0064 (2σ, $n = 32$), respectively at the time of analysis.

4.3. Results

4.3.1. Multivariate (CA and PCA) analyses results

The CIR calibrated XRF core scanner data ($n = 5880$, number of elements = 7) were used to form multiple groups (clusters) according to their similarity. In this study, the K-means clustering method was used to determine the optimal number of clusters as CL14PC has multiple anomalous data points. The K-means clustering (MacQueen, 1967) method makes each cluster based on the mean or center of the data within the cluster. The basic idea behind K-means clustering consists of defining clusters so that the total intra-cluster variation (known as a total within-cluster variation) is minimized. The K-means clustering method found five (K = 5) optimal clusters in the high-resolution ITRAX-XRF core scanner data (*n* = 5880, number of elements = 7). The visualization of the entire clusters in the *elbow method* showed (**Figure 21A**) that if the number of clusters increases after five, the total within the sum of squared (wss) distances (Euclidean distances) of the cluster variation showed very minimal differences and closed each other. Thus, indicating that five is the appropriate/optimal number of clusters based on the contributed data set. A statistical procedure of estimating the number of clusters name *gap statistic* (R function name *{NbClust}*) described that among the seven indices more than 50% that is four indices proposed 5 are the optimal number of clusters in the data set. After specifying the optimal number of clusters (K-means algorithm), we were again partitioning the clusters by hierarchical cluster analysis (HCA) *dendrograms* (tree-based representation of objects) (Lê et al., 2008; Husson et al., 2017). In this agglomerative clustering (HCA) method, we computed the distances by the *Euclidean method*. And, the linkages are computing by *Ward.D2* (Ward, 1963; Murtagh & Legendre, 2014) linkage method. These are similar to previous studies for high-resolution XRF core scanner records and paleoceanographic studies (Martin-Puertas et al., 2017; Penkrot et al., 2018; Lee et al., 2019). These methods are used in this study because they minimize the total within-cluster variance, pair the cluster with minimum between-cluster distance merged, and link the cluster with the smallest linkage distance. After cutting the cluster dendrogram tree (plot), we visualized (label) each cluster as C1, C2, C3, C4, and C5 by different colors like deep sky blue, red, dark blue, dark violet, and lime green, respectively, (**Figure 21B, 22B**). Among the five clusters, C4 was the largest cluster group consist of 371 data points of each element, and most of the data points come from the early-Holocene (EHC) ~10.8–3.1 calibrated thousand years (ka) before present (cal ka BP). Cluster 2 (C2) was the deglacial (DG, ~14.8–10.8 cal ka BP) cluster group that consists of relatively lower data points (73 from each element).

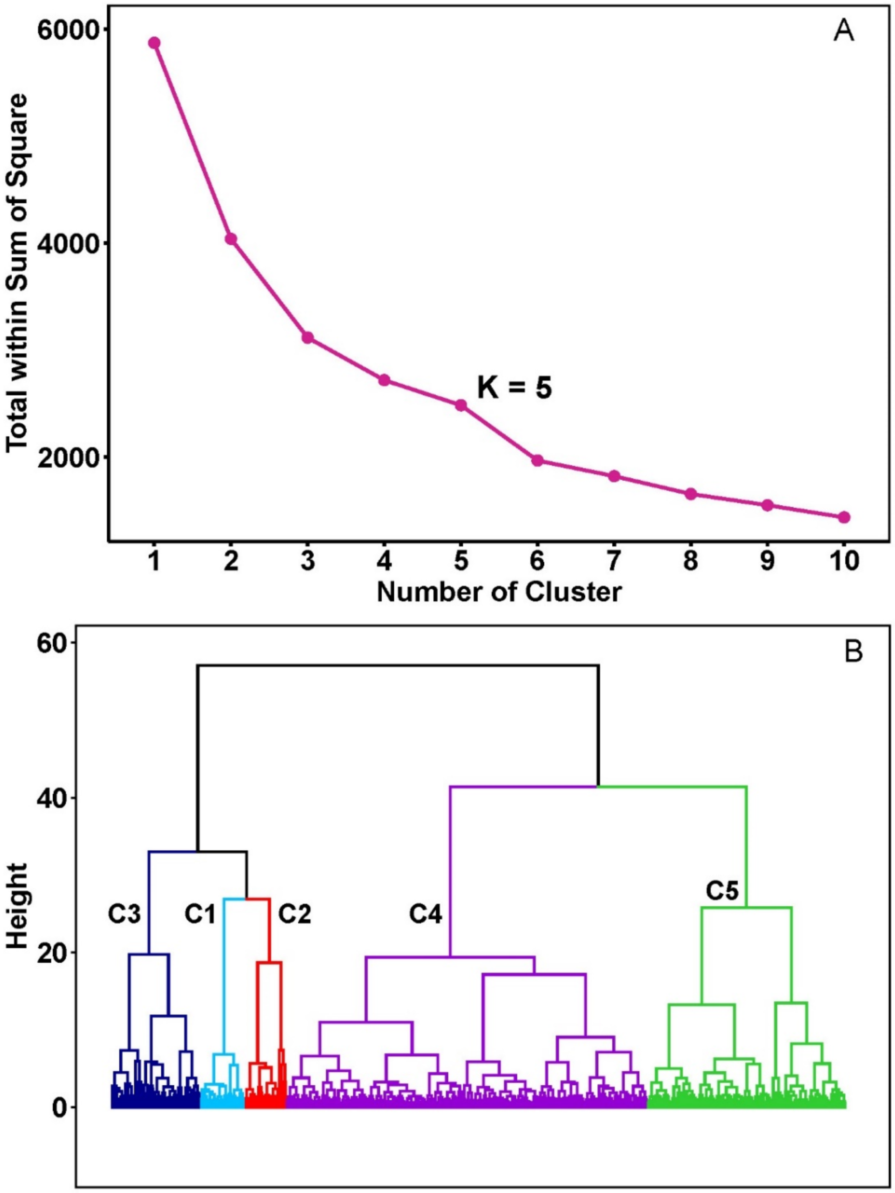

Figure 21. The multivariate analysis results of (A) visualize the optimal number of clusters by the elbow method (k-means clustering). Here, K = 5 means the data have five optimal clusters, (B) cluster dendrogram, and C1, C2, C3, C4, and C5 indicated cluster group.

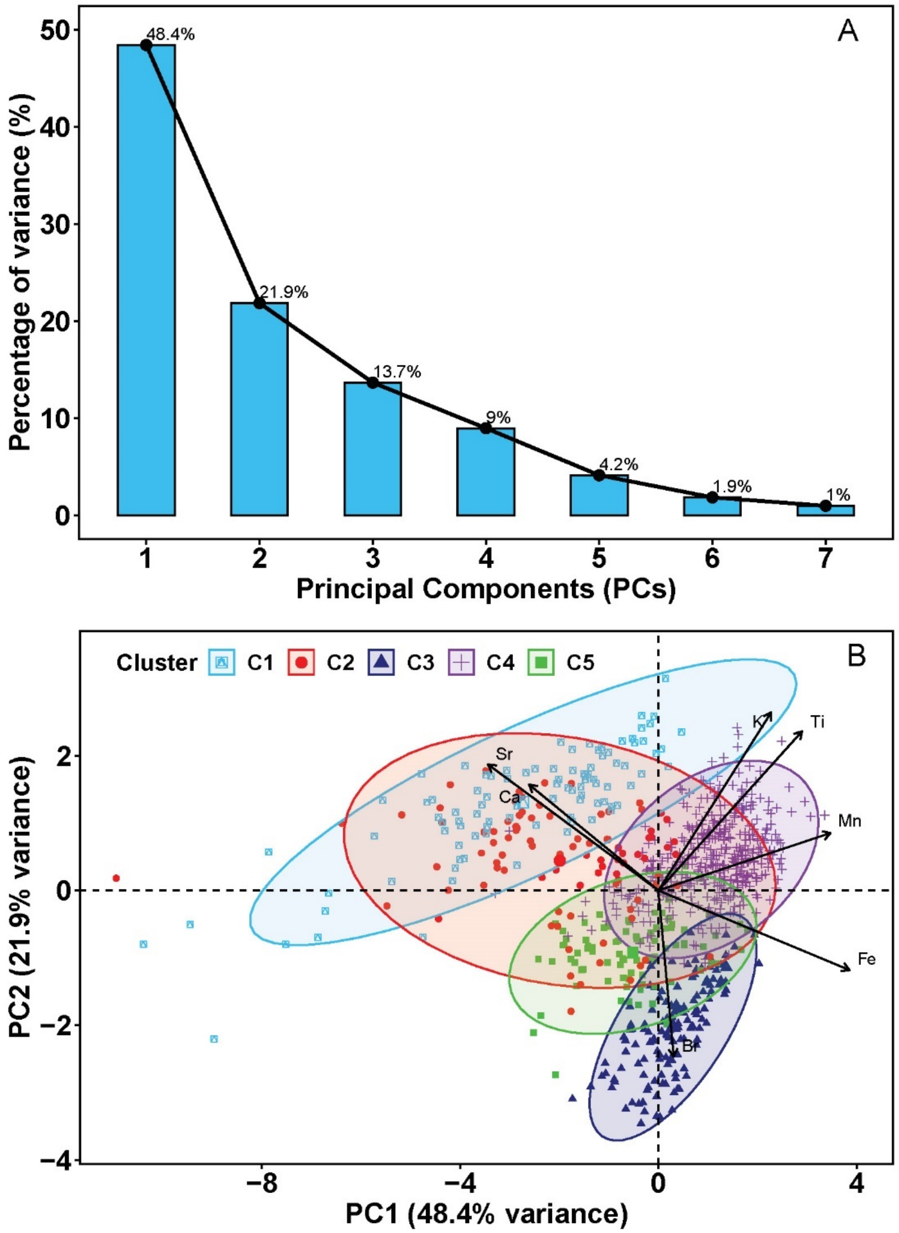

Figure 22. (A) the scree plot of principal component analysis showing the number of dimensions (principal components) in the x-axis and the percentage of variance (%) in the y-axis, and (B) the biplot of individuals and variables of the first two principal components PC1 (48.4%) and PC2 (21.9%). The color marked by deep sky blue, red, dark blue, dark violet, and lime green indicated C1, C2, C3, C4, and C5 clusters, respectively.

In the principal component analysis, the eigenvalues of the first and second dimensions (PCs) were 3.39 and 1.53, respectively, and the corresponding percent of variances was 48.4% and 21.9%, respectively (**Figure 22A**). Besides the first two eigenvalues, the rest of the eigenvalues gradually decrease in the principal components (dimensions), and the value was minor (0.07) in the last PCs (seven), simultaneously the percent (%) of variance gradually decreased up to the last PCs (**Figure 22A**). The cumulative (total) variance (%) of the first two and three PCs were 70.3% and 84%, respectively, indicating that most of the variances were retained by the first three PCs. The variance in the principal component analysis showed that Fe, Mn, and Sr are the main contributor to the variability in the first PCs. In the second PC, K, Br, and Ti are the main contributor. According to equation (14), Fe, Sr, and Ti are major contributors to the PC1 and PC2 variability. The cumulative quality (square cosine ($\cos^2$)) of the major contributors (Fe, Sr, and Ti) in the factor map (Lê et al., 2008) analysis were 0.93, 0.88, and 0.80, respectively. The Fe, Sr, and Ti position in the factor map was close to the circumference of the correlation circle (**Figure 23**), indicating that these variables are the highest contributors in the first component. The individuals and variables, their group (cluster), and their contribution to the dimensions (PC1 and PC2) are projected by a *biplot* (**Figure 22B**). The factor map showed that the Br and Ca are relatively far from the circumference of the correlation circle. And, the color gradients of these two variables are different from Fe, Sr, and Ti (**Figure 23**), indicating that they have a relatively low contribution in the first component. Furthermore, the principal component analysis showing that Br and Ca are the major contributor to the PC3 (**Figure 24**). The eigenvalues and the corresponding variances (%) of PC3 were 0.96 and 13.7%, respectively (**Figure 22A**).

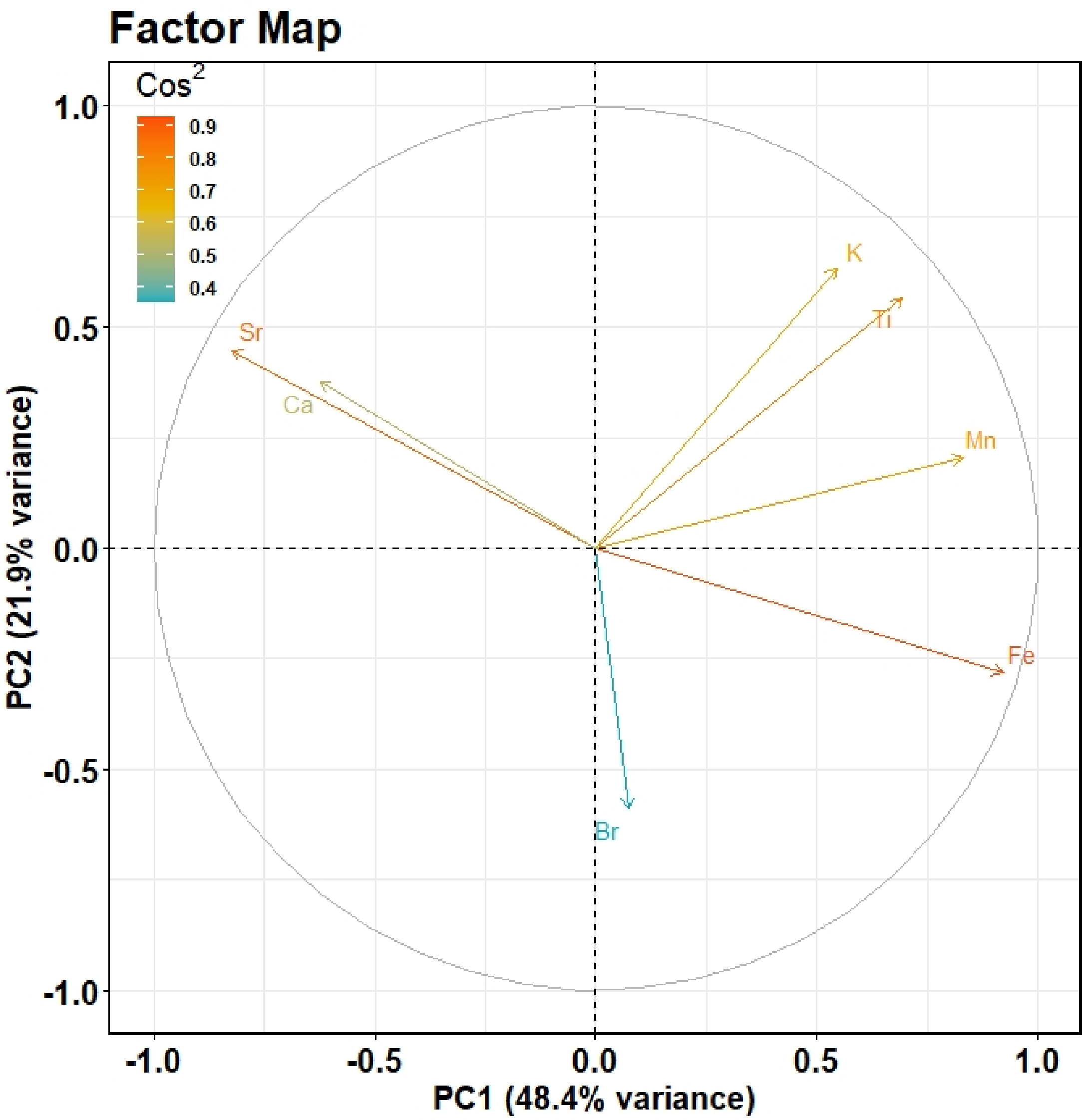

Figure 23. The factor map shows the variable correlation in the first two principal components (PC1 and PC2). The color gradient and values of square cosine ($\cos^2$) indicate the variables' representation of the principal component. The high $\cos^2$ values indicate a perfect correlation of the variables on the first two PCs. In that case, their position is away from the origin. That is, close to the circumference of the correlation circle like Fe, Sr, and Ti.

The correlation between variables and dimensions for Br and Ca in PC3 were 0.79 and 0.40, respectively. Taken together, we considered PC3 as a representative of marine proxy (**Figure 24**). In PC4, the eigenvalue was 0.63, and the percent variance and cumulative variance were

8.99 % (**Figure 22A**) and 93 %, respectively. The variables contributing to PC4 variance were Ca, Mn, and K; of them, Ca was the main contributor (45.9%).

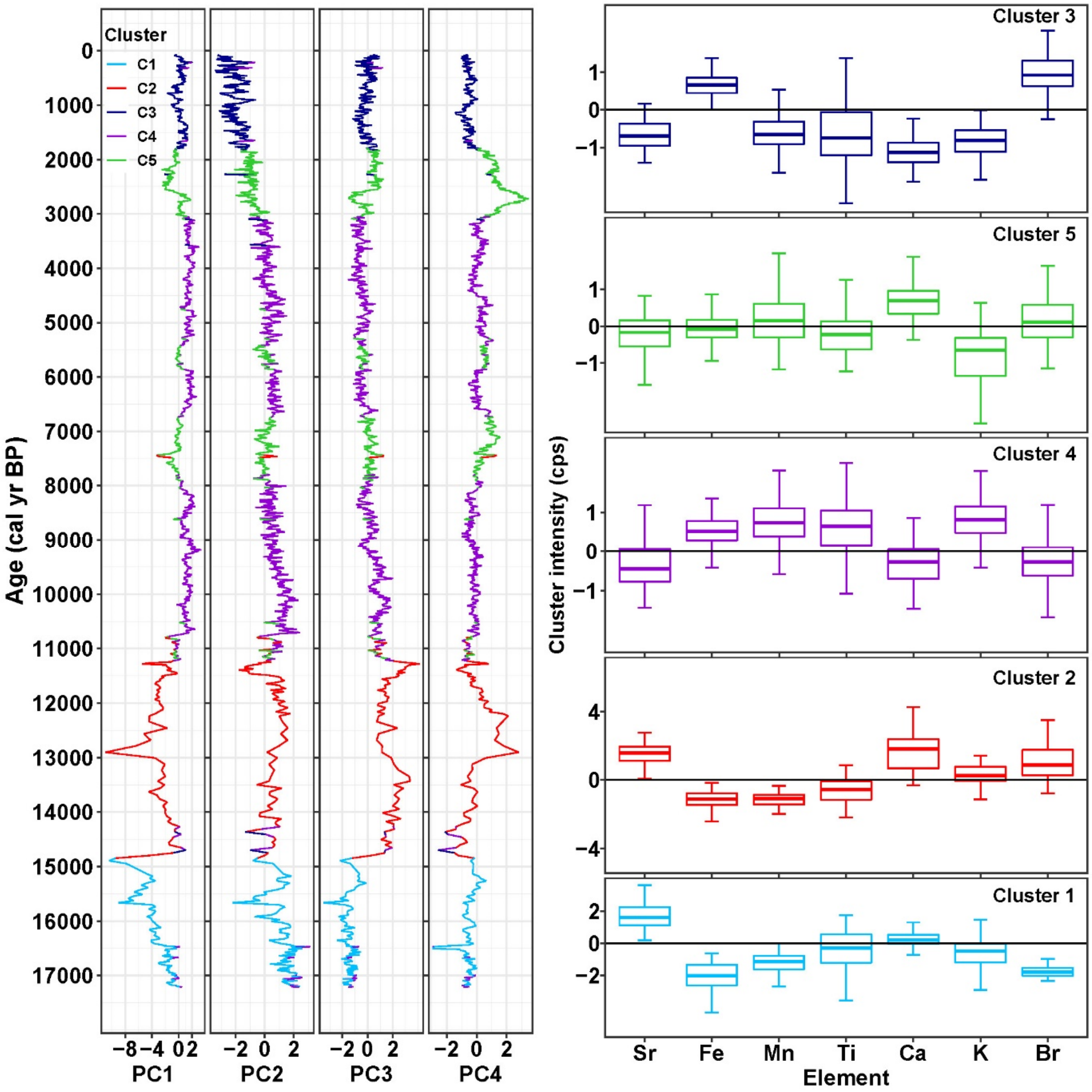

Figure 24. The left-side figure indicating the down-core score profile of the principal component plotted against age (cal yr BP), with five clusters marked by deep sky blue, red, dark blue, dark violet, and lime green color-coding of clusters C1, C2, C3, C4, and C5, respectively. The right-side figures showing the Box-whisker plots of the mean values of the scale data with their error bar of each element in each cluster group and the elements plotted in the y- and x-axis, respectively.

4.3.2. Elemental proxy result

The sedimentary Al or Ti is exclusive of detrital source, and XRF derived Ca normalized with Al and/or Ti reflect biogenic $CaCO_3$ content within the sediment (Jaccard et al., 2005; Riethdorf et al., 2013). Although the Al and Ti show almost identical trends and amplitude, in the core CL14PC, the XRF Ti signal was better than Al. So, in this study, we favored the Ca/Ti ratio to correlate with $CaCO_3$ (wt%) content and found a high coefficient of determination between them ($R^2 = 0.64$, **Figure 25**).

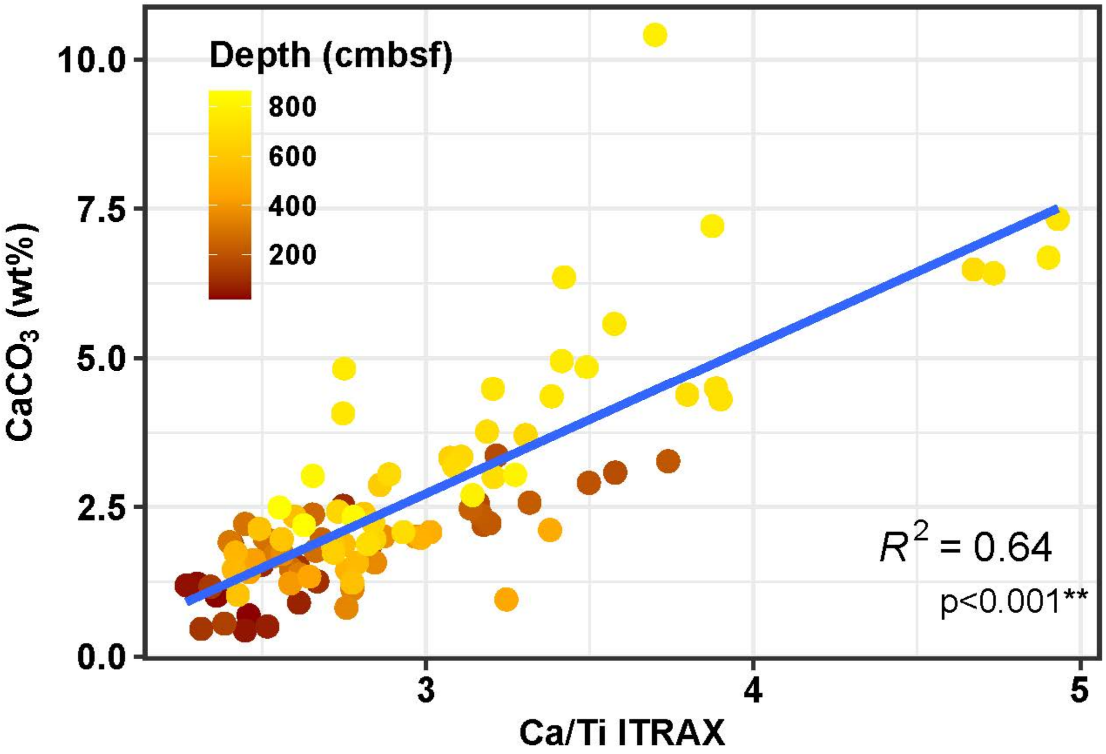

Figure 25. The scatterplots between $CaCO_3$ (wt%) content and Ca/Ti ratio of the core CL14PC. The down-core profile indicates the depth (cmbsf) color gradient, and the linear regression indicates the straight blue line. The coefficient of determination (R^2) is presented at the right-bottom corner of the plot.

Comparison of $CaCO_3$ (wt%) and ITRAX Ca/Ti ratio was revealed that $CaCO_3$ (wt%) estimate got higher values than Ca/Ti ratio at some sedimentary horizons (**Figure 26**). Probably, this difference comes from the difference between surface measurement in a narrow area by ITRAX and a destructive measurement of homogenized samples by an element analyzer. That happens due to biogenic calcite since calcium carbonate and foraminifer are often found in the patch and not homogenous distribution. As a result, during grinding of dry sample for discrete measurement, the calcite shells and foraminifer fragments also grinding with sediment sample make a homogenizes $CaCO_3$ content in the sample. Thus, increase its values during measurement (Tjallingii et al., 2007). However, the mean $CaCO_3$ (wt%) content and Ca/Ti ratio in the deglacial B-A was greater than HS1 and Holocene transition and lower than YD.

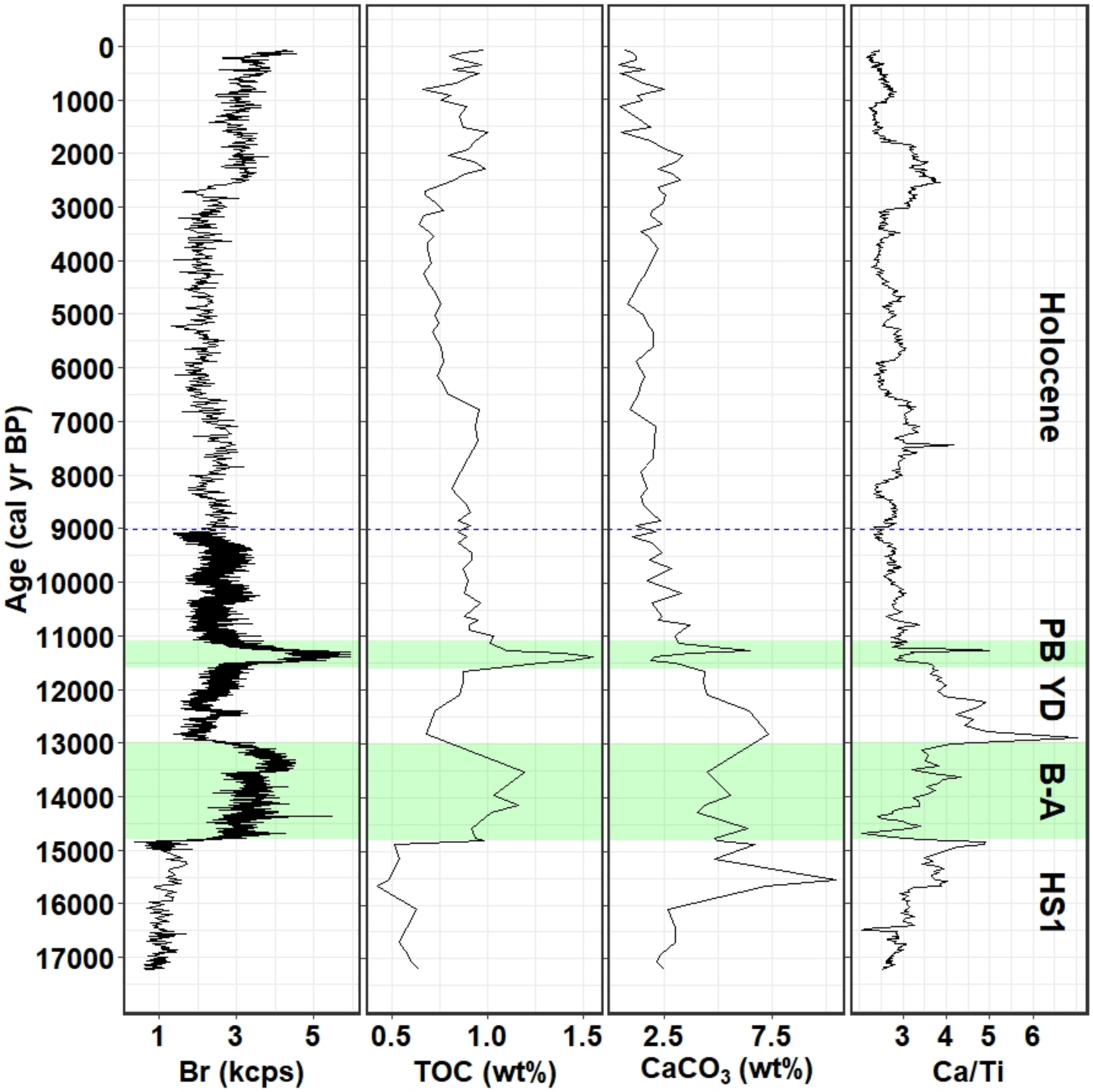

Figure 26. The paleoproductivity record of Br (kcps, the thick black line means 0.4 mm and a thin line indicating 1 cm resolution) and TOC (%), and the carbonate content ($CaCO_3$ (wt%)) and Ca/Ti ratio is plotted versus age (cal yr BP) during the last 17200 cal yr BP of the core CL14PC. The green color shaded period indicating the high productivity in the northern Gulf of Alaska continental margin. The vertical dashed line (blue dash line) at 9.0 cal ka BP indicates the starting of the downcore deglacial section considered for focusing (9.0–17.2 cal ka BP) on this study. The peak productivity period is highlighted in the plot by green color shade during the B-A 14.8–13.0 ka and during the PB 11.6–11.1 ka. The timing of the major climate intervals is demarked in the plot as HS1 (Heinrich Stadial 1, 17.2–14.8 ka), B-A (Bølling-Allerød, 14.8–13.0 ka), YD (Younger Dryas, 13.0–11.7 ka), PB (Preboreal, 11.7–10.8 ka), and Holocene (10.8–end ka) name mention at the right end of the plots.

In multivariate cluster analysis, during the C1 cluster (HS1) period, the TOC (wt%) content was lowest; on the other hand, the C/N ratio was highest. During the deglacial B-A and PB in cluster 2 (C2), the TOC (wt%) content was higher than the HS1, YD, and overall Holocene period, and the C/N ratio was opposite.

4.3.3. Pb isotopic composition during the last deglaciation

In addition to Sr and Nd isotopic composition, the Pb isotopes ratio is widely used to reconstruct provenance changes and is an important tool for geochemical studies of source identification (Aung et al., 2004; Ferrat et al., 2012). Among the four stable isotopes (^{208}Pb, ^{207}Pb, ^{206}Pb, and ^{204}Pb), ^{208}Pb has the heaviest stable nucleus and is radiogenic (Komárek et al., 2008). Among the measured Pb isotopic composition, ^{208}Pb/^{204}Pb from 9.0–17.2 ka during the last deglaciation is used in this study (data reported in Appendix B **Table B5**). The isotopic composition of ^{208}Pb/^{204}Pb during the last deglaciation ranging from 38.8265–38.9939. The ^{208}Pb/^{204}Pb isotopic ratio of the Orca group's deep-sea fan sediments ranging from 38.611–39.209 (Farmer et al., 1993). The Cordova area, such as Rude River Pluton, McKinley Peak Pluton, and Sheep Bay Pluton ^{208}Pb/^{204}Pb isotopic composition was 38.619–38.845 (Barker et al., 1992). These values are similar to the ^{208}Pb/^{204}Pb isotopic ratio in this study. These (Orca groups and Cordova) sites are the offshore proximal to the CL14PC (this study) core site, similar to the Sr and Nd isotopic source.

4.4. Discussion

4.4.1 Heinrich stadial 1 (~17.2–14.8 cal ka BP)

The cluster analysis showed that the Heinrich Stadial 1 sedimental profile consists of cluster 1. According to the downcore profile of the core CL14PC, the Heinrich Stadial 1 was the most profound part, so that the sediments in this interval represent the core bottom. The low cluster (C1, **Figure 21B**) mean of XRF Br count (1086 cps) and low TOC (0.56 wt%) content during the period suggesting low productivity (**Figure 26**). The principal component analysis (**Figure 24**) showed that the sediment consists mainly of terrigenous sediment with low marine-based sediment content (PC3). The high C/N molar ratio (15–24) indicating the high content of terrestrial organic matter in the sediment consistent with the principal component analysis result and low marine-based productivity. During this period (HS1), the GOA was comparatively colder and experienced more significant deposits of abundances of ice-rafted debris (IRD) (**Figure 3** (CT-scan image) and **Figure 16**, the white color area indicating IRD) by advanced icebergs/glacial flour in the coastal settings. That time, the GOA was similar to one of the many glaciated fjords along the modern coast, with a cold and strongly stratified euphotic zone (de Vernal & Pedersen, 1997), with a high concentration of suspended sediment, icebergs, and seasonal sea ice (Barron et al., 2009). As with glacial flour, the fine sediment was released and dispersed from melting icebergs along with coarser-grained material. That increased the water turbidity, together with low temperatures significantly deepening the mixed layer, and severely reduced the light availability for phytoplankton (Keigwin et al., 1992), and suppressed primary productivity. The productivity proxy in the core CL14PC indicated low productivity during this period, consistent with the above explanation.

In the early HS1, the $CaCO_3$ content was low 2–3 wt%. At ~15.6 cal ka BP the $CaCO_3$ content was abruptly increased with an exceptional peak (10.4 wt%) at 15.5 cal ka BP (**Figure 26**), then sharply decreased. This period was synchronized with the high relative abundance of C_{37} alkenones (%$C_{37:4}$) content discussed in the previous chapter (chapter 3). During this short period, low sea-surface temperature (SST) and sea-surface salinity (SSS) induced haptophyte, especially coccolithophorid. Thus increase more production and preservation of $CaCO_3$ in the sediment. Coccolithophores are the primary producer of alkenone (Seki et al., 2004). $CaCO_3$ enclosed their (Coccolithophores) exoskeleton made calcareous plates called coccoliths. Barron et al. (2009) found coccoliths throughout their core except for the late Holocene. Although they (Barron et al., 2009) have no data in the early HS1 (after 15 ka), our high alkenones (%$C_{37:4}$) content in the HS1 suggesting that coccoliths were also common during the period. Therefore, a part of the high carbonate content in the HS1 may come from the haptophyte. However, this had no impact on productivity changes as this was a less productive period, with lower values of productivity proxies (Br and TOC) consistent with this. Alternatively, as this short period (15.6–15.5 cal ka BP), the ice-rafted debris was abundantly high (**Figure 18**), and the C/N ratio showed high values ranging from 22–20, suggesting that the excess carbonate may derive from detrital carbonate and grinding made a homogenous distribution during measurement. However, the Ca/Sr ratio and Ca/Ti ratio during the period (~15.6–15.5 cal. ka BP) did not show concomitant abrupt high values. Suppose biogenic and/or detrital calcite was distributed in a patch. In that case, the ITRAX sometimes miss to detect such element signal may be the reason for not significantly changing the Ca/Sr and Ca/Ti ratio. On the other hand, grinding of dry sediment samples made a homogenous distribution of consisted calcite shells and calcareous plates easily detected by a discrete elemental analyzer. During HS1, the average excess Sr showed in cluster 1 in **Figure 24** may be obtained from calcareous plates as it contains higher Sr (Rothwell & Croudace, 2015) and/or in combination with terrigenous (detrital) sources Sr as higher C/N ratio and IRD found in this period.

Although the $^{208}Pb/^{204}Pb$ and $^{87}Sr/^{86}Sr$ isotope ratios slightly decreased and ε_{Nd} isotope ratio slightly increased in the late HS1 from early HS1 and the $^{208}Pb/^{204}Pb$ and $^{87}Sr/^{86}Sr$ isotope ratios showed a slight discrepancy in some horizon. However, the variation was not significant and similar in trend, suggesting that the sediment's provenance did not change during the period; the K/Ti ratio (**Figure 29**) did not show any abrupt change, which was also consistent with this.

4.4.2. Deglacial period (~14.8–10.8 cal ka BP)

Previous studies from northeast Pacific sediment cores have shown that the millennial-scale deglacial oceanographic changes occurred in phase with northern hemisphere climate oscillations, such as HS1-B-A-YD-PB during the last deglaciation. Herein, we discussed the productivity changes in the GOA during the last deglaciation. We mainly focused on HS1 to PB in terms of the high-resolution XRF multiproxy and their multivariate analysis combined with TOC, $CaCO_3$ content, C/N ratio, and sediment provenance. Besides, we also discuss the relation with the productivity to the ice sheet (CIS) dynamics (meltwater from ice sheet) during the last deglacial transitions. The multivariate cluster analysis (C2, **Figure 21B, 22B**) during this period indicated that the cluster means of the participating marine-based proxy was higher

(Br = 3386 cps) than all other clusters. Furthermore, the PC3 in the principal component analysis where Br and Ca were the major contributor showed a rapid increase with a positive trend started from ~14.8 cal ka BP and then a sharp decrease at ~10.8 cal ka BP (**Figure 24**). However, this extended period (14.8–10.8 cal ka BP) in cluster 2 consists of deglacial B-A, YD, and PB climate transitions. Here we describe details of each transition event based on the multiproxy proxy records.

At the onset of B-A (~14.8 cal ka BP, ranging 14.3–15.2 cal ka BP with a 95% confidence interval), the XRF Br started a sharp increase, and the ongoing elevation ended at ~13.0 cal ka BP (ranging 12.7–13.3 with a 95% confidence interval) (**Figure 26**). The Low C/N ratio suggests low terrigenous organic matter in the sediment; on the other hand, high XRF Br is closely parallel to the high TOC content (**Figure 27**), suggesting that marine algae are the dominant contributor in TOC during this period. In the case of $CaCO_3$ and Ca/Ti ratio, we found a minor increase compared to overall HS1, but lower values compared to YD; this is because high opal (Addison et al., 2012) content diatom (Barron et al., 2009) is the predominant species during this high productivity period. Opal or biogenic silica is a hydrated amorphous form of silica ($SiO_2.nH_2O$), is one of the most widespread biogenic minerals instead of the other major biogenic minerals comprising carbonate and phosphate. On the other hand, marine diatoms abundantly produce organo-bromine compounds in the ocean (Hill & Manley, 2009; Lim et al., 2017). And, the diatom frustules also contain a high concentration of Br (Leri et al., 2010). Besides, silicoflagellates and Dinoflagellate are also abundant during this period (Barron et al., 2009; Tomokawa et al., 2019). However, the high lamination and low oxygen content in the bottom water also influence the low preservation of $CaCO_3$ in the sediment. During this period, the XRF Br robustly exhibited higher values showed a highly significant coefficient with TOC ($R^2 = 0.72$) (**Figure 27**) and a good agreement with opal contents from nearby core EW0404-85JC (Addison et al., 2012). This evidence confirms that XRF Br from the core CL14PC reflects the marine productivity changes. Indeed, during B-A, Br was at least three times higher (Br in B-A = 3660 cps, and in HS1 = 1086 cps), and the TOC concentration was double (TOC in B-A = 1.04 wt% and HS1 = 0.56 wt%) relative to HS1 values. Microfossil proxies (Barron et al., 2009) and enhanced nutrient utilization (Addison et al., 2012) also supported abruptly increased productivity during the B-A warm interval. As seawater Br sometimes overprints on algal Br, the XRF core scanner Br intensities (cps) are sometimes normalized by Cl intensities (cps). The Br/Cl ratio in this study, however, showed weaker correlation (**Figure 27**) with TOC ($R^2 = 0.64$, $n = 100$). As Cl had a lower count with a relatively higher RSD%, Br/Cl ratios might involve large error propagation, thus losing the tight correlation with TOC. However, during the elevated productivity in the B-A period, the surface paleotemperatures remained elevated, induced persistent hypoxic conditions, and a sharp transition to sediment laminations (Praetorius et al., 2015). During the period (B-A), enhanced productivity leads to increased accumulation of algal products in deep northeast Pacific sediments. The enhanced productivity also consistent with the variation of PC3 in the principal component analysis (**Figure 24**).

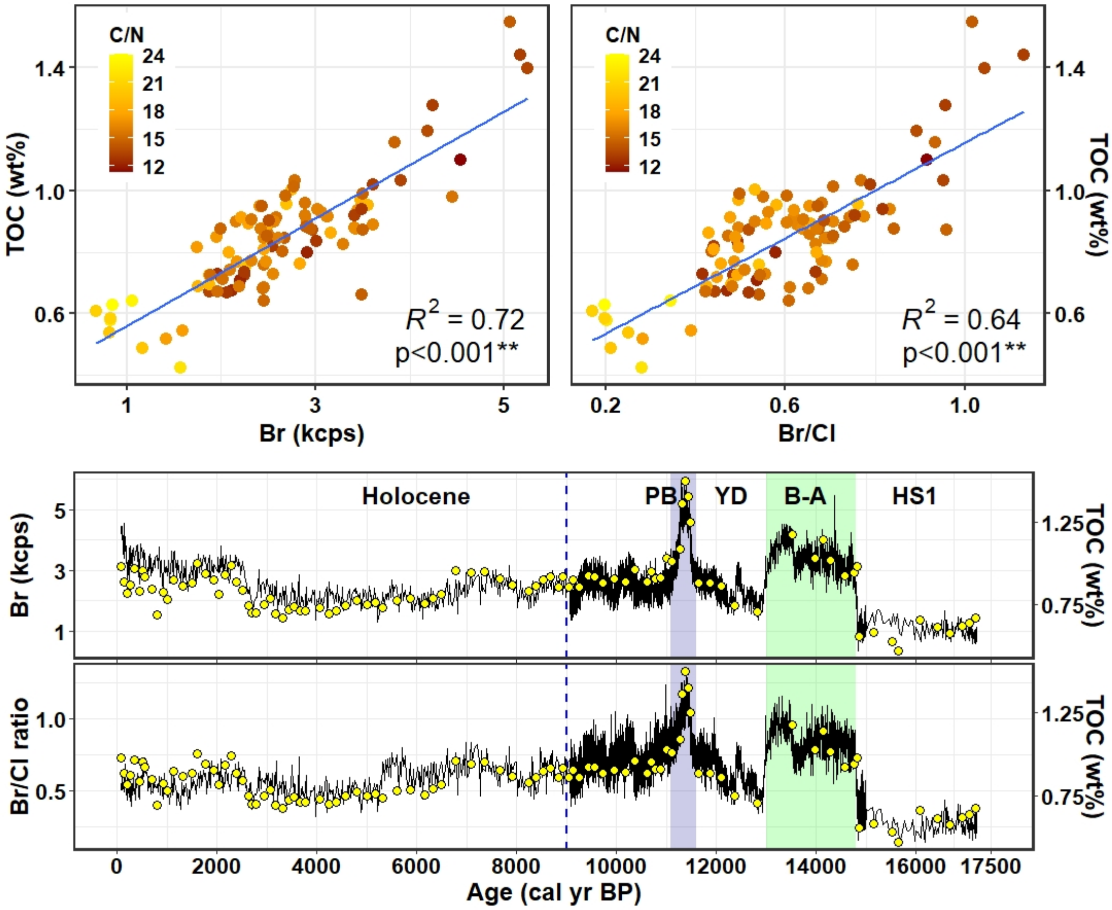

Figure 27. The upper figures indicating of scatterplots between ITRAX-XRF CS Br (kcps, left side) and Br/Cl ratio (right side) versus total organic carbon (TOC wt%) content of the core CL14PC with linear regression line (blue color) and color gradient by C/N ratio. The coefficient of determination (R^2) presented at the bottom right corner $R^2 = 0.72$ $p < 0.001$ ($n = 100$) for Br (kcps) versus TOC (wt%), $R^2 = 0.64$, $p < 0.001$ ($n = 100$) for Br/Cl ratio versus TOC (wt%). The details Br (kcps) and Br/Cl ratio and TOC (%, black circle yellow color) are plotted versus

calibrated calendar age (cal yr BP, x-axis) in the lower figures. For Br and Br/Cl ratio, the thick black line indicates 0.4 mm resolution, and the thin black line indicates 1 cm resolution. The timing of the major climate intervals as HS1, B-A, YD, PB, and Holocene is mention at the top of the plots. The elevated (peak) productivity period is highlighted in the plot by green color shade during the B-A (14.8–13.0 ka) and by dark blue color shade during the PB (11.6–11.1 ka). The vertical dashed line (blue dash line) at 9.0 cal ka BP indicates the starting of the downcore deglacial section considered for focusing (9.0–17.2 cal ka BP) on this study.

The remineralization of sinking particles within the sediment and water column enhanced low bottom water oxygen concentration due to organic matter decomposition and triggering laminated sediment formation. During B-A, rapid warming and a large amount of meltwater supplied from the Cordilleran Ice Sheet (Marcott et al., 2011; Maier et al., 2015; Menounos et al., 2017; Maier et al., 2018; Müller et al., 2018) cause freshening of surface waters. Probably, this abrupt input of meltwater might have shut down relatively deep convection (Keigwin et al., 1992; Lam et al., 2013). As a result, the high nitrate from deep convection would be trapped in the shallow and high-light mixed layer, coupled with the high iron flux. During this period, surface warming may also influence massive nutrient supply (Gebhardt et al., 2008), and modern-day Alaska Gyre circulation advects shallow nitrate-rich water toward the continental shelf of the GOA (Childers et al., 2005). Besides, the deglacial meltwater from the decay of CIS in response to the abrupt sea-level rise inundated (Addison et al., 2012) coastal depocenters. Thus, increase the supply of iron through remobilization (Davies et al., 2011). All of these create a favorable condition in the euphotic zone for deglacial high primary production. The high Br and TOC peaks in the core CL14PC reflect these elevated deglacial productivities in the period (B-A).

The distinctly lower salinity and depleted planktonic foraminifer δ^{18}O at ~14.6–14.3, ~14.2–14.1, and ~13.9–13.8 cal ka BP during the B-A transition that showed a meltwater signature did not tightly coincide with significant productivity change (**Figure 28**). The high productivities may enhance by high vertical mixing between the surface and sub-surface layers during the period. Minor offset (0.09‰) of δ^{18}O records between *G. bulloides* and *N. pachyderma* (sinistral) (**Figure 28**) is consistent with this idea (Gebhardt et al., 2008).

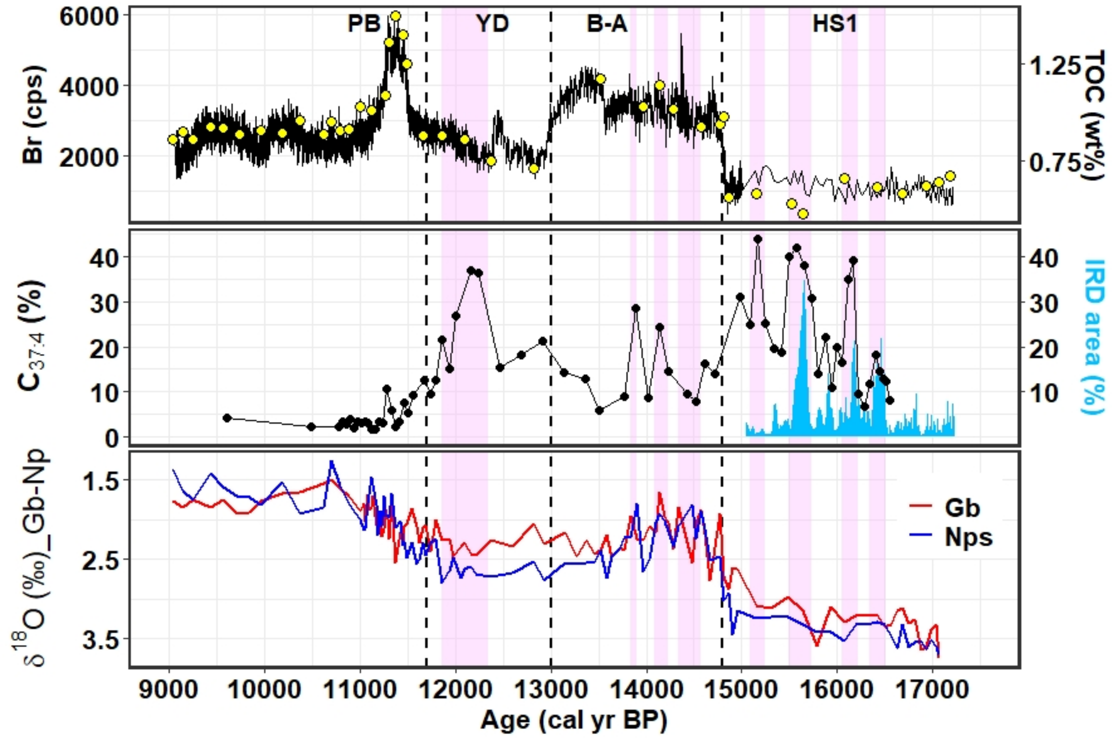

Figure 28. The ITRAX XRF core scanner calibrated high-resolution (thick line indicating 0.4 mm and the thin line indicating 1 cm resolution) Br count (cps), TOC (wt%, yellow color fill black circle), molecular biomarker alkenone ($C_{37:4}$ (%)), IRD (area%), and planktonic foraminifer (Gb = *G. bulloides* and Nps = *N. pachyderma* (sinistral)) $\delta^{18}O$ (‰) are plotted versus calibrated age (cal yr BP, x-axis). The plum color vertical shaded areas at 14.6–14.3, 14.2–14.1, and 13.9–13.8 cal ka BP indicating meltwater signature in the deglacial B-A period. At the top of the plot, the timing of major deglacial climate transitions demarked by HS1, B-A, and YD. The vertical black dashed line at 14.8, 13.0, and 11.7 cal ka BP indicating the transition points to change the XRF Br count.

An important indicator, K/Ti ratio, has emphasized the provenance differences of sediments (Diekmann et al., 2008). Richter et al. (2006) described K and Ti as dominantly linked to the average continental crust and basaltic sources. Hence, the K/Ti ratio, tracing the relative importance of both terrigenous sources (continental crust and basaltic). And, the high K/Ti ratio suggests high continentally derived materials. In core CL14PC, an increased supply of K was observed in both B-A and PB compares to HS1 and YD (**Figure 29**).

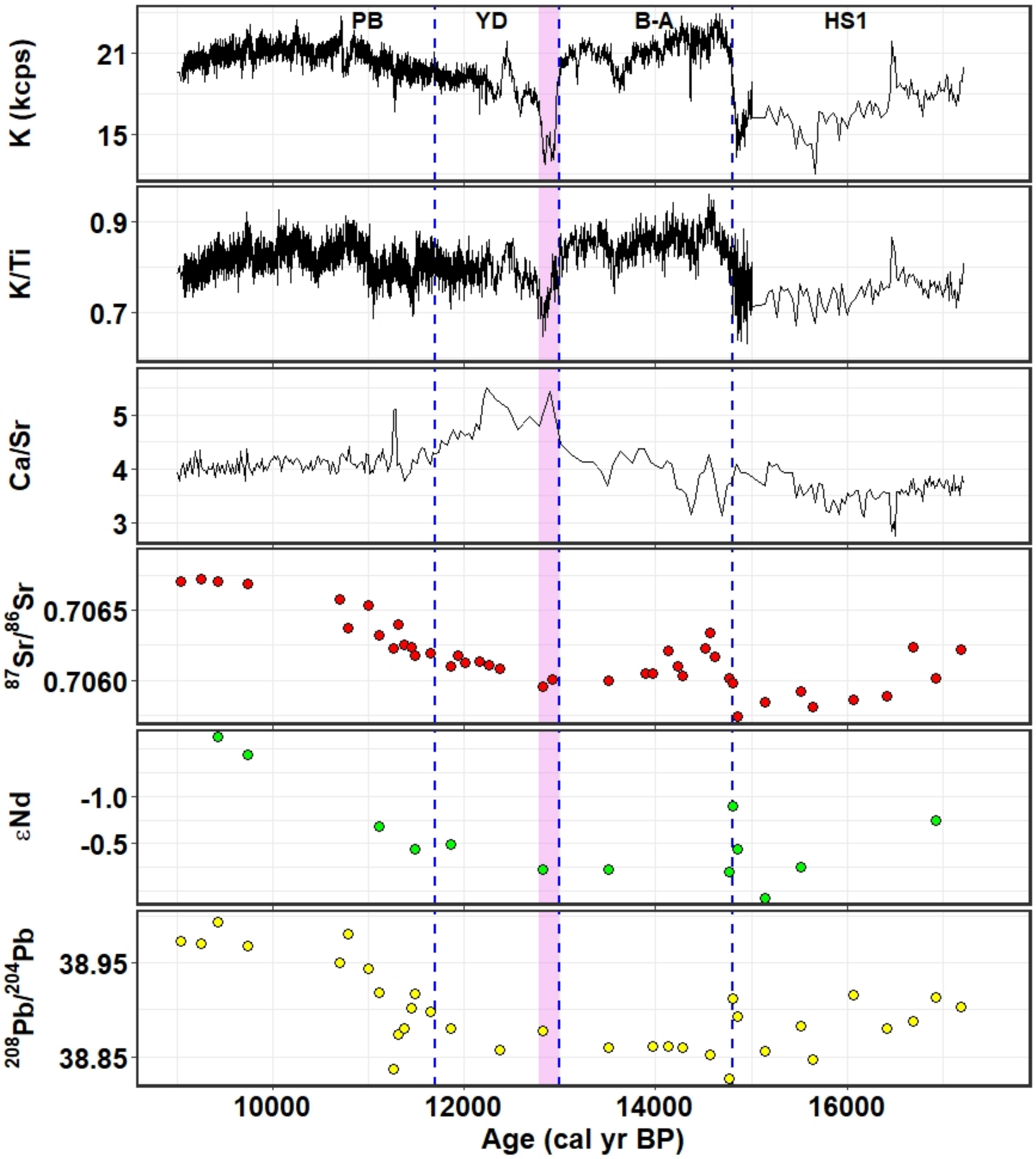

Figure 29. The K (kcps), K/Ti and Ca/Sr ratio, and the stable isotopic (^{87}Sr/^{86}Sr, εNd, and ^{208}Pb/^{204}Pb) composition of the core CL14PC are plotted versus age (cal yr BP, x-axis). For K and K/Ti ratio, the thick black line indicating 0.4 mm resolution, and the thin black line marking 1 cm resolution. The violet color shading at 13.0–12.8 cal ka BP indicating the high detrital carbonate content in the northern Gulf of Alaska continent. The vertical dash line (blue color) at 14.8, 13.0, and 11.7 marking the boundary of the timing of major deglacial climate transitions of HS1, B-A, YD, and PB intervals.

The high K/Ti ratio during B-A and PB interval confirms its supply from the continental region. Increased contribution of continentally derived materials as indicated with a high XRF K/Ti intensity ratio during the periods. The concomitant increase of $^{87}Sr/^{86}Sr$, εNd, and $^{208}Pb/^{204}Pb$ stable isotope ratios (**Figure 29**) during the B-A and PB period also supported the higher K/Ti ratio, thus suggesting lateral transport of terrigenous sediments. At the onset of the B-A, the $^{208}Pb/^{204}Pb$, $^{87}Sr/^{86}Sr$, and εNd isotopes ratio showed slight change toward radiogenic values; however, the variation was less-signification compared to HS1 values, suggesting an insignificant change in detrital sources.

Subsequently, YD was marked by distinct cooling and the regional glacial readvancement, and the decline of Br and TOC indicated low productivity (**Figures 26, 27**). The interval was characterized by reducing nutrients in the sub-surface layer. The majority of sea-ice and sea-ice-related diatom and subarctic silicoflagellate was assemblage indicating colder and less productive waters during the period (Barron et al., 2009). Low productivity resulted in less organic fluff at the seafloor in addition to enhanced oxygenation of Pacific Deepwater. A high C/N ratio indicating the considerable amount of terrestrially derived organic matter contains in the sediment during this interval. High $CaCO_3$ and Ca/Ti ratios show high carbonate content; however, previous studies (Addison et al., 2012) also found high $CaCO_3$ content during the period and did not explain the causes of high carbonate content. Therefore, explaining this concept is a new challenge and requires new datasets. In this study, in the early YD, ~13.0–12.8 cal ka BP, the K and K/Ti ratio sharply decreased, and the Ca/Sr ratio, Ca/Ti ratio, Ca, and $CaCO_3$ content sharply increased (**Figures 26, 29**). During this period, several short-term cooling events gave way (Menounos et al., 2017) to the regional glacial readvancement into the GOA (Davies et al., 2011). Local glacial readvancement derives high precipitation of $CaCO_3$ during this period. High detrital carbonate delivery with glacial readvancement and low K/Ti ratio indicates high basaltic detrital. Hodell et al. (2008) used the Ca/Sr ratio as a proxy for detecting detrital carbonate content in the Heinrich cold period, and high values indicated high detrital carbonate content. The high value of the Ca/Sr ratio during this period suggests that the high carbonate may come from detrital carbonate sources (**Figure 29**). The PC4 in the principal component analysis synchronized with the vicissitudes of the Ca/Sr ratio. Barron et al. (2009) and Tomokawa et al. (2019) indicating that the coastal marine diatom and silicoflagellates species were slightly abundant during the latter part of the YD period of the nearby sediment core EW0408-85JC and our core CL14PC, respectively. Thus, support the elevated peak of Ca/Sr, Ca/Ti, and $CaCO_3$ in the late YD (~12.24) (**Figures 26, 29**). Therefore, it can be concluded that the biogenic carbonate dominated the latter part of the YD, not in the earlier part. Barron et al. (2009) indicating that a subarctic silicoflagellate species *Distephanus octangulatus* (recent name *Stephanocha octangulata*) was common in the below 12.5 cal ka BP. However, the species had a minor contribution in the total silicoflagellate assemblages (~10%); moreover, Tomokawa et al. (2019) arguing that this species was a shift in the latter part of the YD in the core CL14PC (this study). Therefore, from the above discussion, we can conclude that the elevated carbonate peak contributed to the detrital carbonate content in the early YD. However, vigorous or healthy ventilation during this period (Praetorius et al., 2015) may also enhance the high preservation of $CaCO_3$ in the sediment (Okazaki et al., 2014).

During this period (YD), the $^{208}Pb/^{204}Pb$, $^{87}Sr/^{86}Sr$, and εNd stable isotopes ratio showed less significant change than late HS1 (**Figure 29**). Thus, suggesting that although the carbonate content and the sedimentary composition changed during the early YD, the provenance did not change.

As in the PB, the regional glacial readvancement during YD entailed retreating due to abrupt warming (Praetorius et al., 2015). A second prominent productivity peak near the end of YD was observed. At the onset of the PB, the coastal ice margin of the CIS was rapidly disappeared in response to abrupt warmth (Menounos et al., 2017), SST above 11°C (Praetorius et al., 2015), on average 4° to 5°C warmer relative to HS1 (Praetorius et al., 2020). The contributing XRF Br count in cluster 2 (C2, **Figures 21B, 22B**) showed high Br (3916 cps) and concomitant high TOC (1.18 wt%) contents during this (PB) transition (**Figures 24, 25**). Thus, have a good agreement with an increase in biogenic silica concentration and a return to hypoxic condition by laminations, low-oxygen benthic fauna, and an increase in authigenic Mo and U concentration in the nearby core EW0404-85JC (Addison et al., 2012; Praetorius et al., 2015). The XRF Br and TOC (wt%) exhibit peak productivity ~11.6–11.1 ka with an abruptly high peak at ~11.4 cal ka BP (ranging 11.0–11.9 cal ka BP within a 95% confidence interval) (**Figures 26, 27**) during the interval. The timing of this higher productivity pulse seems to correspond to the YD–Preboreal transition (11.653 ± 0.099 cal ka BP) as assigned by the NGRIP (Rasmussen et al., 2006) and the onset of meltwater pulse 1B (MWP-1B, 11.45–11.1 cal ka BP) as assigned by Barbados coral record (Abdul et al., 2016). This late interglacial (PB) productivity peaks were induced by the high SST and sea-level rise due to MWP-1B. The minor offset (0.05‰) between *G. bulloides* and *N. pachyderma* (sinistral)) $\delta^{18}O$ (‰) values suggesting high vertical mixing (Gebhardt et al., 2008) during this period. Vertical mixing and surface current spread the nutrient to the surface and sub-surface upper ocean, thus enhanced primary productivity. That leads to increased export of organic matter to the bottom, reduced the bottom oxygen as decomposition occurs, and forced the formation of sub-laminated sediment (Gebhardt et al., 2008; Barron et al., 2009; Addison et al., 2012; Praetorius et al., 2015). Comparatively lower values of the C/N ratio indicating that the sediment contains a larger amount of marine-based organic matter consistent with high PC3 values in the principal component analysis (**Figure 24**). Although at ~11.28 cal ka BP the Ca/Ti ratio and $CaCO_3$ showed a peak, the mean of Ca/Ti ratio and $CaCO_3$ content showed lower values than YD in the sediment. The reason may be as the opal-rich diatom species dominated this period. Besides, the bottom anoxic conditions may also suppress high $CaCO_3$ preservation and enhance $CaCO_3$ dissolution (Okazaki et al., 2014). Although, Ca/Sr and PC4 was indicator of detrital carbonate, however, a minor elevated peaks showed in Ca/Sr ratio and PC4 at ~11.28 cal ka BP responsible for the biogenic carbonate content as productivity proxy Br and TOC (this study), diatom, and silicoflagellate (Barron et al., 2009; Tomokawa et al., 2019) were also peak at that time. The PB period precisely dated in the region as 11.7–10.8 cal ka BP, coeval with similar studied in the region but little expansion due to the analytical uncertainty and/or uncertainty from age-depth model construction. The peak elevated productivity during the PB period occurred within the sub-lamina interval, similar to the biogenic opal-based paleoproductivity peak within the sub-lamina interval in the previous studies (Addison et al., 2012) with age model uncertainty.

Davies et al. (2011) hypothesized that the elevated productivity episodes during B-A and in the early Holocene were caused by an increased influx of the micronutrient iron (Fe) from surrounding continental shelves previously deposited and increased supply due to the deglacial sea-level rise. Lam et al. (2013) suggested that no evidence for an abrupt deglacial pulse of iron from any source at the time of peak productivity. This study found high XRF Fe during B-A and PB periods compared to HS1 and YD. During B-A, the glacial meltwater and suspended sediment deliver terrestrially derived nutrients (Fe, P, Si) to the coastal ocean as solutes, colloids, and particulates (Hood & Scott, 2008; Schroth et al., 2011; Gerringa et al., 2012). The coastal region act as a depocenter (Davies et al., 2011), where abundant terrigenous and Fe load deposited (Feely et al., 1979; Sholkovitz et al., 2009; Schroth et al., 2011; Crusius et al., 2011; Ito, 2011; Aguilar-Islas et al., 2016). These loads undergo different physical, chemical, and biological processes (Feely et al., 1979), resuspension of fine particulate sediment, repetitive oxidation-reduction, and the reduction of iron isotope produce an isotopically light iron pool that is transferred to the water column and make it accessible for surface biota

(Johnson et al., 2001; Severmann et al., 2010). Besides, the abrupt sea-level rise inundated the coastal depocenters (Addison et al., 2012) and increased Fe supply through remobilization.

4.5. Conclusion

The high-resolution multiproxy records from core CL14PC and CL14MC investigated in this study established a regional paleoproductivity and sedimentary framework. That helps us to understand the productivity fluctuations along the continental margin of the northeastern Gulf of Alaska. From the study, we can make the following conclusion:

- The CIR calibrated XRF CS data were used for multivariate cluster and principal component analysis. The multivariate cluster analysis (K-means) showed that the data was distributed in five formats (cluster). According to paleoclimate events, clusters 1 (C1, Heinrich stadial 1) and 2 consists of the last deglacial XRF core scanner datasets. Cluster 2 (C2) again consists of deglacial B-A, YD, and PB datasets. The principal component analysis showed that the first principal component (PC1) is responsible for 48.4% variation in the high-resolution XRF CS dataset, and Fe, Mn, and Sr are the main variables for this variance. The third principal component (PC3) contributed 13.7% variation, and Br and Ca are the main contributor to this variation. According to the multivariate principal component analysis of the high-resolution XRF CS dataset, this finding concluded that PC3 represents a marine-based productivity proxy, and PC4 represents the detrital carbonate content intervals.

- The finding indicates that the XRF Br counts robustly reflect the deglacial productivity changes in the northeastern Gulf of Alaska continental margin and argues that this might be rarely considered in the region. We observed two peak productivity periods in the core CL14PC at 14.8–13.0 cal ka BP and 11.6–11.0 cal ka BP marked by elevated Br and TOC-rich laminated sediments, correspond to the regional expressions of B-A and PB, respectively. In PC3, these fluctuations are exhibited. However, we argue that the Br records can be an ideal record for evaluating the fluctuation of marine paleoproductivity in the GOA region during the last deglacial period.

- The ^{208}Pb/^{204}Pb isotopic compositing exhibits similar values of the Orca group's deep-sea fan sediments and the Cordova area's Pluton rocks ^{208}Pb/^{204}Pb stable isotope ratios, which are the proximal offshore source like ^{87}Sr/^{86}Sr and ε_{Nd} isotopic ratio. In the early Younger Dryas (~13–12.8 cal ka BP), the concomitant elevated peaks exhibited in the Ca/Sr ratio and in the PC4 in multivariate principal component analysis, indicating high detrital carbonate content existed during the period. The proxy K/Ti ratio suggested that the sediment may contain more basaltic detrital during this period. The Sr, Nd, and Pb isotopic composition did not show provenance change during the period.

Chapter 5: Summary and conclusion

This dissertation's studies examine the high-resolution multiproxy records relating to paleoceanographic reconstruction during the last deglaciation. The period (last deglaciation) encompasses the dynamic transition between the last glacial (last glacial maximum) to the interglacial period of the modern-day. That, characterized by overall planetary warming of several degrees with cold and warm climate oscillations. The multiproxy consisting of large datasets from X-ray fluorescence, geochemical and isotopic records from core KH17-3 CL14PC/MC is then used: to calibration of initial XRF data for increasing reliability of using high-resolution multi-elemental proxy records for further application in paleoceanographic studies, to constrain the timing and potential sources of meltwater discharge associated with the CIS retreat during the last deglaciation, to assess the large datasets through a multivariate approach to extract their latent factors and information, and assess the paleoproductivity based on high-resolution new productivity tracer and their relation with meltwater injection from the decay of the CIS.

In paleoceanographic studies, the rapid acquisition of high-resolution multi-elemental counts data obtained by X-ray fluorescence core scanner is very useful. Still, the appropriate interpretation of the data requires calibration because several factors affect multi-element counts during measurement. In this study (chapter 2), the linear regression between the initial XRF core scanner results with WD-XRF measured concentration showed moderate to a high agreement (correlation) for heavier elements and weaker correlation for lighter elements, especially K and Ti. Therefore, the high-resolution raw data from the ITRAX XRF core scanner were tested in multiple calibration methods to determine the best way to normalize the data that provides the highest accuracy from the initial raw data. Among the normalization (calibration) methods, the coherent/incoherent X-ray scatter ratio (CIR) showed the best performance. Furthermore, the correlation measured through linear regression of Pearson's method and Kendall's tau (τ) method substantially increased in the CIR calibration method than initial correlation. Therefore, based on the evaluation of this study, it can conclude that normalization of ITRAX XRF CS initial data by coherent to incoherent X-ray scatter ratio (i.e., element count/CIR) is a suitable method for marine-based wet sediment.

The multiproxy records from $\%C_{37:4}$ alkenones, planktonic foraminifer $\delta^{18}O$, ice-rafted debris, and detrital Sr-Nd isotope datasets reconstruct meltwater injection events from the decay of the Cordilleran Ice Sheet during the last deglaciation in this study (chapter 3). The study provides new evidence of multiple stages of the collapse of the northern marine-terminating CIS margins linked to lower sea-surface salinity and IRD deposition. During HS1 at ~16.4, ~16.2, and ~15.6 ka, the peaks %$C_{37:4}$ alkenones content (18%, 39%, and 42%, respectively) are concurrent with higher IRD deposition, suggesting that surface freshening was associated with the melting of icebergs. Furthermore, Sr-Nd isotopes indicated that the sediment source was proximal to the core site. That indicates that meltwater injection during HS1 was associated with the large-scale collapse of the marine-terminating CIS margins in the northern GOA. In early B-A, anomalously high values of %$C_{37:4}$ alkenones at ~14.1 (24%) and ~13.9 (29%) ka indicate distinctly lower salinity conditions are associated with two notable δ^{18}O-depleted peaks at 14.2–14.1 and 13.9–13.8 ka. Besides, at 14.6–14.3 ka, the depleted planktonic foraminifer δ^{18}O and δ^{13}C signals show a meltwater signature, but this was not sufficient in volume to sustain lower salinity conditions throughout the year, especially in summer. This evidence constrains the timing of multiple meltwater injections during 14.6–13.8 ka that lasted ~800 years. In the middle YD at ~12.2 ka, the extremely high %$C_{37:4}$ alkenones (37%) also suggesting meltwater signature. However, the integrated evidence from %$C_{37:4}$ alkenones, ice-rafted debris, planktonic foraminifera- and bulk sediment-stable isotopic records indicate that melting of the northern parts of the CIS injected a large amount of freshwater into the northeaster GOA, following a substantial mass loss of CIS during HS1 and in early B-A to middle YD. Importantly, argue that sources of the deglacial meltwater are likely proximal to the core site, and multiple CIS meltwater injection in the northeast Pacific was temporally disaggregated during 14.6–12.2 ka. However, their impact on the freshwater budget in the northeastern Pacific during the abrupt global sea-level rise (14.6–14.3) was relatively small.

This study (chapter 4) used the CIR calibrated (i.e., element count/CIR) XRF CS data for multivariate cluster and principal component analysis. The multivariate cluster analysis (K-means) showed that the data was distributed in five cluster formats. Among the cluster, clusters 1 and 2 consists of the last deglacial (HS1–PB) high-resolution XRF multi-element datasets. According to the multivariate principal component analysis of the high-resolution XRF CS dataset, the findings of this study (chapter 4) concluded that PC3 and PC4 represent the marine-based productivity proxy and the detrital carbonate content variation, respectively, during the last deglacial paleoclimate events. The deglacial cluster (C2) showed two peaks elevated productivity periods in the core CL14PC. At 14.8–13.0 cal ka BP and 11.6–11.1 cal ka BP the peaks productivity marked by elevated Br and TOC-rich laminated sediments correspond to the regional expressions of B-A and PB, respectively, during the last deglacial period. In PC3, these fluctuations are exhibited. The elevated productivity episodes are coeval with the lamina and sub-lamina interval during the last deglaciation. That is similar to the low-resolution biogenic opal-based paleoproductivity records in the previous studies. The high productivity during inferred multiple meltwater periods in the B-A did not tightly coincide. During these warming intervals (B-A and PB), the vertical mixing between the surface and sub-surface layers might have the crucial modulator for high productivity. That is consistent with a minor offset of δ^{18}O records between surface and sub-surface dwelling *G. bulloides* and *N. pachyderma* (sinistral) species, respectively. The finding indicating that the high-resolution XRF Br counts robustly reflect the deglacial productivity changes in the northeastern Gulf of Alaska continental margin that might yet rarely be considered in the region. During the B-A and PB period, the continentally derived materials increase (high K/Ti ratio), and in the early Younger Dryas (~13–12.8 cal ka BP), the concomitant increase of Ca/Sr ratio and PC4 indicating that elevated detrital carbonate content exists in the sediment composition. Furthermore, the proxy K/Ti ratio suggested that this high detrital carbonate may be derived from a basaltic detrital source. The similar values of ^{208}Pb/^{204}Pb isotopic composition found in the proximal Orca group's deep-sea fan sediments and the Cordova area's Pluton rocks ^{208}Pb/^{204}Pb stable isotopic composition, like ^{87}Sr/^{86}Sr and ε_{Nd} isotopic ratio. The insignificant change of Pb, Sr, and Nd isotopic composition from HS1 to YD and the close similarity to the offshore sediment Pb, Sr, and Nd isotopic values suggesting that during the last deglaciation, the sediment derived from the proximal sources as with glacial meltwater. The finding of this study also indicates high fertilization with Fe during the high productivity episodes in the Bølling-Allerød and Preboreal period, a previous controversial hypothesis (Davies et al., 2011; Lam et al., 2013).

Appendix A. Experimental

A.1. Chemicals and Materials

Some of the chemicals and materials used in the study are listed here. However, their names and uses are discussed in the relevant study (chapter 2–4).

- **Spectro Blend:** Spectro Blend (Cat# 3399N064, Spectro Blend CH660) is a pelletization powder binder contain C, O, H, and N ($C_{19}H_{38}ON$). It is used in this study to make pressed pellets for the Wavelength Dispersive-XRF core scanner quantitative measurement because homogenized power sample difficult to formed pellets without mixing binder.

- **Sodium Acetate Anhydrous** (fisher scientific, assay percent range ≥99.0%): Molecular formula $C_2H_3NaO_2$ (CH_3COONa), molecular weight 82.034 (g/mol), melting point 324 °C.

- **Acetic Acid** (fisher scientific, percent purity ≥99.7%): Molecular formula $C_2H_4O_2$ (CH_3COOH), molecular weight 60.052 (g/mol), boiling point 118 °C.

- **Hydroxylamine hydrochloride** (Sigma-Aldrich, assay percent 99.999%): Molecular formula $NH_2OH.HCl$ (Hydroxylammonium chloride), molecular weight 69.49 (g/mol). Melting point 155–157 °C.

- **Sodium hydroxide:** Chemical formula NaOH, molecular weight 39.9971 (g/mol), melting point 323 °C (613 °F).

- **Nitric Acid:** Chemical formula HNO_3, molecular weight 63.012 (g/mol), boiling point 83 °C (181 °F). Product used in this study from TAMAPURE (assay 68.0 ± 1.0 wt%, TAMAPURE-AA-100, Tama Chemical, Co., Ltd., Tokyo, Japan) and KANTO (assay 69%, KANTO Ultrapure-100 Nitric Acid, Kanto Chemical Co., Inc. Japan).

- **Hydrochloric acid:** Chemical formula HCl, molecular weight 36.458 (g/mol), boiling point 61 °C (for concentration 36%). Product used in this study from KANTO (KANTO Ultrapure Hydrochloric Acid, Kanto Chemical Co., Inc. Japan).

- **Hydrofluoric acid:** Chemical formula HF, molar mass 20.0 (g/mol), boiling point 19.5 °C. Product used in this study from TAMAPURE-AA-100 (Tama Chemical, Co., Ltd., Tokyo, Japan).

- **Perchloric acid:** Chemical formula $HClO_4$, molar mass 100.46 (g/mol), boiling point 203 °C (397 °F). Product used in this study from TAMAPURE-AA-100 (Tama Chemical, Co., Ltd., Tokyo, Japan).

- **Certified Reference Materials (CRMs):** CRMs from Geological Survey of Japan (GSJ)- JA-1, JA-3, JB-1a, JB-2, JB-3, JF-1, JG-3, JG-1, JP-1, JR-1, JLK-1, and JSd-2, and National Research Council Canada (NRCC)- MESS-4.

Standard:

- **Sulfanilamide** (Molecular formula- $C_6H_8N_2O_2S$), IUPAC name- 4-aminobenzenesulfonamide, synonyms- Sulphanilamide, Sulfamine. Melting point- 165 °C (329 °F). Chemically, Sulfanilamide is an organic compound consisting of an aniline derivatized with a sulfonamide group. This standard was used in this study during the elemental analysis of total organic carbon, total carbon, and total nitrogen.

- **NMJI CRM 3681-a (Pb standard)-** from National Metrology Institute of Japan (NMIJ). This standard was used during Pb stable isotopic measurement.

- **JNdi-1:** JNdi-1 is an international standard for Neodymium (Nd). This standard was used during the measurement of Nd isotopic composition.

- **NBS 987:** NBS 987 is the standard reference material for Strontium Carbonate Isotopic Standard. This standard was used during Strontium (Sr) isotopic composition measurement.

A.2. Methods

A.2.1. X-ray fluorescence multi-elements count

The multi-elemental count of different elements was measured through the ITRAX X-ray fluorescence core scanner. The description of the ITRAX core scanner and detailed procedure for element intensity measurement is described in chapter 2.

A.2.2. Element concentration measurement

The element concentration was measured using Rigaku Supermini 200 spectroscope and Vario EL cube CHNOS elemental analyzer. The Wavelength Dispersive X-ray Fluorescence Rigaku Supermini 200 spectroscope measured Sr, Fe, Mn, Ti, Ca, and K concentration through the Empirical Calibration (EC) method. Briquette method (Takahashi, 2015) was used for the preparation of the sample for concentration measurement. The detailed procedure for concentration measurement (EC method) is described in chapter 2 of this study and for further information, see the product web page:

(https://www.rigaku.com/products/wdxrf/supermini200).

The total organic carbon, total carbon, and total nitrogen concentration were measured using an elemental analyzer (Vario EL cube CHNOS). The procedure for measurement and sample preparation describes in chapter 2 and 4.

A.2.3. Leaching and digestion of bulk sediments

The bulk samples were sequentially leached for Pb, Sr, and Nd isotopic composition measurements from the bulk sediments. The brief procedure as approximately 1.0 g of a dry bulk sediment sample from the core KH17-3 CL14PC sequentially leached to remove the silica fractions, carbonate, and Fe-Mn oxide coatings (Bayon et al., 2002; Piotrowski et al., 2004; Horikawa et al., 2011; Kozaka et al., 2018). To remove the carbonate (decarbonization) the sediment samples were dissolved with 1.5 M buffered acetic acid (AA) for about 4 hours at a hot water bath (~85 °C). Next, the samples were rinsed with ultrapure water (18.2 MΩ·cm) three times. Then, the Fe-Mn oxide fraction was leached using 0.05 M hydroxylamine hydrochloride (HH) in 25% acetic acid for about 4 hours in the hot water bath (~85 °C). By adding ultrapure water, the samples were rinsed three times. For removing the biogenic silica fraction, the samples were leached with 1 M NaOH solution for 30 minutes in the hot water bath (~85 °C) and then rinsed with ultrapure water three times.

The residue samples were then oven-dried at 50 °C. From the dried samples, ~40 mg was weighted and entirely digested by an admixture of 0.5 mL of concentrated HNO_3 (TAMAPURE-AA-100) and 0.5 mL of concentrated $HClO_4$ (TAMAPURE-AA-100) by refluxing with PFA Teflon (Savillex®) vial for more than 24 hours at 130 °C. After cooling, add 0.5 mL of concentrated HF (TAMAPURE-AA-100) and thoroughly digest the sample at 140 °C for more than six h on a hot plate (DigiPrep Jr) in a cleanroom.

A.2.4. Stable isotope measurement

The planktonic foraminifer (*Globigerina bulloides* and *Neogloboquadrina pachyderma* (sinistral)), carbon ($\delta^{13}C$), and oxygen ($\delta^{18}O$) stable isotopes were measured using Thermo-Finnigan MAT-253 mass spectrometer with a carbonate preparation device. The radiocarbon isotope (^{14}C) was measured using Accelerator Mass Spectrometer (AMS), the procedure described in chapter 3. The Pb ($^{208}Pb/^{204}Pb$, $^{207}Pb/^{204}Pb$, $^{206}Pb/^{204}Pb$) and Sr ($^{87}Sr/^{86}Sr$) stable isotopic composition was measured by using multi-collector inductively coupled plasma mass spectrometer (MC-ICP-MS) NEPTUNE (Thermo Fisher Scientific), the procedure described in chapter 3 and 4 sections. The Nd ($^{143}Nd/^{144}Nd$) stable isotopes were measured through thermal ionization mass spectrometer (TIMS) TRITON, the description found in chapter 3.

A.2.5. Molecular biomarker measurement

The molecular biomarker of tetraunsaturated C_{37} methyl ketones (alkenone- a percentage of the relative abundance of $C_{37:4}$ (%$C_{37:4}$) to the total abundance of $C_{37:2}$, $C_{37:3}$, and $C_{37:4}$) was measured by using a SpeedExtractor (E-916, BUCHI) and HP6890 gas chromatograph (GC), the procedure described in chapter 3.

Appendix B

Table B1. The accelerator mass spectrometry (AMS) planktonic foraminifera ^{14}C dates from the core CL14PC/MC (KH17-3-CL14PC/MC) and the calibrated calendar ages ('rbacon' Blaauw and Christen, 2011). The local reservoir age correction $\Delta R = 470 \pm 80$ years (McNeely et al., 2006) was applied for calibration of calendar ages in Marine13 (Reimer et al., 2013) and recalculated $\Delta R = 301 \pm 60$ years (McNeely et al., 2006) was applied for calibration of calendar ages in Marine20 (Heaton et al., 2020; Reimer et al., 2020). The age-depth model was constructed using the R script name {*rbacon*} of the 2.3.9.1 package for Marine13 and the 2.4.3 package for Marine20.

Core	**Core depth (cm)**	**Planktonic foraminifer ^{14}C age (years BP)**	**Planktonic foraminifer ^{14}C age error (± years BP)**	**Marine13 calibrated age (cal yr BP)**	**Marine20 calibrated age (cal yr BP)**	**Lab code**
Multiple	13.5	260[a]	60			OS-144767
Piston	88.0	1560	40	740	761	OS-144765
Piston	292.4	4240	65	3775	3819	OS-144766
Piston	451.9	6690[b]	25	6698	6692	OS-144531
Piston	521.7	8360	30	8284	8264	OS-139041
Piston	632.7	9570	40	9930	9967	OS-139042
Piston	705.1	10700	40	11412	11513	OS-139149
Piston	726.4	11050	45	12091	12193	OS-144532
Piston	741.2	12600	35	13486	13603	OS-139106
Piston	765.4	13500	50	14862	14946	OS-144533
Piston	783.7	14000	55	15636	15603	OS-144590
Piston	809.5	14650	55	16420	16279	OS-144591
Piston	845.7	15000	40	16975	16788	OS-139107
Piston	868.5	14750	60	17232	17052	OS-144592

[a] The data was not used to calibrate calendar age due to being out of the calibration range.

[b] Mollusca shells.

Table B2. The planktonic foraminifer *Globigerina bulloides* (Gb) and *Neogloboquaderin pachyderma* (sinistral) (Nps) $\delta^{13}C$ (‰ VPDB) and $\delta^{18}O$ (‰ VPDB) data from 9.0 to 17.2 ka of the core CL14PC/MC (KH17-3-CL14PC/MC) in this study.

Composite Depth (cm bsf)	**Age (cal yr BP)**	**$\delta^{13}C$ (‰) Gb**	**± SD Gb**	**$\delta^{18}O$ (‰) Gb**	**± SD Gb**	**$\delta^{13}C$ (‰) Nps**	**± SD Nps**	**$\delta^{18}O$ (‰) Nps**	**± SD Nps**
572	9038	0.00	0.04	1.78	0.02	0.38	0.02	1.37	0.02
579	9139	-0.15	0.04	1.86	0.03	0.48	0.03	1.64	0.02
587	9254	-0.20	0.01	1.76	0.02	0.48	0.03	1.75	0.03
599	9430	-0.33	0.02	1.85	0.01	0.40	0.04	1.42	0.02
608	9564	-0.30	0.02	1.75	0.02	0.38	0.04	1.59	0.02
618	9708	-0.32	0.07	1.93	0.03	0.30	0.02	1.71	0.04
627	9840	-0.19	0.02	1.91	0.03	0.41	0.04	1.72	0.03
634	9957	-0.14	0.09	1.77	0.02	0.28	0.01	1.81	0.03
646	10189	-0.42	0.02	1.67	0.02	0.36	0.02	1.53	0.03
655	10372	-0.30	0.01	1.65	0.03	0.28	0.02	1.93	0.02
667	10619	-0.13	0.06	1.55	0.03	0.31	0.03	1.86	0.02
671	10702	-0.65	0.02	1.49	0.02	0.07	0.01	1.27	0.04
675	10784	-0.34	0.01	1.61	0.02	0.10	0.02	1.57	0.03
680	10884	-0.50	0.02	1.70	0.04	0.31	0.00	1.80	0.03
686	10999	-0.20	0.01	1.90	0.02	0.34	0.03	2.00	0.01
687	11038	-0.20	0.04	1.80	0.02	0.51	0.02	2.13	0.05
688	11056	-0.29	0.01	2.02	0.02	0.26	0.07	2.12	0.04
689	11076	-0.20	0.02	1.70	0.01	0.45	0.02	1.80	0.03
690	11094	-0.30	0.01	1.88	0.02	0.35	0.01	1.69	0.03
691	11115	-0.05	0.01	1.85	0.02	0.39	0.02	1.47	0.03
692	11133	-0.21	0.02	1.70	0.03	0.63	0.02	1.57	0.02
693	11153	-0.28	0.01	1.95	0.02	0.34	0.03	1.74	0.03
694	11171	-0.40	0.01	2.06	0.02	0.34	0.02	1.82	0.02
695	11191	-0.32	0.01	1.95	0.03	0.38	0.02	2.20	0.04
696	11209	-0.07	0.03	2.07	0.03	0.35	0.03	1.89	0.02
697	11230	-0.01	0.02	2.21	0.04	0.44	0.02	2.08	0.03
698	11248	0.12	0.02	2.11	0.02	0.40	0.03	1.71	0.02
699	11268	0.01	0.01	1.87	0.03	0.33	0.06	1.96	0.03
700	11286	0.12	0.02	1.98	0.02	0.48	0.02	1.95	0.03
701	11309	0.18	0.01	2.24	0.03	0.44	0.03	1.97	0.04
702	11331	-0.13	0.04	1.78	0.07	0.44	0.02	1.67	0.03
704	11376	0.06	0.02	2.55	0.03	0.27	0.03	2.10	0.03
706	11421	-0.03	0.02	2.17	0.04	0.56	0.02	2.02	0.03
706	11445	0.23	0.03	2.31	0.02	0.53	0.03	2.32	0.03
707	11467	0.05	0.01	2.09	0.02	0.47	0.03	2.28	0.01

708	11490	0.10	0.02	2.05	0.02	0.47	0.02	2.49	0.03
710	11538	0.07	0.02	1.86	0.04	0.53	0.02	2.28	0.02
712	11596	0.06	0.04	2.08	0.02	0.47	0.02	2.56	0.04
713	11623	0.11	0.03	2.29	0.02	0.51	0.03	2.49	0.04
714	11654	-0.08	0.03	2.10	0.02	0.46	0.01	2.29	0.02
715	11682	0.05	0.01	2.07	0.03	0.65	0.01	2.44	0.02
717	11740	0.06	0.01	2.40	0.03	0.61	0.01	2.30	0.03
719	11798	-0.14	0.02	2.01	0.03	0.53	0.01	2.25	0.03
721	11863	0.04	0.03	2.26	0.03	0.62	0.07	2.80	0.02
723	11939	0.03	0.02	2.24	0.02	0.53	0.03	2.64	0.04
724	11979	0.12	0.01	2.46	0.03	0.64	0.02	2.48	0.03
725	12055	-0.01	0.02	2.34	0.02	0.58	0.03	2.73	0.03
726	12091	-0.03	0.03	2.30	0.04	0.51	0.02	2.63	0.02
728	12167	-0.14	0.02	2.44	0.04	0.41	0.02	2.59	0.04
729	12207	0.00	0.02	2.45	0.02	0.51	0.01	2.68	0.03
731	12376	-0.17	0.02	2.26	0.04	0.33	0.01	2.72	0.02
733	12598	-0.19	0.02	2.34	0.03	0.43	0.04	2.67	0.03
735	12820	-0.06	0.01	2.05	0.03	0.43	0.02	2.53	0.01
736	12925	-0.35	0.02	2.31	0.03	0.51	0.01	2.76	0.02
738	13147	-0.30	0.01	2.17	0.02	0.44	0.01	2.54	0.03
739	13264	-0.10	0.02	2.46	0.03	0.30	0.01	2.57	0.03
740	13370	-0.15	0.02	2.26	0.02	0.28	0.02	2.55	0.03
741	13452	-0.24	0.01	2.43	0.02	0.24	0.04	2.55	0.04
742	13513	-0.03	0.01	2.38	0.01	0.14	0.02	2.39	0.02
743	13581	-0.09	0.02	2.20	0.04	0.21	0.02	2.74	0.02
744	13642	-0.20	0.01	2.49	0.03	0.22	0.01	2.47	0.01
744	13710	-0.35	0.03	2.36	0.01	0.16	0.01	2.37	0.03
745	13771	-0.40	0.02	2.39	0.03	0.21	0.02	2.24	0.02
746	13838	-0.41	0.02	1.97	0.01	0.19	0.01	2.22	0.02
747	13899	-0.20	0.02	2.25	0.03	0.21	0.01	1.81	0.04
748	13967	0.01	0.03	2.26	0.05	0.22	0.03	2.66	0.02
749	14028	-0.24	0.01	2.08	0.02	0.21	0.05	2.50	0.04
750	14092	-0.28	0.02	2.17	0.03	0.13	0.02	2.03	0.03
751	14138	-0.56	0.04	1.65	0.04	0.13	0.02	1.93	0.03
752	14188	-0.47	0.01	1.97	0.01	0.01	0.02	2.03	0.04
753	14233	-0.33	0.02	2.04	0.02	0.11	0.02	2.15	0.02
754	14284	-0.14	0.01	2.36	0.04	0.39	0.02	2.35	0.03
755	14329	-0.34	0.04	1.84	0.02	0.25	0.02	2.08	0.02
758	14475	-0.32	0.02	2.54	0.03	0.42	0.02	1.81	0.04
759	14520	-0.17	0.01	2.06	0.03	-0.10	0.04	2.25	0.03
760	14570	-0.32	0.04	1.88	0.03	-0.01	0.04	1.90	0.02
761	14616	-0.15	0.01	2.18	0.01	-0.18	0.03	2.12	0.03
762	14667	-0.12	0.03	2.76	0.04	0.39	0.02	2.51	0.04

763	14765	-0.18	0.02	1.93	0.02	-0.10	0.02	2.46	0.01
764	14811	0.06	0.02	2.71	0.01	0.19	0.04	3.03	0.03
765	14862	-0.12	0.02	2.87	0.03	0.21	0.01	2.92	0.03
766	14908	-0.01	0.02	2.60	0.02	0.27	0.03	3.44	0.03
767	14959	-0.02	0.02	2.63	0.02	0.12	0.02	3.14	0.02
771	15149	-0.30	0.02	3.08	0.02	0.06	0.02	3.24	0.02
775	15314	-0.27	0.02	3.11	0.01	-0.04	0.01	3.23	0.04
780	15483	0.00	0.02	2.97	0.02	0.13	0.02	3.23	0.04
784	15636	-0.65	0.02	3.14	0.01	-0.01	0.01	3.32	0.01
788	15789	-0.38	0.03	3.59	0.03	0.28	0.02	3.42	0.01
792	15927	-0.30	0.04	3.10	0.03	0.21	0.01	3.42	0.01
797	16071	-0.63	0.02	3.28	0.02	-0.03	0.01	3.53	0.02
801	16190	-0.47	0.02	3.21	0.02	0.27	0.01	3.32	0.03
805	16305	-0.56	0.03	3.21	0.04	0.04	0.02	3.32	0.03
810	16420	-0.46	0.02	3.20	0.03	-0.21	0.02	3.29	0.04
814	16494	-0.53	0.01	3.36	0.02	0.07	0.02	3.31	0.02
818	16560	-0.43	0.01	3.31	0.01	0.06	0.01	3.46	0.01
822	16625	-0.63	0.03	3.14	0.04	0.13	0.01	3.63	0.02
826	16686	-0.70	0.03	3.12	0.02	-0.26	0.03	3.31	0.02
830	16747	-0.76	0.03	3.31	0.03	0.00	0.02	3.60	0.02
834	16811	-0.44	0.03	3.26	0.03	0.07	0.01	3.54	0.02
838	16873	-0.59	0.02	3.64	0.02	0.06	0.01	3.52	0.02
843	16932	-0.50	0.01	3.60	0.02	-0.03	0.01	3.64	0.02
847	16990	-0.77	0.02	3.38	0.04	-0.02	0.02	3.51	0.02
850	17032	-0.72	0.03	3.32	0.03	0.05	0.02	3.60	0.02
853	17066	-0.74	0.03	3.75	0.01	0.04	0.02	3.70	0.02

Table B3. The isotopic composition of Strontium ($^{87}Sr/^{86}Sr$) was determined from the bulk sediment sample of the core CL14PC/MC (KH17-3-CL14PC/MC) in this study. The data reported here from 9.0 to 17.2 ka.

Composite Depth (cmbsf)	Age (cal yr BP)	$^{87}Sr/^{86}Sr$	± 2σ (SE)
572.21	9038	0.706705408	0.000010
587.20	9254	0.706718048	0.000010
599.20	9430	0.70670797	0.000012
620.20	9737	0.706686631	0.000011
671.20	10702	0.706580723	0.000012
675.13	10784	0.706374075	0.000014
685.58	10999	0.706531453	0.000011
691.28	11115	0.70631896	0.000014
698.88	11268	0.706231109	0.000011
700.78	11309	0.706400025	0.000012
703.63	11376	0.706251232	0.000009
706.48	11445	0.706235827	0.000012
708.38	11490	0.706179512	0.000007
714.08	11654	0.706197562	0.000008
720.73	11863	0.706102932	0.000010
722.63	11939	0.706173541	0.000008
724.53	12015	0.706122072	0.000008
728.33	12167	0.706133912	0.000010
730.23	12259	0.706104462	0.000008
731.18	12376	0.706082526	0.000010
734.98	12820	0.705958276	0.000010
735.93	12925	0.706006604	0.000006
741.63	13513	0.705999708	0.000013
747.33	13899	0.70604599	0.000008
748.28	13967	0.706050366	0.000009
751.13	14138	0.706211303	0.000010
753.03	14233	0.706103578	0.000007
753.98	14284	0.706034957	0.000010
758.73	14520	0.706226593	0.000008

759.68	14570	0.70634159	0.000011
760.63	14616	0.706170825	0.000009
763.48	14765	0.706010848	0.000011
764.43	14811	0.705979739	0.000012
765.38	14862	0.705739733	0.000013
771.29	15149	0.705846934	0.000011
780.59	15521	0.705919936	0.000012
783.69	15636	0.705809964	0.000014
797.14	16071	0.705862802	0.000015
809.54	16420	0.705887145	0.000011
826.09	16686	0.706237202	0.000011
842.63	16932	0.706014591	0.000009
864.35	17187	0.706217318	0.000015

Table B4. The Neodymium (^{143}Nd/^{144}Nd) isotopic composition from 9.0 to 17.2 ka was determined from a bulk sediment sample of the core CL14PC/MC (KH17-3-CL14PC/MC) in this study.

Composite Depth (cmbsf)	**Age (cal yr BP)**	**^{143}Nd/^{144}Nd**	**ε_{Nd}**	**± 2σ (SE)**
599	9430	0.51255	-1.62	0.13
620	9737	0.51256	-1.44	0.11
691	11115	0.51260	-0.69	0.11
708	11490	0.51262	-0.44	0.13
721	11863	0.51261	-0.50	0.15
735	12820	0.51263	-0.22	0.14
742	13513	0.51263	-0.23	0.12
763	14765	0.51263	-0.20	0.11
764	14811	0.51259	-0.89	0.12
765	14862	0.51262	-0.44	0.13
771	15149	0.51264	0.07	0.13
781	15521	0.51263	-0.25	0.14
843	16932	0.51260	-0.74	0.15

Table B5. The bulk sediment sample Lead ($^{208}Pb/^{204}Pb$) isotopic composition of the core CL14PC/MC (KH17-3-CL14PC/MC) in this study was reported from 9.0 to 17.2 ka.

Composite Depth (cmbsf)	**Age (cal yr BP)**	**$^{208}Pb/^{204}Pb$**	**± 2σ (SE)**
572	9038	38.9734	0.0012
587	9254	38.9700	0.0014
599	9430	38.9939	0.0014
620	9737	38.9682	0.0015
671	10702	38.9503	0.0011
675	10784	38.9810	0.0010
686	10999	38.9434	0.0010
691	11115	38.9178	0.0015
699	11268	38.8367	0.0009
701	11309	38.8732	0.0013
704	11376	38.8797	0.0013
706	11445	38.9016	0.0011
708	11490	38.9169	0.0013
714	11654	38.8973	0.0010
721	11863	38.8798	0.0009
731	12376	38.8575	0.0011
735	12820	38.8769	0.0011
742	13513	38.8596	0.0011
748	13967	38.8608	0.0011
751	14138	38.8612	0.0011
754	14284	38.8598	0.0010
760	14570	38.8520	0.0012
763	14765	38.8265	0.0010
764	14811	38.9122	0.0011
765	14862	38.8927	0.0011
771	15149	38.8557	0.0011
781	15521	38.8827	0.0013
784	15636	38.8471	0.0012
797	16071	38.9155	0.0010
810	16420	38.8805	0.0011
826	16686	38.8874	0.0009
843	16932	38.9126	0.0011
864	17187	38.9029	0.0011

Appendix C

Figure C1:

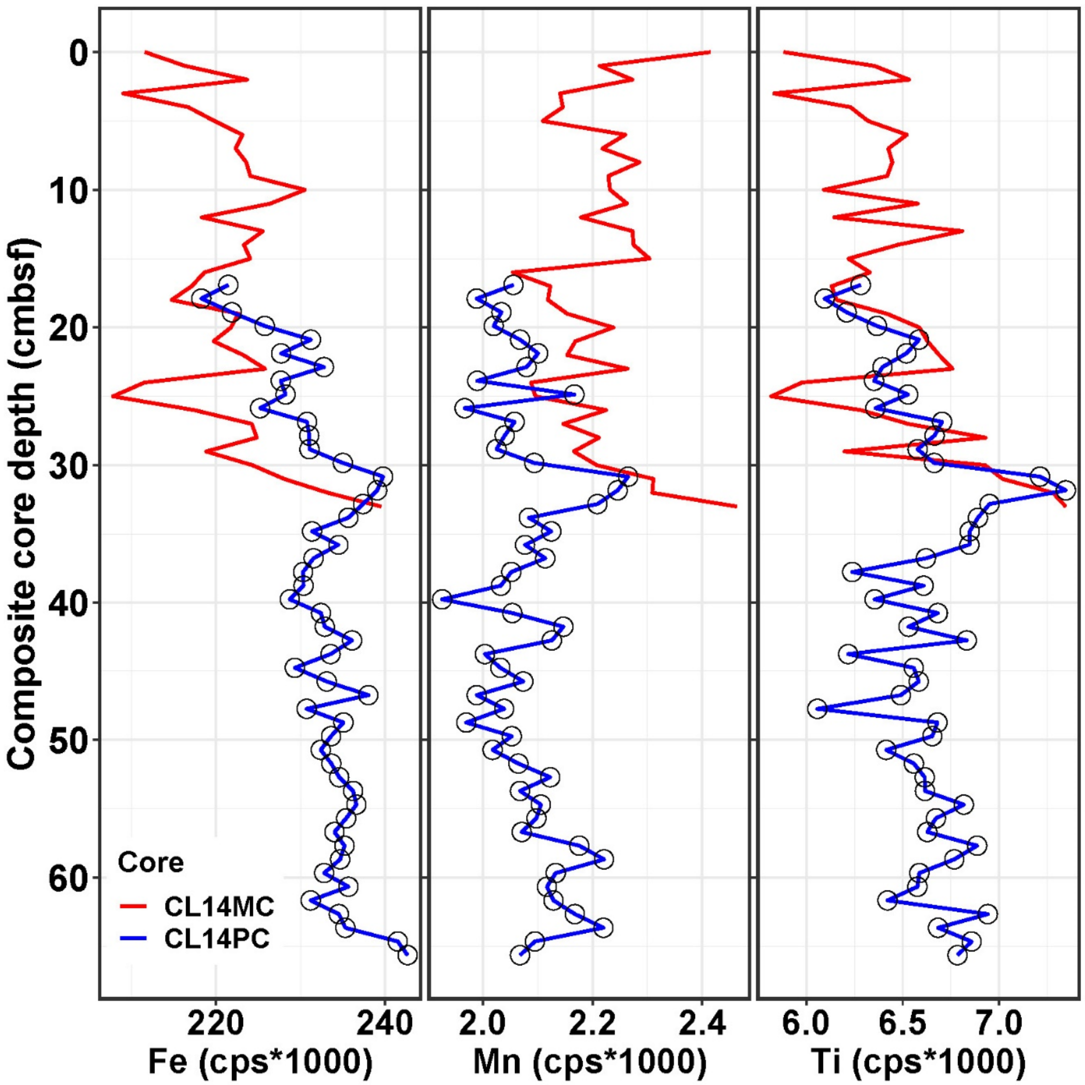

Figure C1. Determination of composite core-depth. The multiple-core sediments (CL14MC, red color line) are integrated with piston core (CL14PC, blue color line) at the same site. That was determined by the correlation of the ITRAX X-ray fluorescence (XRF) core scanner Fe, Mn, and Ti count (cps*1000, plotted in the x-axis) of downcore variability between the piston (CL14PC) and multiple (CL14MC) core. The depth is defined as composite core depth (centimeter below the seafloor scale, plotted in the y-axis).

References

Abdul, N. A., Mortlock, R. A., Wright, J. D., & Fairbanks, R. G. (2016). Younger Dryas sea level and meltwater pulse 1B recorded in Barbados reef crest coral Acropora palmata. *Paleoceanography*, *31*(2), 330–344. https://doi.org/10.1002/2015PA002847

Addison, J. A., Finney, B. P., Dean, W. E., Davies, M. H., Mix, A. C., Stoner, J. S., & Jaeger, J. M. (2012). Productivity and sedimentary δ15N variability for the last 17,000 years along the northern Gulf of Alaska continental slope. *Paleoceanography*, *27*(1), 1–17. https://doi.org/10.1029/2011PA002161

Addison, J. A., Finney, B. P., Jaeger, J. M., Stoner, J. S., Norris, R. D., & Hangsterfer, A. (2013). Integrating satellite observations and modern climate measurements with the recent sedimentary record: An example from Southeast Alaska. *Journal of Geophysical Research: Oceans*, *118*(7), 3444–3461. https://doi.org/10.1002/jgrc.20243

Agarwal, B. K. (1991). Scattering of X-rays. In *In: X-Ray Spectroscopy. Springer Series in Optical Sciences, vol 15. Springer, Berlin* (pp. 223–239). https://doi.org/10.1007/978-3-662-14469-5_5

Aguilar-Islas, A. M., Séguret, M. J. M., Rember, R., Buck, K. N., Proctor, P., Mordy, C. W., & Kachel, N. B. (2016). Temporal variability of reactive iron over the Gulf of Alaska shelf. *Deep-Sea Research Part II: Topical Studies in Oceanography*, *132*, 90–106. https://doi.org/10.1016/j.dsr2.2015.05.004

Aitchison, J., & Egozcue, J. J. (2005). Compositional data analysis: Where are we and where should we be heading? *Mathematical Geology*, *37*(7), 829–850. https://doi.org/10.1007/s11004-005-7383-7

Arth, J. G., Barker, F., & Stern, T. W. (1988). Coast batholith and taku plutons near Ketchikan, Alaska: petrography, geochronology, geochemistry, and isotopic character. *American Journal of Sciences, 288-A*, 461–489.

Asahi, H., & Takahashi, K. (2007). A 9-year time-series of planktonic foraminifer fluxes and environmental change in the Bering sea and the central subarctic Pacific Ocean , 1990 – 1999. *Progress in Oceanography*, *72*(4), 343–363. https://doi.org/10.1016/j.pocean.2006.03.021

Aung, N. N., Uryu, T., & Yoshinaga, J. (2004). Lead Isotopic Compositions of

Environmental Certified Reference Materials for an Inter-Laboratory Comparison of Lead Isotope Analysis. *Analytical Sciences, 20*(1), 195–198. https://doi.org/10.2116/analsci.20.195

Babin, D. P., Franzese, A. M., Hemming, S. R., Hall, I. R., LeVay, L. J., Barker, S., Tejeda, L., & Simon, M. H. (2020). Data report: X-ray fluorescence core scanning of IODP Site U1474 sediments, Natal Valley, Southwest Indian Ocean, Expedition 361. *Proceedings of the International Ocean Discovery Program*, *361*. https://doi.org/10.14379/iodp.proc.361.201.2020

Balbas, A. M., Barth, A. M., Clark, P. U., Clark, J., Caffee, M., O'Connor, J., Baker, V. R., Konrad, K., & Bjornstad, B. (2017). 10Be dating of late pleistocene megafloods and cordilleran ice sheet retreat in the northwestern United States. *Geology*, *45*(7), 583–586. https://doi.org/10.1130/G38956.1

Barker, F., Farmer, G. L., Ayuso, R. A., Plafker, G., & Lull, J. S. (1992). The 50 Ma granodiorite of the eastern Gulf of Alaska: Melting in an accretionary prism in the forearc. *Journal of the Geophysical Research: Solid Earth*, *97*(B5), 6757–6778. https://doi.org/10.1029/92JB00257

Barron, J. A., Bukry, D., Dean, W. E., Addison, J. A., & Finney, B. (2009). Paleoceanography of the Gulf of Alaska during the past 15,000 years: Results from diatoms, silicoflagellates, and geochemistry. *Marine Micropaleontology*, *72*(3–4), 176–195. https://doi.org/10.1016/j.marmicro.2009.04.006

Bayon, G., German, C. R., Boella, R. M., Milton, J. A., Taylor, R. N., & Nesbitt, R. W. (2002). An improved method for extracting marine sediment fractions and its application to Sr and Nd isotopic analysis. *Chemical Geology*, *187*(3–4), 179–199. https://doi.org/10.1016/S0009-2541(01)00416-8

Bemis, B. E., Spero, H. J., Bijma, J., & Lea, D. W. (1998). Reevaluation of the oxygen isotopic composition of planktonic foraminifera: Experimental results and revised paleotemperature equations. *Paleoceanography*, *13*(2), 150–160. https://doi.org/10.1029/98PA00070

Bendle, J., Rosell-Melé, A., & Ziveri, P. (2005). Variability of unusual distributions of alkenones in the surface waters of the Nordic seas. *Paleoceanography*, *20*(2), 1–15. https://doi.org/10.1029/2004PA001025

Blaauw, M., & Christen, J. A. (2011). Flexible paleoclimate age-depth models using an autoregressive gamma process. *Bayesian Analysis*, *6*(3), 457–474. https://doi.org/10.1214/11-BA618

Boyd, B. L., Anderson, J. B., Wellner, J. S., & Fernández, R. A. (2008). The sedimentary record of glacial retreat, Marinelli Fjord, Patagonia: Regional correlations and climate ties. *Marine Geology*, *255*(3–4), 165–178. https://doi.org/10.1016/j.margeo.2008.09.001

Boyle, J. F., Chiverrell, R. C., & Schillereff, D. (2015). Approaches to Water Content Correction and Calibration for µXRF Core Scanning: Comparing X-ray Scattering with Simple Regression of Elemental Concentrations. In *In: Croudace I., Rothwell R. (eds) Micro-XRF Studies of Sediment Cores. Developments in Paleoenvironmental Research, vol 17. Springer, Dordrecht.* (pp. 373–390). https://doi.org/10.1007/978-94-017-9849-5_14

Brennan, S. R., Fernandez, D. P., Mackey, G., Cerling, T. E., Bataille, C. P., Bowen, G. J., & Wooller, M. J. (2014). Strontium isotope variation and carbonate versus silicate weathering in rivers from across Alaska: Implications for provenance studies. *Chemical Geology*, *389*, 167–181. https://doi.org/10.1016/j.chemgeo.2014.08.018

Briner, J. P., & Kaufman, D. S. (2008). Late Pleistocene mountain glaciation in Alaska: key chronologies. *Journal of Quaternary Science*, *23*(6–7), 659–670. https://doi.org/10.1002/jqs.1196

Broecker, W. S. (1994). Massive iceberg discharges as triggers for global climate change. *Nature*, *372*(6505), 421–424. https://doi.org/10.1038/372421a0

Brunelle, B. G., Sigman, D. M., Jaccard, S. L., Keigwin, L. D., Plessen, B., Schettler, G., Cook, M. S., & Haug, G. H. (2010). Glacial/interglacial changes in nutrient supply and stratification in the western subarctic North Pacific since the penultimate glacial maximum. *Quaternary Science Reviews*, *29*(19–20), 2579–2590. https://doi.org/10.1016/j.quascirev.2010.03.010

Carpenter, L. J., & Liss, P. S. (2000). On temperate sources of bromoform and other reactive organic bromine gases. *Journal of Geophysical Research Atmospheres*, *105*(D16), 20539–20547. https://doi.org/10.1029/2000JD900242

Cartapanis, O., Tachikawa, K., & Bard, E. (2012). Latitudinal variations in intermediate depth ventilation and biological production over northeastern Pacific Oxygen Minimum

Zones during the last 60 ka. *Quaternary Science Reviews*, *53*(C), 24–38. https://doi.org/10.1016/j.quascirev.2012.08.009

Chagué-Goff, C., Chan, J. C. H., Goff, J., Gadd, P., Oliva, F., Peros, M. C., Viau, A. E., Reinhardt, E. G., Nixon, F. C., & Morin, A. (2016). Late Holocene record of environmental changes, cyclones and tsunamis in a coastal lake, Mangaia, Cook Islands. *Island Arc*, *25*(5), 333–349. https://doi.org/10.1111/iar.12153

Chikamoto, M. O., Menviel, L., Abe-Ouchi, A., Ohgaito, R., Timmermann, A., Okazaki, Y., Harada, N., Oka, A., & Mouchet, A. (2012). Variability in North Pacific intermediate and deep water ventilation during Heinrich events in two coupled climate models. *Deep-Sea Research Part II: Topical Studies in Oceanography*, *61–64*, 114–126. https://doi.org/10.1016/j.dsr2.2011.12.002

Childers, A. R., Whitledge, T. E., & Stockwell, D. A. (2005). Seasonal and interannual variability in the distribution of nutrients and chlorophyll a across the Gulf of Alaska shelf: 1998-2000. *Deep-Sea Research Part II: Topical Studies in Oceanography*, *52*(1–2), 193–216. https://doi.org/10.1016/j.dsr2.2004.09.018

Clague, J. J., & James, T. S. (2002). History and isostatic effects of the last ice sheet in southern British Columbia. *Quaternary Science Reviews*, *21*(1–3), 71–87. https://doi.org/10.1016/S0277-3791(01)00070-1

Clark, P. U., Marshall, S. J., Clarke, G. K. C., Hostetler, S. W., Licciardi, J. M., & Teller, J. T. (2001). Freshwater forcing of abrupt climate change during the last glaciation. *Science*, *293*(5528), 283–287. https://doi.org/10.1126/science.1062517

Clark, Peter U., & Mix, A. C. (2002). Ice sheets and sea level of the Last Glacial Maximum. *Quaternary Science Reviews*, *21*(1–3), 1–7. https://doi.org/10.1016/S0277-3791(01)00118-4

Clark, Peter U., Pisias, N. G., Stocker, T. F., & Weaver, A. J. (2002). The role of the thermohaline circulation in abrupt climate change. *Nature*, *415*, 863–869. https://doi.org/10.1038/415863a

Clark, Peter U., Shakun, J. D., Baker, P. A., Bartlein, P. J., Brewer, S., Brook, E., Carlson, A. E., Cheng, H., Kaufman, D. S., Liu, Z., Marchitto, T. M., Mix, A. C., Morrill, C., Otto-Bliesner, B. L., Pahnke, K., Russell, J. M., Whitlock, C., Adkins, J. F., Blois, J. L., … Williams, J. W. (2012). Global climate evolution during the last deglaciation.

Proceedings of the National Academy of Sciences of the United States of America, *109*(19). https://doi.org/10.1073/pnas.1116619109

Clinger, A. E., Aciego, S. M., Stevenson, E. I., Arendt, C. A., & Robbins, M. J. (2016). Implications for post-comminution processes in subglacial suspended sediment using coupled radiogenic strontium and neodymium isotopes. *Geomorphology*, *259*, 134–144. https://doi.org/10.1016/j.geomorph.2016.02.006

Comas Cufí, M., & Thió-Henestrosa, S. (2011). CoDaPack 2.0: a stand-alone, multi-platform compositional software. *In: Egozcue JJ, Tolosana-Delgado R, Ortego MI, Eds. CoDaWork'11: 4th International Workshop on Compositional Data Analysis. Sant Feliu de Guíxols*, 1–10.

Cosma, T., & Hendy, I. L. (2008). Pleistocene glacimarine sedimentation on the continental slope off Vancouver Island, British Columbia. *Marine Geology*, *255*(1–2), 45–54. https://doi.org/10.1016/j.margeo.2008.07.001

Costa, K. M., McManus, J. F., & Anderson, R. F. (2018). Paleoproductivity and Stratification Across the Subarctic Pacific Over Glacial-Interglacial Cycles. *Paleoceanography and Paleoclimatology*, *33*(9), 914–933. https://doi.org/10.1029/2018PA003363

Croudace, I. W., Rindby, A., & Rothwell, R. G. (2006). ITRAX: Description and evaluation of a new multi-function X-ray core scanner. *Geological Society Special Publication*, *267*, 51–63. https://doi.org/10.1144/GSL.SP.2006.267.01.04

Crusius, J., Schroth, A. W., Gassó, S., Moy, C. M., Levy, R. C., & Gatica, M. (2011). Glacial flour dust storms in the Gulf of Alaska: Hydrologic and meteorological controls and their importance as a source of bioavailable iron. *Geophysical Research Letters*, *38*(6), 1–5. https://doi.org/10.1029/2010GL046573

Currie, Ll. A. (1995). Nomenclature in evaluation of analytical methods including detection and quantification capabilities (IUPAC Recommendations 1995). *Pure and Applied Chemistry*, *67*(10), 1699–1723. https://doi.org/10.1351/pac199567101699

Dalton, A. S., Margold, M., Stokes, C. R., Tarasov, L., Dyke, A. S., Adams, R. S., Allard, S., Arends, H. E., Atkinson, N., Attig, J. W., Barnett, P. J., Barnett, R. L., Batterson, M., Bernatchez, P., Borns, H. W., Breckenridge, A., Briner, J. P., Brouard, E., Campbell, J. E., … Wright, H. E. (2020). An updated radiocarbon-based ice margin chronology for the last deglaciation of the North American Ice Sheet Complex. *Quaternary Science*

Reviews, *234*, 106223. https://doi.org/10.1016/j.quascirev.2020.106223

Darvill, C. M., Menounos, B., Goehring, B. M., Lian, O. B., & Caffee, M. W. (2018). Retreat of the Western Cordilleran Ice Sheet Margin During the Last Deglaciation. *Geophysical Research Letters, 45*(18), 9710–9720. https://doi.org/10.1029/2018GL079419

Davies-Walczak, M., Mix, A. C., Stoner, J. S., Southon, J. R., Cheseby, M., & Xuan, C. (2014). Late Glacial to Holocene radiocarbon constraints on North Pacific Intermediate Water ventilation and deglacial atmospheric CO2 sources. *Earth and Planetary Science Letters*, *397*, 57–66. https://doi.org/10.1016/j.epsl.2014.04.004

Davies, M. H., Mix, A. C., Stoner, J. S., Addison, J. A., Jaeger, J., Finney, B., & Wiest, J. (2011). The deglacial transition on the southeastern Alaska Margin: Meltwater input, sea level rise, marine productivity, and sedimentary anoxia. *Paleoceanography, 26*(2), 1–18. https://doi.org/10.1029/2010PA002051

Dawson, G. M. (1888). III.—Recent Observations on the Glaciation of British Columbia and Adjacent Regions. *Geological Magazine*, *5*(8), 347–350. https://doi.org/10.1017/S0016756800182159

de Vernal, A., & Pedersen, T. F. (1997). Micropaleontology and palynology of core PAR87A-10: A 23,000 year record of paleoenvironmental changes in the Gulf of Alaska, Northeast North Pacific. *Paleoceanography*, *12*(6), 821–830. https://doi.org/10.1029/97PA02167

Dembitsky, V. M. (2002). Bromo- and iodo-containing alkaloids from marine microorganisms and sponges. *Russian Journal of Bioorganic Chemistry*, *28*(3), 170–182. https://doi.org/10.1023/A:1015748018820

Deschamps, P., Durand, N., Bard, E., Hamelin, B., Camoin, G., Thomas, A. L., Henderson, G. M., Okuno, J., & Yokoyama, Y. (2012). Ice-sheet collapse and sea-level rise at the Bølling warming 14,600 years ago. *Nature*, *483*(7391), 559–564. https://doi.org/10.1038/nature10902

Diekmann, B., Hofmann, J., Henrich, R., Fütterer, D. K., Röhl, U., & Wei, K. Y. (2008). Detrital sediment supply in the southern Okinawa Trough and its relation to sea-level and Kuroshio dynamics during the late Quaternary. *Marine Geology*, *255*(1–2), 83–95. https://doi.org/10.1016/j.margeo.2008.08.001

Dunlea, A. G., Murray, R. W., Tada, R., Alvarez-Zarikian, C. A., Anderson, C. H., Gilli, A., Giosan, L., Gorgas, T., Hennekam, R., Irino, T., Murayama, M., Peterson, L. C., Reichart, G. J., Seki, A., Zheng, H., & Ziegler, M. (2020). Intercomparison of XRF Core Scanning Results From Seven Labs and Approaches to Practical Calibration. *Geochemistry, Geophysics, Geosystems*, *21*(9), 1–13. https://doi.org/10.1029/2020GC009248

Dunn, C. A., Enkelmann, E., Ridgway, K. D., & Allen, W. K. (2017). Source to sink evaluation of sediment routing in the Gulf of Alaska and Southeast Alaska: A thermochronometric perspective. *Journal of Geophysical Research: Earth Surface*, *122*(3), 711–734. https://doi.org/10.1002/2016JF004168

Dyke, A.S., Moore, A., & Robertson, L. (2003). *Deglaciation of North America: Thirty-two digital maps at 1:7,000,000 scale with accompanying digital chronological database and one poster (two sheets) with full map series. Geological Survey of Canada, Open File 1574*. https://doi.org/10.4095/214399

Dyke, Arthur S. (2004). An outline of North American deglaciation with emphasis on central and northern Canada. *Developments in Quaternary Sciences*, *2*(Part B), 373–424. https://doi.org/10.1016/S1571-0866(04)80209-4

Farmer, G. L., Ayuso, R., & Plafker, G. (1993). A Coast Mountains provenance for the Valdez and Orca groups, southern Alaska, based on Nd, Sr, and Pb isotopic evidence. *Earth and Planetary Science Letters*, *116*(1–4), 9–21. https://doi.org/10.1016/0012-821X(93)90042-8

Feely, R. A., Baker, E. T., Schumacher, J. D., Massoth, G. J., & Landing, W. M. (1979). Processes affecting the distribution and transport of suspended matter in the northeast Gulf of Alaska. *Deep Sea Research Part A, Oceanographic Research Papers*, *26*(4), 445–464. https://doi.org/10.1016/0198-0149(79)90057-8

Ferrat, M., Weiss, D. J., Dong, S., Large, D. J., Spiro, B., Sun, Y., & Gallagher, K. (2012). Lead atmospheric deposition rates and isotopic trends in Asian dust during the last 9.5kyr recorded in an ombrotrophic peat bog on the eastern Qinghai-Tibetan Plateau. *Geochimica et Cosmochimica Acta*, *82*, 4–22. https://doi.org/10.1016/j.gca.2010.10.031

Flower, B. P., Hastings, D. W., Hill, H. W., & Quinn, T. M. (2004). Phasing of deglacial warming and Laurentide Ice Sheet meltwater in the Gulf of Mexico. *Geology*, *32*(7), 597–600. https://doi.org/10.1130/G20604.1

Gazulla, M. F., Rodrigo, M., Vicente, S., & Orduña, M. (2010). Methodology for the determination of minor and trace elements in petroleum cokes by wavelength-dispersive X-ray fluorescence (WD-XRF). *X-Ray Spectrometry*, *39*(5), 321–327. https://doi.org/10.1002/xrs.1270

Gebhardt, H., Sarnthein, M., Grootes, P. M., Kiefer, T., Kuehn, H., Schmieder, F., & Röhl, U. (2008). Paleonutrient and productivity records from the subarctic North Pacific for Pleistocene glacial terminations I to V. *Paleoceanography*, *23*(4), 1–21. https://doi.org/10.1029/2007PA001513

Gerringa, L. J. A., Alderkamp, A. C., Laan, P., Thuróczy, C. E., De Baar, H. J. W., Mills, M. M., van Dijken, G. L., Haren, H. van, & Arrigo, K. R. (2012). Iron from melting glaciers fuels the phytoplankton blooms in Amundsen Sea (Southern Ocean): Iron biogeochemistry. *Deep-Sea Research Part II: Topical Studies in Oceanography*, *71–76*, 16–31. https://doi.org/10.1016/j.dsr2.2012.03.007

Gombiner, J. H., Hemming, S. R., Hendy, I. L., Bryce, J. G., & Blichert-Toft, J. (2016). Isotopic and elemental evidence for Scabland Flood sediments offshore Vancouver Island. *Quaternary Science Reviews*, *139*, 129–137. https://doi.org/10.1016/j.quascirev.2016.02.026

Gonyo, A. W., Yu, Z., & Bebout, G. E. (2012). Late Holocene change in climate and atmospheric circulation inferred from geochemical records at Kepler Lake, south-central Alaska. *Journal of Paleolimnology*, *48*(1), 55–67. https://doi.org/10.1007/s10933-012-9603-8

Goodwin, K. D., North, W. J., & Lidstrom, M. E. (1997). Production of bromoform and dibromomethane by Giant Kelp : Factors affecting release and comparison to anthropogenic bromine sources. *Limnology and Oceanography*, *42*(8), 1725–1734. https://doi.org/10.4319/lo.1997.42.8.1725

Gorbarenko, S., Shi, X., Zou, J., Velivetskaya, T., Artemova, A., Liu, Y., Yanchenko, E., & Vasilenko, Y. (2019). Evidence of meltwater pulses into the North Paci fi c over the last 20 ka due to the decay of Kamchatka Glaciers and Cordilleran Ice Sheet. *Global and Planetary Change*, *172*, 33–44. https://doi.org/10.1016/j.gloplacha.2018.09.014

Gregoire, L. J., Payne, A. J., & Valdes, P. J. (2012). Deglacial rapid sea level rises caused by ice-sheet saddle collapses. *Nature*, *487*(7406), 219–222. https://doi.org/10.1038/nature11257

Gregory, B. R. B., Patterson, R. T., Reinhardt, E. G., Galloway, J. M., & Roe, H. M. (2019). An evaluation of methodologies for calibrating Itrax X-ray fluorescence counts with ICP-MS concentration data for discrete sediment samples. *Chemical Geology*, *521*, 12–27. https://doi.org/10.1016/j.chemgeo.2019.05.008

Gribble, G. W. (2000). The natural production of organobromine compounds. *Environmental Science and Pollution Research*, *7*(1), 37–49. https://doi.org/10.1065/espr199910.002

Guevara, M., Verma, S. P., Velasco-Tapia, F., Lozano-Santa Cruz, R., & Girón, P. (2005). Comparison of Linear Regression Models for Quantitative Geochemical Analysis: An Example Using X-Ray Fluorescence Spectrometry. *Geostandards and Geoanalytical Research*, *29*(3), 271–284. https://doi.org/10.1111/j.1751-908x.2005.tb00900.x

Hallmann, N., Schöne, B. R., Irvine, G. V., Burchell, M., Cokelet, E. D., & Hilton, M. R. (2011). An Improved Understanding of the Alaska Coastal Current: the Application of a Bivalve Growth-Temperature Model To Reconstruct Freshwater-Influenced Paleoenvironments. *Palaios*, *26*(6), 346–363. https://doi.org/10.2110/palo.2010.p10-151r

Hamilton, T.D., Thorson, R. M. (1983). The Cordilleran ice sheet in Alaska. *In: Porter, S. C. (Ed.), Late Quaternary Environments of the United States, 1, The Late Pleistocene. Minneapolis, University of Minnesota Press*, 38–52.

Hamilton, T. D. (1994). Late Cenozoic glaciation of Alaska. *In: Plafker, G. & Berg, H. C. (Eds), The Geology of Alaska, The Geology of North America, G-1. Boulder, Colorado, Geological Society of America*, 813–844.

Harada, N., Shin, K. H., Murata, A., Uchida, M., & Nakatani, T. (2003). Characteristics of alkenones synthesized by a bloom of *Emiliania huxleyi* in the Bering Sea. *Geochimica et Cosmochimica Acta*, *67*(8), 1507–1519. https://doi.org/10.1016/S0016-7037(02)01318-2

Haslett, J., & Parnell, A. (2008). A simple monotone process with application to radiocarbon-dated depth chronologies. *Journal of the Royal Statistical Society. Series C: Applied Statistics*, *57*(4), 399–418. https://doi.org/10.1111/j.1467-9876.2008.00623.x

Heaton, T. J., Köhler, P., Butzin, M., Bard, E., Reimer, R. W., Austin, W. E. N., Bronk

Ramsey, C., Grootes, P. M., Hughen, K. A., Kromer, B., Reimer, P. J., Adkins, J., Burke, A., Cook, M. S., Olsen, J., & Skinner, L. C. (2020). Marine20 - The Marine Radiocarbon Age Calibration Curve (0-55,000 cal BP). *Radiocarbon, 62*(4), 779–820. https://doi.org/10.1017/RDC.2020.68

Hedges, J. I., & Stern, J. H. (1984). Carbon and nitrogen determinations of carbonate-containing solids. *Limnology and Oceanography, 29*(3), 657–663. https://doi.org/10.4319/lo.1984.29.3.0657

Hennekam, R., & de Lange, G. (2012). X-ray fluorescence core scanning of wet marine sediments: Methods to improve quality and reproducibility of high resolution paleoenvironmental records. *Limnology and Oceanography: Methods, 10*(12), 991–1003. https://doi.org/10.4319/lom.2012.10.991

Heyman, J., Stroeven, A. P., Harbor, J. M., & Caffee, M. W. (2011). Too young or too old: Evaluating cosmogenic exposure dating based on an analysis of compiled boulder exposure ages. *Earth and Planetary Science Letters*, *302*(1–2), 71–80. https://doi.org/10.1016/j.epsl.2010.11.040

Hill, V. L., & Manley, S. L. (2009). Release of reactive bromine and iodine from diatoms and its possible role in halogen transfer in polar and tropical oceans. *Limnology and Oceanography, 54*(3), 812–822. https://doi.org/10.4319/lo.2009.54.3.0812

Hillaire-Marcel, C., De Vernal, A., Polyak, L., & Darby, D. (2004). Size-dependent isotopic composition of planktic foraminifers from Chukchi Sea vs. NW Atlantic sediments - Implications for the Holocene paleoceanography of the western Arctic. *Quaternary Science Reviews*, *23*(3–4), 245–260. https://doi.org/10.1016/j.quascirev.2003.08.006

Hodell, D. A., Channeil, J. E. T., Curtis, J. H., Romero, O. E., & Röhl, U. (2008). Onset of “Hudson Strait” Heinrich events in the eastern North Atlantic at the end of the middle Pleistocene transition (~640 ka)? *Paleoceanography, 23*(4), 1–16. https://doi.org/10.1029/2008PA001591

Hood, E., & Scott, D. (2008). Riverine organic matter and nutrients insoutheast Alaska affected by glacial coverage. *Nature Geoscience*, *1*(9), 583–587. https://doi.org/10.1038/ngeo280

Horikawa, K., Martin, E. E., Asahara, Y., & Sagawa, T. (2011). Limits on conservative behavior of Nd isotopes in seawater assessed from analysis of fish teeth from Pacific core tops. *Earth and Planetary Science Letters*, *310*(1–2), 119–130. https://doi.org/10.1016/j.epsl.2011.07.018

Horikawa, K., Martin, E. E., Basak, C., Onodera, J., Seki, O., Sakamoto, T., Ikehara, M., Sakai, S., & Kawamura, K. (2015). Pliocene cooling enhanced by flow of low-salinity Bering Sea water to the Arctic Ocean. *Nature Communications*, *6*(August), 1–9. https://doi.org/10.1038/ncomms8587

Hunt, J. E., Croudace, I. W., & MacLachlan, S. E. (2015). Use of Calibrated ITRAX XRF Data in Determining Turbidite Geochemistry and Provenance in Agadir Basin, Northwest African Passive Margin. In I.W. Croudace & R. . Rothwell (Eds.), *Micro-XRF Studies of Sediment Cores. Developments in Paleoenvironmental Research* (Vol. 17, pp. 127–146). Springer, Dordrecht. https://doi.org/10.1007/978-94-017-9849-5_4

Husson, F., Lê, S., & Pagès, J. (2017). Exploratory Multivariate Analysis by Example Using R. In *Chapman and Hall/CRC Press.*

Imai, N., Terashima, S., Itoh, S., & Ando, A. (1995). 1994 Compilation of Analytical Data for Minor and Trace Elements in Seventeen Gsj Geochemical Reference Samples, “Igneous Rock Series.” *Geostandards Newsletter*, *19*(2), 135–213. https://doi.org/10.1111/j.1751-908X.1995.tb00158.x

Ito, A. (2011). Mega fire emissions in Siberia: Potential supply of bioavailable iron from forests to the ocean. *Biogeosciences*, *8*(6), 1679–1697. https://doi.org/10.5194/bg-8-1679-2011

Iwasaki, S., Kimoto, K., Kuroyanagi, A., & Kawahata, H. (2017). Horizontal and vertical distributions of planktic foraminifera in the subarctic Pacific. *Marine Micropaleontology*, *130*, 1–14. https://doi.org/10.1016/j.marmicro.2016.12.001

Jaccard, S. L., Haug, G. H., Sigman, D. M., Pedersen, T. F., Thierstein, H. R., & Röhl, U. (2005). Glacial/interglacial changes in subarctic north pacific stratification. *Science*, *308*(5724), 1003–1006. https://doi.org/10.1126/science.1108696

Jacobsen, S. B., & Wasserburg, G. J. (1980). Sm-Nd isotopic evolution of chondrites. *Earth and Planetary Science Letters*, *50*(1), 139–155. https://doi.org/10.1016/0012-821X(80)90125-9

Jakobsson, M., Pearce, C., Cronin, T. M., Backman, J., Anderson, L. G., Barrientos, N., Björk, G., Coxall, H., De Boer, A., Mayer, L. A., Mörth, C. M., Nilsson, J., Rattray, J. E., Stranne, C., Semiletov, I., & O'Regan, M. (2017). Post-glacial flooding of the Bering Land Bridge dated to 11 cal ka BP based on new geophysical and sediment records. *Climate of the Past*, *13*(8), 991–1005. https://doi.org/10.5194/cp-13-991-2017

Johnson, K. S., Chavez, F. P., Elrod, V. A., Fitzwater, S. E., Pennington, J. T., Buck, K. R., & Walz, P. M. (2001). The annual cycle of iron and the biological response in central California coastal waters. *Geophysical Research Letters*, *28*(7), 1247–1250. https://doi.org/10.1029/2000GL012433

Jonkers, L., Brummer, G. J. A., Peeters, F. J. C., Van Aken, H. M., & De Jong, M. F. (2010). Seasonal stratification, shell flux, and oxygen isotope dynamics of left coiling *N. pachyderma* and *T. quinqueloba* in the western subpolar North Atlantic. *Paleoceanography*, *25*(2), 1–13. https://doi.org/10.1029/2009PA001849

Kaufman, D. S., & Manley, W. F. (2004). Pleistocene Maximum and Late Wisconsinan glacier extents across Alaska, U.S.A. *Developments in Quaternary Science*, *2*(Part B), 9–27. https://doi.org/10.1016/S1571-0866(04)80182-9

Keigwin, L. D., Jones, G. A., & Froelich, P. N. (1992). A 15,000 year paleoenvironmental record from Meiji Seamount, far northwestern Pacific. *Earth and Planetary Science Letters*, *111*(2–4), 425–440. https://doi.org/10.1016/0012-821X(92)90194-Z

Kido, Y., Koshikawa, T., & Tada, R. (2006). Rapid and quantitative major element analysis method for wet fine-grained sediments using an XRF microscanner. *Marine Geology*, *229*(3–4), 209–225. https://doi.org/10.1016/j.margeo.2006.03.002

Kipphut, G. W. (1990). Glacial meltwater input to the Alaska coastal current: evidence from oxygen isotope measurements. *Journal of Geophysical Research*, *95*(C4), 5177–5181. https://doi.org/10.1029/JC095iC04p05177

Komárek, M., Ettler, V., Chrastný, V., & Mihaljevič, M. (2008). Lead isotopes in environmental sciences: A review. *Environment International*, *34*(4), 562–577. https://doi.org/10.1016/j.envint.2007.10.005

Kozaka, Y., Horikawa, K., Asahara, Y., Amakawa, H., & Okazaki, Y. (2018). Late Miocene-mid-Pliocene tectonically induced formation of the semi-closed Japan Sea, inferred from seawater Nd isotopes. *Geology*, *46*(10), 903–906. https://doi.org/10.1130/G45033.1

Kuroyanagi, A., & Kawahata, H. (2004). Vertical distribution of living planktonic foraminifera in the seas around Japan. *Marine Micropaleontology, 53*(1–2), 173–196. https://doi.org/10.1016/j.marmicro.2004.06.001

Kuroyanagi, A., Kawahata, H., & Nishi, H. (2011). Seasonal variation in the oxygen isotopic composition of different-sized planktonic foraminifer Neogloboquadrina pachyderma (sinistral) in the northwestern North Pacific and implications for reconstruction of the paleoenvironment. *Paleoceanography, 26*(4), 1–10. https://doi.org/10.1029/2011PA002153

Kylander, M. E., Ampel, L., Wohlfarth, B., & Veres, D. (2011). High-resolution X-ray fluorescence core scanning analysis of Les Echets (France) sedimentary sequence: New insights from chemical proxies. *Journal of Quaternary Science, 26*(1), 109–117. https://doi.org/10.1002/jqs.1438

Lam, P. J., Robinson, L. F., Blusztajn, J., Li, C., Cook, M. S., McManus, J. F., & Keigwin, L. D. (2013). Transient stratification as the cause of the North Pacific productivity spike during deglaciation. *Nature Geoscience, 6*(8), 622–626. https://doi.org/10.1038/ngeo1873

Lambeck, K., Purcell, A., & Zhao, S. (2017). The North American Late Wisconsin ice sheet and mantle viscosity from glacial rebound analyses. *Quaternary Science Reviews, 158*, 172–210. https://doi.org/10.1016/j.quascirev.2016.11.033

Lambeck, K., Rouby, H., Purcell, A., Sun, Y., & Sambridge, M. (2014). Sea level and global ice volumes from the Last Glacial Maximum to the Holocene. *Proceedings of the National Academy of Sciences of the United States of America, 111*(43), 15296–15303. https://doi.org/10.1073/pnas.1411762111

Lê, S., Josse, J., & Husson, F. (2008). FactoMineR: An R Package for Multivariate Analysis. *Journal of Statistical Software, 25*(1), 1–18. https://doi.org/10.18637/jss.v025.i01

Lee, A. S., Huang, J. J. S., Burr, G., Kao, L. C., Wei, K. Y., & Liou, S. Y. H. (2019). High resolution record of heavy metals from estuary sediments of Nankan River (Taiwan) assessed by rigorous multivariate statistical analysis. *Quaternary International, 527*, 44–51. https://doi.org/10.1016/j.quaint.2018.11.018

Leri, A. C., Hakala, J. A., Marcus, M. A., Lanzirotti, A., Reddy, C. M., & Myneni, S. C. B. (2010). Natural organobromine in marine sediments: New evidence of biogeochemical

Br cycling. *Global Biogeochemical Cycles*, *24*(4), 1–15. https://doi.org/10.1029/2010GB003794

Leri, A. C., Mayer, L. M., Thornton, K. R., & Ravel, B. (2014). Bromination of marine particulate organic matter through oxidative mechanisms. *Geochimica et Cosmochimica Acta*, *142*(1), 53–63. https://doi.org/10.1016/j.gca.2014.08.012

Lesnek, A. J., Briner, J. P., Baichtal, J. F., & Lyles, A. S. (2020). New constraints on the last deglaciation of the Cordilleran Ice Sheet in coastal Southeast Alaska. *Quaternary Research (United States)*, *96*(May), 140–160. https://doi.org/10.1017/qua.2020.32

Lesnek, A. J., Briner, J. P., Lindqvist, C., Baichtal, J. F., & Heaton, T. H. (2018). Deglaciation of the pacific coastal corridor directly preceded the human colonization of the Americas. *Science Advances, 4*(5), eaar5040. https://doi.org/10.1126/sciadv.aar5040

Li, Y., Liu, G., Chen, Y., Li, Y., Harbor, J., Stroeven, A. P., Caffee, M., Zhang, M., Li, C., & Cui, Z. (2014). Timing and extent of Quaternary glaciations in the Tianger Range, eastern Tian Shan, China, investigated using 10Be surface exposure dating. *Quaternary Science Reviews*, *98*, 7–23. https://doi.org/10.1016/j.quascirev.2014.05.009

Lim, Y. K., Phang, S. M., Abdul Rahman, N., Sturges, W. T., & Malin, G. (2017). Halocarbon emissions from marine phytoplankton and climate change. *International Journal of Environmental Science and Technology*, *14*(6), 1355–1370. https://doi.org/10.1007/s13762-016-1219-5

Linsinger, T. (2010). Comparison of a measurement result with the certified value. *European Reference Materials*, 1–2.

Lippiatt, S. M., Lohan, M. C., & Bruland, K. W. (2010). The distribution of reactive iron in northern Gulf of Alaska coastal waters. *Marine Chemistry*, *121*(1–4), 187–199. https://doi.org/10.1016/j.marchem.2010.04.007

Llamas, B., Fehren-Schmitz, L., Valverde, G., Soubrier, J., Mallick, S., Rohland, N., Nordenfelt, S., Valdiosera, C., Richards, S. M., Rohrlach, A., Romero, M. I. B., Espinoza, I. F., Cagigao, E. T., Jiménez, L. W., Makowski, K., Reyna, I. S. L., Lory, J. M., Torrez, J. A. B., Rivera, M. A., … Haak, W. (2016). Ancient mitochondrial DNA provides high-resolution time scale of the peopling of the Americas. *Science Advances*, *2*(4), e1501385. https://doi.org/10.1126/sciadv.1501385

Loska, K., & Wiechuła, D. (2003). Application of principal component analysis for the estimation of source of heavy metal contamination in surface sediments from the Rybnik Reservoir. *Chemosphere, 51*(8), 723–733. https://doi.org/10.1016/S0045-6535(03)00187-5

Lyle, M., Kulhanek, D. K., Bowen, M. G., & Hahn, A. (2018). Data report: X-ray fluorescence studies of Site U1457 sediments, Laxmi Basin, Arabian Sea. *Proceedings of the International Ocean Discovery Program, 355*. https://doi.org/10.14379/iodp.proc.355.203.2018

Lyle, M., Oliarez Lyle, A., Gorgas, T., Holbourn, A., Westerhold, T., Hathorne, E., Kimoto, K., & Yamamoto, S. (2012). Data report: raw and normalized elemental data along the Site U1338 splice from X-ray fluorescence scanning. *Proceedings of the Integrated Ocean Drilling Program, 320/321*. https://doi.org/10.2204/iodp.proc.320321.203.2012

MacLachlan, S. E., Hunt, J. E., & Croudace, I. W. (2015). An Empirical Assessment of Variable Water Content and Grain-Size on X-Ray Fluorescence Core-Scanning Measurements of Deep Sea Sediments. In *In: Croudace I., Rothwell R. (eds) Micro-XRF Studies of Sediment Cores. Developments in Paleoenvironmental Research, vol 17. Springer, Dordrecht.* (pp. 173–185). https://doi.org/10.1007/978-94-017-9849-5_6

MacQueen, J. (1967). Some methods for classification and analysis of multivariate observations. *Proceedings of the Fifth Berkeley Symposium on Mathematical Statistics and Probability, 1*(14), 281–297.

Maier, E., Méheust, M., Abelmann, A., Gersonde, R., Chapligin, B., Ren, J., Stein, R., Meyer, H., & Tiedemann, R. (2015). Deglacial subarctic Pacific surface water hydrography and nutrient dynamics and links to North Atlantic climate variability and atmospheric CO2. *Paleoceanography, 30*(7), 949–968. https://doi.org/10.1002/2014PA002763

Maier, E., Zhang, X., Abelmann, A., Gersonde, R., Mulitza, S., Werner, M., Méheust, M., Ren, J., Chapligin, B., Meyer, H., Stein, R., Tiedemann, R., & Lohmann, G. (2018). North Pacific freshwater events linked to changes in glacial ocean circulation. *Nature, 559*(7713), 241–245. https://doi.org/10.1038/s41586-018-0276-y

Malcolm, S. J., & Price, N. B. (1984). The behaviour of iodine and bromine in estuarine surface sediments. *Marine Chemistry, 15*(3), 263–271. https://doi.org/10.1016/0304-

4203(84)90022-7

Mann, D. H., & Peteet, D. M. (1994). Extent and Timing of the Last Glacial Maximum in Southwestern Alaska. *Quaternary Research*, *42*(2), 136–148. https://doi.org/10.1006/qres.1994.1063

Marcott, S. A., Clark, P. U., Padman, L., Klinkhammer, G. P., Springer, S. R., Liu, Z., Otto-Bliesner, B. L., Carlson, A. E., Ungerer, A., Padman, J., He, F., Cheng, J., & Schmittner, A. (2011). Ice-shelf collapse from subsurface warming as a trigger for Heinrich events. *Proceedings of the National Academy of Sciences of the United States of America*, *108*(33), 13415–13419. https://doi.org/10.1073/pnas.1104772108

Margold, M., Gosse, J. C., Hidy, A. J., Woywitka, R. J., Young, J. M., & Froese, D. (2019). Beryllium-10 dating of the Foothills Erratics Train in Alberta, Canada, indicates detachment of the Laurentide Ice Sheet from the Rocky Mountains at ∼15 ka. *Quaternary Research (United States)*, *92*(2), 469–482. https://doi.org/10.1017/qua.2019.10

Margold, M., Stroeven, A. P., Clague, J. J., & Heyman, J. (2014). Timing of terminal Pleistocene deglaciation at high elevations in southern and central British Columbia constrained by 10Be exposure dating. *Quaternary Science Reviews*, *99*, 193–202. https://doi.org/10.1016/j.quascirev.2014.06.027

Martin-Puertas, C., Tjallingii, R., Bloemsma, M., & Brauer, A. (2017). Varved sediment responses to early Holocene climate and environmental changes in Lake Meerfelder Maar (Germany) obtained from multivariate analyses of micro X-ray fluorescence core scanning data. *Journal of Quaternary Science*, *32*(3), 427–436. https://doi.org/10.1002/jqs.2935

Matthews, J. A., Shakesby, R. A., & Fabel, D. (2017). Very low inheritance in cosmogenic surface exposure ages of glacial deposits: A field experiment from two Norwegian glacier forelands. *Holocene*, *27*(9), 1406–1414. https://doi.org/10.1177/0959683616687387

Mayer, L. M., Schick, L. L., Allison, M. A., Ruttenberg, K. C., & Bentley, S. J. (2007). Marine vs. terrigenous organic matter in Louisiana coastal sediments: The uses of bromine: organic carbon ratios. *Marine Chemistry*, *107*(2), 244–254. https://doi.org/10.1016/j.marchem.2007.07.007

McManus, J. F., Francois, R., Gherardl, J. M., Kelgwin, L., & Drown-Leger, S. (2004). Collapse and rapid resumption of Atlantic meridional circulation linked to deglacial climate changes. *Nature*, *428*(6985), 834–837. https://doi.org/10.1038/nature02494

McNeely, R., Dyke, A. S., & Southon, J. R. (2006). Canadian Marine Reservoir Ages, Preliminary Data Assessment. *Geological Survey of Canada. Open File*, 5049, 3 pp.

Menounos, B., Goehring, B. M., Osborn, G., Margold, M., Ward, B., Bond, J., Clarke, G. K. C., Clague, J. J., Lakeman, T., Koch, J., Caffee, M. W., Gosse, J., Stroeven, A. P., Seguinot, J., & Heyman, J. (2017). Cordilleran Ice Sheet mass loss preceded climate reversals near the Pleistocene Termination. *Science*, *358*(6364), 781–784. https://doi.org/10.1126/science.aan3001

Miller, J. N., Miller, J. C., & Miller, R. D. (2018). *Statistics and Chemometrics for Analytical Chemistry* (7th Editio). Pearson Education Limited, Harlow, United Kingdom.

Misarti, N., Finney, B. P., Jordan, J. W., Maschner, H. D. G., Addison, J. A., Shapley, M. D., Krumhardt, A., & Beget, J. E. (2012). Early retreat of the Alaska Peninsula Glacier Complex and the implications for coastal migrations of First Americans. *Quaternary Science Reviews*, *48*, 1–6. https://doi.org/10.1016/j.quascirev.2012.05.014

Mondal, M. N., Horikawa, K., Osamu, S., Nejigaki, K., Minami, H., Murayama, M., & Okazaki, Y. (2021). Investigation of Adequate Calibration Methods for X-Ray Fluorescence Core Scanning Element Count Data : A Case Study of a Marine Sediment Piston Core from the Gulf of Alaska. *Journal of Marine Science and Engineering*, *9*(5), 1–21. https://doi.org/10.3390/jmse9050540

Müller, J., Romero, O., Cowan, E. A., McClymont, E. L., Forwick, M., Asahi, H., März, C., Moy, C. M., Suto, I., Mix, A., & Stoner, J. (2018). Cordilleran ice-sheet growth fueled primary productivity in the Gulf of Alaska, northeast Pacific Ocean. *Geology*, *46*(4), 307–310. https://doi.org/10.1130/G39904.1

Mundy, P. R. (2005). The Gulf of Alaska: Biology and Oceanography. In *Alaska Sea Grant College Program, University of Alaska Fairbanks*. Alaska Sea Grant, University of Alaska Fairbanks. https://doi.org/10.4027/gabo.2005

Munyikwa, K., Feathers, J. K., Rittenour, T. M., & Shrimpton, H. K. (2011). Constraining the Late Wisconsinan retreat of the Laurentide ice sheet from western Canada using luminescence ages from postglacial aeolian dunes. *Quaternary Geochronology*, *6*(3–4), 407–422. https://doi.org/10.1016/j.quageo.2011.03.010

Murtagh, F., & Legendre, P. (2014). Ward’s Hierarchical Agglomerative Clustering Method: Which Algorithms Implement Ward’s Criterion? *Journal of Classification*, *31*(3), 274–295. https://doi.org/10.1007/s00357-014-9161-z

Okazaki, Y., Kimoto, K., Asahi, H., Sato, M., Nakamura, Y., & Harada, N. (2014). Glacial to deglacial ventilation and productivity changes in the southern Okhotsk Sea. *Palaeogeography, Palaeoclimatology, Palaeoecology*, *395*, 53–66. https://doi.org/10.1016/j.palaeo.2013.12.013

Okumura, Y. M., Deser, C., Hu, A., Xie, S. P., & Timmermann, A. (2009). North Pacific climate response to freshwater forcing in the subarctic North Atlantic: Oceanic and atmospheric pathways. *Journal of Climate*, *22*(6), 1424–1445. https://doi.org/10.1175/2008JCLI2511.1

Oliva, F., Peros, M. C., Viau, A. E., Reinhardt, E. G., Nixon, F. C., & Morin, A. (2018). A multi-proxy reconstruction of tropical cyclone variability during the past 800 years from Robinson Lake, Nova Scotia, Canada. *Marine Geology*, *406*(April), 84–97. https://doi.org/10.1016/j.margeo.2018.09.012

Parnell, A. C., Haslett, J., Allen, J. R. M., Buck, C. E., & Huntley, B. (2008). A flexible approach to assessing synchroneity of past events using Bayesian reconstructions of sedimentation history. *Quaternary Science Reviews*, *27*(19–20), 1872–1885. https://doi.org/10.1016/j.quascirev.2008.07.009

Peltier, W. R., Argus, D. F., & Drummond, R. (2015). Space geodesy constrains ice age terminal deglaciation: The global ICE-6G_C (VM5a) model. *Journal of Geophysical Research: Solid Earth*, *120*(1), 450–487. https://doi.org/10.1002/2014JB011176

Penkrot, M. L., Jaeger, J. M., Cowan, E. A., St-Onge, G., & LeVay, L. (2018). Multivariate modeling of glacimarine lithostratigraphy combining scanning XRF, multisensory core properties, and CT imagery: IODP Site U1419. *Geosphere*, *14*(4), 1935–1960. https://doi.org/10.1130/GES01635.1

Penkrot, M., LeVay, L. J., & Jaeger, J. M. (2017). Data report: X-ray fluorescence scanning of sediment cores, Site U1419, Gulf of Alaska. *Proceedings of the Integrated Ocean Drilling Program*, *341*, 1–7. https://doi.org/10.2204/iodp.proc.341.203.2017

Piotrowski, A. M., Goldstein, S. L., Hemming, S. R., & Fairbanks, R. G. (2004). Intensification and variability of ocean thermohaline circulation through the last deglaciation. *Earth and Planetary Science Letters*, *225*(1–2), 205–220. https://doi.org/10.1016/j.epsl.2004.06.002

Plaza-Morlote, M., Rey, D., Santos, J. F., Ribeiro, S., Heslop, D., Bernabeu, A., Mohamed, K. J., Rubio, B., & Martíns, V. (2017). Southernmost evidence of large European Ice Sheet-derived freshwater discharges during the Heinrich Stadials of the Last Glacial Period (Galician Interior Basin, Northwest Iberian Continental Margin). *Earth and Planetary Science Letters*, *457*, 213–226. https://doi.org/10.1016/j.epsl.2016.10.020

Praetorius, S. K., Condron, A., Mix, A. C., Walczak, M. H., McKay, J. L., & Du, J. (2020). The role of Northeast Pacific meltwater events in deglacial climate change. *Science Advances*, *6*(9), 1–18. https://doi.org/10.1126/sciadv.aay2915

Praetorius, S. K., & Mix, A. C. (2014). Synchronization of North Pacific and Greenland climates preceded abrupt deglacial warming. *Science*, *345*(6195), 444–448. https://doi.org/10.1126/science.1252000

Praetorius, S. K., Mix, A. C., Walczak, M. H., Wolhowe, M. D., Addison, J. A., & Prahl, F. G. (2015). North Pacific deglacial hypoxic events linked to abrupt ocean warming. *Nature*, *527*(7578), 362–366. https://doi.org/10.1038/nature15753

Prahl, F. G., Muehlhausen, L. A., & Zahnle, D. L. (1988). Further evaluation of long-chain alkenones as indicators of paleoceanographic conditions. *Geochimica et Cosmochimica Acta*, *52*(9), 2303–2310. https://doi.org/10.1016/0016-7037(88)90132-9

Prahl, F. G., Popp, B. N., Karl, D. M., & Sparrow, M. A. (2005). Ecology and biogeochemistry of alkenone production at Station ALOHA. *Deep-Sea Research Part I: Oceanographic Research Papers*, *52*(5), 699–719. https://doi.org/10.1016/j.dsr.2004.12.001

Rasmussen, S. O., Andersen, K. K., Svensson, A. M., Steffensen, J. P., Vinther, B. M., Clausen, H. B., Siggaard-Andersen, M. L., Johnsen, S. J., Larsen, L. B., Dahl-Jensen, D., Bigler, M., Röthlisberger, R., Fischer, H., Goto-Azuma, K., Hansson, M. E., & Ruth, U. (2006). A new Greenland ice core chronology for the last glacial termination. *Journal of Geophysical Research: Atmospheres*, *111*(D6), 1–16. https://doi.org/10.1029/2005JD006079

Ravelo, A. C., & Hillaire-Marcel, C. (2007). The Use of Oxygen and Carbon Isotopes of Foraminifera in Paleoceanography. *Developments in Marine Geology*, *1*, 735–764. https://doi.org/10.1016/S1572-5480(07)01023-8

Reimer, P. J., Austin, W. E. N., Bard, E., Bayliss, A., Blackwell, P. G., Bronk Ramsey, C., Butzin, M., Cheng, H., Edwards, R. L., Friedrich, M., Grootes, P. M., Guilderson, T. P., Hajdas, I., Heaton, T. J., Hogg, A. G., Hughen, K. A., Kromer, B., Manning, S. W., Muscheler, R., … Talamo, S. (2020). The IntCal20 Northern Hemisphere Radiocarbon Age Calibration Curve (0-55 cal kBP). *Radiocarbon*, *62*(4), 725–757. https://doi.org/10.1017/RDC.2020.41

Reimer, P. J., Bard, E., Bayliss, A., Beck, J. W., Blackwell, P. G., Ramsey, C. B., Buck, C. E., Cheng, H., Edwards, R. L., Friedrich, M., Grootes, P. M., Guilderson, T. P., Haflidason, H., Hajdas, I., Hatté, C., Heaton, T. J., Hoffmann, D. L., Hogg, A. G., Hughen, K. A., … van der Plicht, J. (2013). Intcal13 and Marine13 Radiocarbon Age Calibration Curves 0–50,000 Years Cal Bp. *Radiocarbon*, *55*(4), 1869–1887. https://doi.org/10.2458/azu_js_rc.55.16947

Reynolds, L., & Thunell, R. C. (1985). Seasonal succession of planktonic foraminifera in the subpolar North Pacific. *Journal of Foraminiferal Research*, *15*(4), 282–301. https://doi.org/10.2113/gsjfr.15.4.282

Richter, T. O., van der Gaast, S., Koster, B., Vaars, A., Gieles, R., de Stigter, H. C., De Haas, H., & van Weering, T. C. E. (2006). The Avaatech XRF Core Scanner: Technical description and applications to NE Atlantic sediments. *Geological Society, London, Special Publication*, *267*, 39–50. https://doi.org/10.1144/GSL.SP.2006.267.01.03

Riethdorf, Jan-Rainer, Nürnberg, Dirk , Max, L., Tiedemann, R., Gorbarenko, S. A., Malakhov, M. I. (2013). Millennial-scale variability of marine productivity and terrigenous matter supply in the western Bering Sea over the past 180 kyr. *Climate of the Past*, *9*(3), 1345–1373. https://doi.org/10.5194/cp-9-1345-2013

Rinterknecht, V., Braucher, R., Böse, M., Bourlès, D., & Mercier, J. L. (2012). Late Quaternary ice sheet extents in northeastern Germany inferred from surface exposure dating. *Quaternary Science Reviews*, *44*, 89–95. https://doi.org/10.1016/j.quascirev.2010.07.026

Rodríguez-Germade, I., Rubio, B., Rey, D., Vilas, F., López-Rodríguez, C. F., Comas, M. C.,

& Martínez-Ruiz, F. (2015). Optimization of Itrax Core Scanner Measurement Conditions for Sediments from Submarine Mud Volcanoes. In I.W. Croudace & R. G. Rothwell (Eds.), *Micro-XRF Studies of Sediment Cores. Developments in Paleoenvironmental Research, vol 17* (pp. 103–126). Springer, Dordrecht. https://doi.org/10.1007/978-94-017-9849-5_3

Rosell-Melé, A. (1998). Interhemispheric appraisal of the value of alkenone indices as temperature and salinity proxies in high-latitude locations. *Paleoceanography*, *13*(6), 694–703. https://doi.org/10.1029/98PA02355

Rosell-Melé, A., Jansen, E., & Weinelt, M. (2002). Appraisal of a molecular approach to infer variations in surface ocean freshwater inputs into the North Atlantic during the last glacial. *Global and Planetary Change*, *34*(3–4), 143–152. https://doi.org/10.1016/S0921-8181(02)00111-X

Rothwell, R. G., & Croudace, I. W. (2015). *Twenty Years of XRF Core Scanning Marine Sediments: What Do Geochemical Proxies Tell Us? In: Croudace, I., Rothwell, R. (eds) Micro-XRF Studies of Sediment Cores. Developments in Paleoenvironmental Research, vol 17, Springer, Dordrecht*. https://doi.org/10.1007/978-94-017-9849-5_2

Rothwell, R. G., & Rack, F. R. (2006). New techniques in sediment core analysis: An introduction. *Geological Society Special Publication*, *267*, 1–29. https://doi.org/10.1144/GSL.SP.2006.267.01.01

Royer, T. C. (2005). Hydrographic responses at a coastal site in the northern Gulf of Alaska to seasonal and interannual forcing. *Deep-Sea Research Part II: Topical Studies in Oceanography*, *52*(1-2 SPEC. ISS.), 267–288. https://doi.org/10.1016/j.dsr2.2004.09.022

Royer, T. C., & Finney, B. (2020). AN OCEANOGRAPHIC PERSPECTIVE ON EARLY HUMAN MIGRATION TO THE AMERICAS. *Oceanography*, *33*(1), 32–41. https://doi.org/https://www.jstor.org/stable/26897833

Sachs, J. P., Pahnke, K., Smittenberg, R., & Zhang, Z. (2013). Paleoceanography, Biological Proxies │Biomarker Indicators of Past Climate. In *In: Elias, S. A. (ed.), The Encyclopedia of Quaternary Science (Second Edition), Elsevier, Amsterdam* (2nd ed.). Elsevier B.V. https://doi.org/10.1016/B978-0-444-53643-3.00280-6

Samson, S. D., Patchett, P. J., Gehrels, G. E., & Anderson, R. G. (1990). Nd and Sr Isotopic

Characterization of the Wrangellia Terrane and Implications for Crustal Growth of the Canadian Cordillera Published by : The University of Chicago Press Stable URL : http://www.jstor.org/stable/30068043 REFERENCES Linked references are. *Journal of Geology*, *98*(5), 749–762. https://doi.org/10.1086/629438

Sautter, L. R., & Thunell, R. C. (1989). Seasonal succession of planktonic foraminifera: results from a four-year time-series sediment trap experiment in the northeast Pacific. *Journal of Foraminiferal Research*, *19*(4), 253–267. https://doi.org/10.2113/gsjfr.19.4.253

Schiebel, R., Waniek, J., Bork, M., & Hemleben, C. (2001). Planktic foraminiferal production stimulated by chlorophyll redistribution and entrainment of nutrients. *Deep Sea Research Part I: Oceanographic Research Papers*, *48*(3), 721–740. https://doi.org/10.1016/S0967-0637(00)00065-0

Schroth, A. W., Crusius, J., Chever, F., Bostick, B. C., & Rouxel, O. J. (2011). Glacial influence on the geochemistry of riverine iron fluxes to the Gulf of Alaska and effects of deglaciation. *Geophysical Research Letters*, *38*(16), 1–6. https://doi.org/10.1029/2011GL048367

Schwestermann, T., Huang, J., Konzett, J., Kioka, A., Wefer, G., Ikehara, K., Moernaut, J., Eglinton, T. I., & Strasser, M. (2020). Multivariate Statistical and Multiproxy Constraints on Earthquake-Triggered Sediment Remobilization Processes in the Central Japan Trench. *Geochemistry, Geophysics, Geosystems*, *21*(6), 1–24. https://doi.org/10.1029/2019GC008861

Seguinot, J., Rogozhina, I., Stroeven, A. P., Margold, M., & Kleman, J. (2016). Numerical simulations of the Cordilleran ice sheet through the last glacial cycle. *The Cryosphere*, *10*(2), 639–664. https://doi.org/10.5194/tc-10-639-2016

Seki, A., Tada, R., Kurokawa, S., & Murayama, M. (2019). High-resolution Quaternary record of marine organic carbon content in the hemipelagic sediments of the Japan Sea from bromine counts measured by XRF core scanner. *Progress in Earth and Planetary Science*, *6*(1), 1–12. https://doi.org/10.1186/s40645-018-0244-z

Seki, O., Ikehara, M., Kawamura, K., Nakatsuka, T., Ohnishi, K., Wakatsuchi, M., Narita, H., & Sakamoto, T. (2004). Reconstruction of paleoproductivity in the Sea of Okhotsk over the last 30 kyr. *Paleoceanography*, *19*(1), 1–18. https://doi.org/10.1029/2002PA000808

Seki, O., Kawamura, K., Sakamoto, T., Ikehara, M., Nakatsuka, T., & Wakatsuchi, M. (2005). Decreased surface salinity in the Sea Okhotsk during the last glacial period estimated from alkenones. *Geophysical Research Letters*, *32*(8), 1–4. https://doi.org/10.1029/2004GL022177

Severmann, S., McManus, J., Berelson, W. M., & Hammond, D. E. (2010). The continental shelf benthic iron flux and its isotope composition. *Geochimica et Cosmochimica Acta, 74*(14), 3984–4004. https://doi.org/10.1016/j.gca.2010.04.022

Sholkovitz, E. R., Sedwick, P. N., & Church, T. M. (2009). Influence of anthropogenic combustion emissions on the deposition of soluble aerosol iron to the ocean: Empirical estimates for island sites in the North Atlantic. *Geochimica et Cosmochimica Acta*, *73*(14), 3981–4003. https://doi.org/10.1016/j.gca.2009.04.029

Sicre, M.-A., Bard, E., Ezat, U., & Rostek, F. (2002). Alkenone distributions in the North Atlantic and Nordic sea surface waters. *Geochemistry, Geophysics, Geosystems*, *3*(2), 1–13. https://doi.org/10.1029/2001gc000159

Sisson, V. B., Poole, A. R., Harris, N. R., Burner, H. C., Pavlis, T. L., Copeland, P., Donelick, R. A., & McLelland, W. C. (2003). Geochemical and geochronologic constraints for genesis of a tonalite-trondhjemite suite and associated mafic intrusive rocks in the eastern Chugach Mountains, Alaska: A record of ridge-transform subduction. *Geological Society of America Special Paper*, *371*, 293–326. https://doi.org/10.1130/0-8137-2371-X.293

Smith, N. T., Shreeve, J., & Kuras, O. (2020). Multi-sensor core logging (MSCL) and X-ray computed tomography imaging of borehole core to aid 3D geological modelling of poorly exposed unconsolidated superficial sediments underlying complex industrial sites: An example from Sellafield nuclear site, UK. *Journal of Applied Geophysics*, *178*, 104084. https://doi.org/10.1016/j.jappgeo.2020.104084

Snoeckx, H., Grousset, F., Revel, M., & Boelaert, A. (1999). European contribution of ice-rafted sand to Heinrich layers H3 and H4. *Marine Geology*, *158*(1–4), 197–208. https://doi.org/10.1016/S0025-3227(98)00168-6

Stabeno, P. J., Bell, S., Cheng, W., Danielson, S., Kachel, N. B., & Mordy, C. W. (2016). Long-term observations of Alaska Coastal Current in the northern Gulf of Alaska. *Deep-Sea Research Part II: Topical Studies in Oceanography*, *132*, 24–40.

https://doi.org/10.1016/j.dsr2.2015.12.016

Stabeno, P. J., Bond, N. A., Hermann, A. J., Kachel, N. B., Mordy, C. W., & Overland, J. E. (2004). Meteorology and oceanography of the Northern Gulf of Alaska. *Continental Shelf Research*, *24*(7–8), 859–897. https://doi.org/10.1016/j.csr.2004.02.007

Stroeven, A. P., Fabel, D., Codilean, A. T., Kleman, J., Clague, J. J., Miguens-Rodriguez, M., & Xu, S. (2010). Investigating the glacial history of the northern sector of the Cordilleran Ice Sheet with cosmogenic 10Be concentrations in quartz. *Quaternary Science Reviews*, *29*(25–26), 3630–3643. https://doi.org/10.1016/j.quascirev.2010.07.010

Stroeven, A. P., Fabel, D., Margold, M., Clague, J. J., & Xu, S. (2014). Investigating absolute chronologies of glacial advances in the NW sector of the Cordilleran Ice Sheet with terrestrial in situ cosmogenic nuclides. *Quaternary Science Reviews*, *92*, 429–443. https://doi.org/10.1016/j.quascirev.2013.09.026

Strom, S. L., Macri, E. L., & Fredrickson, K. A. (2010). Light limitation of summer primary production in the coastal Gulf of Alaska: Physiological and environmental causes. *Marine Ecology Progress Series*, *402*, 45–57. https://doi.org/10.3354/meps08456

Strom, S. L., Olson, M. B., Macri, E. L., & Mordy, C. W. (2006). Cross-shelf gradients in phytoplankton community structure, nutrient utilization, and growth rate in the coastal Gulf of Alaska. *Marine Ecology Progress Series*, *328*, 75–92. https://doi.org/10.3354/meps328075

Sun, Y., Xiao, W., Wang, R., Wu, L., & Wu, Y. (2021). Changes in sediment provenance and ocean circulation on the northern slope of the Bering Sea since the last deglaciation. *Marine Geology*, *436*(April). https://doi.org/10.1016/j.margeo.2021.106492

Takahashi, G. (2015). Sample preparation for X-ray fluorescence analysis III. Pressed and loose powder methods. *Rigaku Journal*, *31*(1), 25–30.

Tanaka, T., Togashi, S., Kamioka, H., Amakawa, H., Kagami, H., Hamamoto, T., Yuhara, M., Orihashi, Y., Yoneda, S., Shimizu, H., Kunimaru, T., Takahashi, K., Yanagi, T., Nakano, T., Fujimaki, H., Shinjo, R., Asahara, Y., Tanimizu, M., & Dragusanu, C. (2000). JNdi-1: A neodymium isotopic reference in consistency with LaJolla neodymium. *Chemical Geology*, *168*(3–4), 279–281. https://doi.org/10.1016/S0009-2541(00)00198-4

Tarasov, L., & Peltier, W. R. (2005). Arctic freshwater forcing of the Younger Dryas cold reversal. *Nature*, *435*(7042), 662–665. https://doi.org/10.1038/nature03617

Taylor, B. J., Rae, J. W. B., Gray, W. R., Darling, K. F., Burke, A., Gersonde, R., Abelmann, A., Maier, E., Esper, O., & Ziveri, P. (2018). Distribution and ecology of planktic foraminifera in the North Paci fi c : Implications for paleo-reconstructions. *Quaternary Science Reviews*, *191*, 256–274. https://doi.org/10.1016/j.quascirev.2018.05.006

Taylor, M. A., Hendy, I. L., & Pak, D. K. (2014). Deglacial ocean warming and marine margin retreat of the Cordilleran Ice Sheet in the North Pacific Ocean. *Earth and Planetary Science Letters*, *403,* 89–98. https://doi.org/10.1016/j.epsl.2014.06.026

Terashima, S., Imai, N., Itoh, S., Ando, A., & Mita, N. (1994). 1993 compilation of analytical data for major elements in seventeen GSJ geochemical reference samples, "Igneous rock series." *Bulletin of the Geological Society of Japan*, *45*(6), 305–381.

Terasmae, J. (1984). Radiocarbon dating: some problems and potential developments. In W. C. Mahaney (Ed.), *Developments in Palaeontology and Stratigraphy: Quaternary dating methods* (Vol. 7, pp. 1–15). Elsevier Science Publishers B.V., The Netherlands. https://doi.org/10.1016/S0920-5446(08)70060-8

Thomson, J., Croudace, I. W., & Rothwell, R. G. (2006). A geochemical application of the ITRAX scanner to a sediment core containing eastern Mediterranean sapropel units. *Geological Society, London, Special Publication*, *267*, 65–77. https://doi.org/10.1144/GSL.SP.2006.267.01.05

Tjallingii, R., Röhl, U., Kölling, M., & Bickert, T. (2007). Influence of the water content on X-ray fluorescence core scanning measurements in soft marine sediments. *Geochemistry, Geophysics, Geosystems*, *8*(2), 1–12. https://doi.org/10.1029/2006GC001393

Tomczak, M., & Godfrey, J. S. (1994). *Regional Oceanography: An Introduction*. Elsevier. Pergamon, Oxford, UK.

Tomokawa, A., Okazaki, Y., Onodera, J., & Horikawa, K. (2019). Silicoflagellate and Actiniscus response to meltwater during the last deglaciation in the Alaska margin. *Japan Geoscience Union Meeting, MAY 26-30, 2019*, MIS19-P21 2019.

Tütken, T., Eisenhauer, A., Wiegand, B., & Hansen, B. T. (2002). Glacial-interglacial cycles in Sr and Nd isotopic composition of Arctic marine sediments triggered by the Svalbard/Barents Sea ice sheet. *Marine Geology*, *182*(3–4), 351–372. https://doi.org/10.1016/S0025-3227(01)00248-1

Wackett, A. A. (2014). *Petrology and Geochemistry of the Crawfish Inlet and Krestof Island Plutons, Baranof Island, Alaska*.

Walczak, M. H., Mix, A. C., Cowan, E. A., Fallon, S., Keith Fifield, L., Alder, J. R., Du, J., Haley, B., Hobern, T., Padman, J., Praetorius, S. K., Schmittner, A., Stoner, J. S., & Zellers, S. D. (2020). Phasing of millennial-scale climate variability in the Pacific and Atlantic Oceans. *Science, 370*(6517), 716–720. https://doi.org/10.1126/science.aba7096

Walinsky, S. E., Prahl, F. G., Mix, A. C., Finney, B. P., Jaeger, J. M., & Rosen, G. P. (2009). Distribution and composition of organic matter in surface sediments of coastal Southeast Alaska. *Continental Shelf Research*, *29*(13), 1565–1579. https://doi.org/10.1016/j.csr.2009.04.006

Ward, J. H. (1963). Hierarchical Grouping to Optimize an Objective Function. *Journal of the American Statistical Association, 58*(301), 236–244. https://doi.org/10.1080/01621459.1963.10500845

Weaver, A. J., Saenko, O. A., Clark, P. U., & Mitrovica, J. X. (2003). Meltwater pulse 1A from Antarctica as a trigger of the Bølling-Allerød warm interval. *Science, 299*(5613), 1709–1713. https://doi.org/10.1126/science.1081002

Weingartner, T. J., Danielson, S. L., & Royer, T. C. (2005). Freshwater variability and predictability in the Alaska Coastal Current. *Deep-Sea Research Part II: Topical Studies in Oceanography, 52*, 169–191. https://doi.org/10.1016/j.dsr2.2004.09.030

Weltje, G. J., & Tjallingii, R. (2008). Calibration of XRF core scanners for quantitative geochemical logging of sediment cores: Theory and application. *Earth and Planetary Science Letters, 274*(3–4), 423–438. https://doi.org/10.1016/j.epsl.2008.07.054

Whitney, F. A., & Freeland, H. J. (1999). Variability in upper-ocean water properties in the NE Pacific Ocean. *Deep-Sea Research Part II: Topical Studies in Oceanography, 46*(11–12), 2351–2370. https://doi.org/10.1016/S0967-0645(99)00067-3

Woodward, C. A., & Gadd, P. S. (2019). The potential power and pitfalls of using the X-ray fluorescence molybdenum incoherent: Coherent scattering ratio as a proxy for sediment organic content. *Quaternary International*, *514*, 30–43. https://doi.org/10.1016/j.quaint.2018.11.031

Young, N. E., Briner, J. P., & Kaufman, D. S. (2009). Late Pleistocene and Holocene glaciation of the Fish Lake Valley, northeastern Alaska Range, Alaska. *Journal of Quaternary Science*, *24*(7), 677–689. https://doi.org/10.1002/jqs.1279

Ziegler, M., Jilbert, T., De Lange, G. J., Lourens, L. J., & Reichart, G. J. (2008). Bromine counts from XRF scanning as an estimate of the marine organic carbon content of sediment cores. *Geochemistry, Geophysics, Geosystems*, *9*(5), 1–6. https://doi.org/10.1029/2007GC001932

List of publication

In peer-reviewed journal (Impact Factor = 2.458)

Mondal, M. N., Horikawa, K., Seki, O., Nejigaki, K., Minami, H., Murayama, M., & Okazaki, Y. (2021). Investigation of Adequate Calibration Methods for X-Ray Fluorescence Core Scanning Element Count Data : A Case Study of a Marine Sediment Piston Core from the Gulf of Alaska. *Journal of Marine Science and Engineering*, *9*(5), 1–21. https://doi.org/10.3390/jmse9050540

Manuscript under preparation

Mondal, M.N.; Horikawa, K.; Seki, O.; Nejigaki, K.; Minami, H.; Murayama, M.; Okazaki, Y.; Masahiro, N.; Wakaki, S.; and Shin, K-C. Glacial meltwater injection into the northern Gulf of Alaska from the Cordilleran Ice Sheet is insights from alkenone (%$C_{37:4}$), ice-rafted debris, and isotope proxy records.

Mondal, M.N.; Horikawa, K.; Seki, O.; Nejigaki, K.; Minami, H.; Murayama, M.; Okazaki, Y. Multivariate and multiproxy analysis of high-resolution records revealing paleoproductivity and sedimentary changes in the northern Gulf of Alaska.

Conference publication

Md Nurunnabi Mondal, Keiji Horikawa, Katsuya Nejigaki, and Masafumi Murayama. High-resolution analyzed sedimentary records reveal the sedimentary changes in the continental slope of the Gulf of Alaska. *Abstract 4243, Goldschmidt® Virtual.2021 conference*, 4–9 July 2021.

Md Nurunnabi Mondal, Keiji Horikawa, Katsuya Nejigaki, Hideki Minami, Masafumi Murayama, Osamu Seki, and Yusuke Okazaki. Iron counts from XRF scanning positively correlated with the deglacial paleoproductivity in the Gulf of Alaska. *Abstract for Poster-Presentation, PP009-0014, American Geophysical Union (AGU) Fall Meeting* 1–17 December 2020.

Md Nurunnabi Mondal, Keiji Horikawa, Katsuya Nejigaki, Hideki Minami, Masafumi MURAYAMA, Osamu Seki, Yusuke Okazaki. Deglacial productivity changes reflect XRF Br fueled by Cordilleran Ice Sheet dynamics. *Abstract for Poster-Presentation, MIS08-18, Japan Geoscience Union-American Geophysical Union (JpGU-AGU) Joint Meeting*, 12–16 July 2020.

Keiji Horikawa, **Nurunnabi MD Mondal,** Masafumi MURAYAMA, Katsuya Nejigaki, Osamu Seki, Yusuke Okazaki. The advantages and limits of ITRAX core scanner: Learning by comparison with destructive element and isotope data from the Gulf of Alaska sediment core. *Abstract for Poster-Presentation, MIS12-02, Japan Geoscience Union-American Geophysical Union (JpGU-AGU) Joint Meeting*, 12–16 July 2020.

Award and honor

2018 – 2021: Scholarship for Doctoral Program awarded by the Government of Japan (MEXT)

2019 Travel grant for sightseeing by the University of Toyama